Czech Technical University in Prague
Faculty of Electrical Engineering

Doctoral Thesis

Prague, Feruary 2022

Ing. Ondrej Tereň

Czech Technical University in Prague

Faculty of Electrical Engineering
Department of Measurement

Dielectric Spectroscopy in High Voltage Machines Diagnostics

Doctoral Thesis

Ing. Ondrej Tereň

Prague, Feruary 2022

Supervisor:	**doc. Ing. Josef Vedral, CSc.**
Supervisor-specialist:	**Ing. Radek Sedlacek, PhD.**
Ph.D. programme:	Electrical Engineering and Information Technology (P2612)
Branch of study:	Measurement and Instrumentation (2601V006)

Acknowledgement

I would like to thank my advisors Doc. Ing. josef Vedral, CSc. and Ing. Radek Sedláček, PhD. for a great opportunity to study doctoral studies at the Department of Measurement at Faculty of Electrical Engineering of Czech Technical University in Prague.

Declaration

I declare that I worked out the presented thesis independently and I quoted all used sources of information in accord with Methodical instructions about ethical principles for writing academic thesis.

Abstract

Táto práca zaoberá problematikou nedeštruktívnej diagnostiky vysoko napäťových strojov v odbore výroby elektrickej energie. Hlavný dôraz je kladený na meracie metódy slúžiace na posúdenie stavu izolácie týchto strojov. Tieto nedeštruktívne metódy slúžia na snahu predikovať nadchádzajúcu poruchu stroja. Táto práca vznikla ako čiastkový cieľ väčšieho vedeckého projektu. Cieľom projektu bolo venovať sa nedeštruktívnej diagnostike strojom v širšom ohľade. Okrem dielektrickej spektroskopie (DSP) bola študovaná aj metóda frekvenčnej odozvy (FRA). Aj preto je hlavným cieľom tejto práce navrhnúť hardvérovú platformu vhodnú pre obidve spomenuté metódy. Platforma by mala vykazovať lepšie parametre ako prístroje dostupné na trhu.

Spomenuté sú základné definície a fyzikálne princípy ako polarizácia, dielektrická relaxácia a absorpcia. Ďalej sú spomenuté najpoužívanejšie metódy nedeštruktívnej diagnostiky v oblasti vysoko napäťových strojov. Zvláštny záujem je venovaný metóde DSP. Opísané sú dva rôzne prístupy k tejto metóde: spektroskopia v časovej oblasti (TDS) a spektroskopia vo frekvenčnej oblasti (FDS). Ďalej je zhrnutý zoznam na trhu dostupných meracích prístrojov, spolu s ich najdôležitejšími parametrami.

Práca ďalej pokračuje popisom návrhu hardvérovej platformy. Táto práca popisuje návrh analógovej dosky, ktorá je časťou celého navrhovaného meracieho systému. Úlohou analógovej dosky je zabezpečiť všetky potrebné konverzie analógových signálov na digitálne a späť. Ďalšia kapitola popisuje softvérové vybavenie meracej platformy. Hlavnou úlohou aplikácie je implementovať potrebné výpočty pre obidve metódy. Ďalšou úlohou je zobrazovať namerané dáta a zabezpečiť rýchlu a spoľahlivú komunikáciu s hardvérovou platformou.

V neposlednom rade posledné kapitoly dokumentujú testovanie a overovanie navrhnuté meracieho systému. Testovanie bolo rozdelené do dvoch fáz. V prvej fáze sa jednalo o testovanie v laboratórnych podmienkach. Tieto testy potvrdili základnú funkcionalitu systému ako sú vektorový voltmeter a generátor s nastaviteľnou frekvenciou. Druhá fáza testovania znamenala testovanie v prevádzkových podmienkach na reálnych testovaných objektoch. Vedecký tím navštívil spoločnosť zaoberajúcu sa opravami vysokonapäťových transformátorov, ktorá poskytla dva transformátory ako testovacie vzorky. Behom týchto testov bolo potvrdené že navrhnutý systém je funkčný aj v podmienkach reálnej prevádzy. V závere kapitoly sú zmienené dve možnosti metód pre vyhodnotenie nameraných údajov. Prvá metóda využíva porovnávanie nameraných výsledkov pomocou vyhodnotenia plochy pod nameranou krivkou. Druhá metóda využíva porovnávanie výsledkom vyhodnotením korelačného keoficientu.

Kľúčové slová

elektrická impedancia; elektrická kapacita; dielektrická spektroskopia; spektroskopia v časovej oblasti; spektroskopia vo frekvenčnej oblasti; lock-in zosilňovač; diagnostika VN strojov; izolácia; dielektrikum

Abstract

The thesis discuss the problems of the non-invasive diagnostic of high-voltage machines used in the field of electricity production systems. Much emphasis is given to methods intended for machine insulation state assessment. These are non-invasive diagnostics methods and their role is to try to predict an upcoming machine failure. This thesis arose from a larger scientific team form. The teamwork was intended for non-invasive diagnostic of high voltage machines in general. Besides dielectric spectroscopy (DSP), frequency response analysis (FRA) was studied. Therefore, the main goal of the thesis is to design a hardware platform suitable for both DSP and FRA methods. The platform should have better parameters than market available instrumentations.

The most frequently used methods and principles of the non-invasive diagnostic in the field of high voltage machines are described in the thesis. Special interest is devoted to mainly dielectric spectroscopy. Two different approaches are described time-domain spectroscopy (TDS) and frequency domain spectroscopy (FDS). The common market available measuring instruments are further discussed. Especially, parameters such as measurement precision are mentioned.

The work continues with a description of the design of the hardware platform. This thesis describes the design of a daughterboard, which is a part of the whole measuring instrument platform. The role of the daughterboard is to provide necessary analog-to-digital conversions and vice versa. The next chapter deals with the design of software equipment for the designed instrumentation. A PC control application has been developed for the designed platform. The role of the application is not only to control the platform itself but to provide necessary computation for both DPS and FRA methods.

Last but not least chapters discuss achieved results. The testing itself is divided into two stages. The first stage is intended to test in laboratory conditions. These tests confirmed the basic functionality of the proposed instrumentation platform such as vector voltmeter and frequency sweep generator. The second stage of the testing was intended to perform a test with real tested objects. The research team visited a company dealing with high voltage transformer repair. They provided two samples to be tested. During these tests, the instrumentation platform has been confirmed to be able to use to perform the measurement in the real environment as well. Also, two methods of dataset evaluation have been outlined. One method utilized comparison of areas underneath measured curves and the second one is based on correlation coefficient evaluation.

Key words

electrical impedance; electrical capacitance; dielectric spectroscopy; time domain spectroscopy; frequency domain spectroscopy; lock-in amplifier; HV machines diagnostic; insulation; dielectric;

Contents

Abbreviations

AC	alternating current
AD	analog to digital
ADC	analog to digital converter
DC	direct current
DSP	digital signal processing
DUT	device under test
ENOB	effective number of bits
FDS	frequency domain spectroscopy
FPGA	field programmable array
FRA	frequency response analysis
FSG	frequency sweep generator
GUI	graphic user interface
HSMC	high speed mezzanine connector
HV	high voltage
LIA	lock-in amplifier
PCB	printed circuit board
PSU	power supply unit
PDC	polarization and depolarization current
RMS	root mean square
TDS	time domain spectroscopy

Symbols

C	Electric capacitance.
$\mathbf{D}$	Electric displacement field.
$\mathbf{E}$	Electric field.
$\mathbf{P}$	Electric polarization.
R	Electric resistance.
$\mathbf{Z}$	Electric impedance.
ϵ_0	Vacuum permittivity.
χ	Electric susceptibility.
σ	Electric conductivity.

1. Introduction

In the field of energetics, there is an amount of high-voltage (HV) machines that lifetime is expected of the order of tens of years. As an example may be mentioned the power transformers and generators directly used in the production and the transmission of electricity. To achieve the expected lifetime it is necessary to plan regular diagnostic examinations of these machines, thus the machine operator avoids an unexpected shut down of the machine or the entire system [1].

The HV machines windings and insulations are constantly exposed to a combination of heat, electric, and mechanical stresses [2], [3]. All of these factors influence the state of the machine winding insulation. The state of the winding insulation is one of the studied parameters that can detect an upcoming failure. There is a few measurements methods used to winding insulation state assessment as electric resistance measurement using DC current [4], partial discharge measurement [5], [6], dielectric response measurement [7], capacitance and dissipation factor measurement and dielectric spectroscopy [8].

The main goal of this work is to try to develop a hardware platform suitable for dielectric spectroscopy assessment of the insulation of the HV rotary and non-rotary machines. The platform should improve the parameters of the market available instruments. The dielectric spectroscopy is a general method used in the field of materials engineering [9]. Modified methods are used in the field of energetics and the insulation testing of the HV machines. The literature introduces the methods as a time (TDS) and a frequency domain spectroscopy (FDS).

In this work, the topic of dielectric is discussed. The basic definitions and principles such as polarization, dielectric relaxation, and absorption are stated. The next chapter deals with measurement methods used for the insulation state assessment in general. Then, close attention is paid to the description of the dielectric spectroscopy measurement. Two different approaches TDS and FDS are described. A principle of the methods is described and the market available measuring instruments is discussed.

Hence, this work is a result of teamwork of a larger research group, a description of a workload division is stated in the Chapter 3. The chapter describes what are the goals of this thesis and was planned to do by the author of the thesis. In the next sections, a design of the hardware platform is described. The platform is mainly intended for the TDS and FDS methods as well. Expecting these two methods, the proposed platform can find an application in frequency response analysis (FRA) diagnostics. Special emphasis is given to the author's contribution to teamwork. Other researchers' results are briefly outlined only to provide necessary information to the reader. The platform description is divided into two chapters. The first describes hardware design and the second software equipment. Measurement uncertainties are discussed then. A detailed uncertainties analysis is described concerning the developed computation algorithms.

The last chapters deal with the verification of the proposed instrumentation platform. The main emphasis is given to prove the improvement of the market available instrumentation parameters. The laboratory test and field test are performed as well. The test results and the thesis goals evaluations are stated in the conclusions.

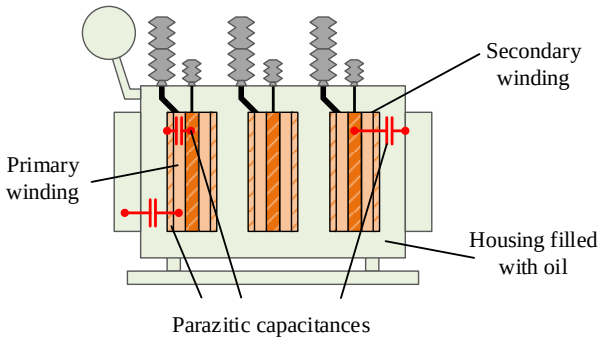

Figure 1. Parasitic capacitances in high voltage transformer. Simplified diagram.

1.1. Theory of Dielectric

The electrical machines consist of parts made of different types of material. Generally, the basic parts of the machines are windings, insulation, and housing encapsulating the machine in one entity. These parts form a serial reliability chain, which means a failure of one of these parts causes a failure of the whole system. The most vulnerable part to failures is insulation [10]. Therefore, it is necessary to pay attention to the machine insulation system during its lifetime.

The main goal of the insulation system is to provide an electric separation between parts with different electric potentials (primary and secondary winding) and cooling of the winding system. From the electric point of view, the winding and the insulation system form a parasitic capacitor between themselves (see Fig. 1). Since the electric capacitance is a relatively easily measurable physical quantity, it is a good way how to describe the current state of the insulation system of the particular machines. The well-known relation says

$$C = \frac{\varepsilon_r \cdot \varepsilon_0 \cdot A}{d}, \tag{1}$$

where C is the electric capacitance, ε_r is a relative permittivity of the insulation material (dielectric material parameter), ε_0 is a vacuum permittivity, A is an area of the overlapping electrodes and d is a distance between the electrodes. It is obvious, the capacitance changes its value with the relative permittivity, the electrode distance, and the overlapping area. The last two components may refer to a mechanical failure of the machine (winding displacement, corrosion). Since this work is intended for dielectric spectroscopy, therefore studying the insulation material, further attention will be paid to the relative permittivity.

This section tries to briefly explain phenomena taking place in the dielectric material and its relation to external stresses of the dielectric material. The relative permittivity is studied as a macroscopic quantity describing the material. The effect of the dielectric polarization is described and related to a microscopic quantity. Basic principles utilized in technical diagnostic are stated.

1.1.1. Dielectric Definition

A dielectric material is any material that can produce an inner electric field after placing in an external electric field **E**. The electric charges do not flow through the material, they only change their positions around their equilibrium point depending on the outer electric field direction. Hence, it is a material able to polarize.

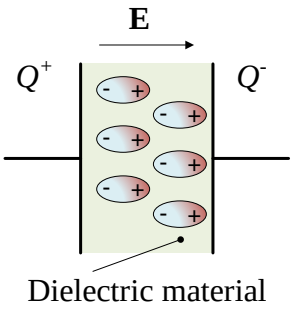

Figure 2. Dielectric material inside the electric field.

On the other hand, an insulator is a material able to prevent a current flow through the material between locations with different potentials. Therefore, the dielectric is a more general term than the insulator is. It is true, that each insulator is a dielectric material, not vice-versa.

The measure of how easily the material can be polarized in response to the electric field is defined as an electric susceptibility χ_e. It is defined as a constant of proportionality to the external electric field and then a polarization density vector $\mathbf{P}$ can be defined as

$$\mathbf{P} = \chi_e \epsilon_0 \mathbf{E}, \tag{2}$$

where $\epsilon_0 = 8.854 \cdot 10^{-12}\ F \cdot m^{-1}$ is an electric permittivity of free space. The electric displacement $\mathbf{D}$ is then related by

$$\mathbf{D} = \epsilon_0 \mathbf{E} + \mathbf{P} = \epsilon \mathbf{E}, \tag{3}$$

where $\epsilon = \epsilon_0 \cdot \epsilon_r$ is permittivity and ϵ_r is a relative permittivity. Substituting with the equation (2) leads to

$$\mathbf{D} = \epsilon_0 \mathbf{E} + \chi_e \epsilon_0 \mathbf{E} = \epsilon_0 \cdot \epsilon_r \mathbf{E}. \tag{4}$$

Dividing the equation (4) by expression $\epsilon_0 \mathbf{E}$ leads to

$$1 + \chi_e = \epsilon_r. \tag{5}$$

1.1.2. Polarization

Every kind of dielectric material consists, at an atomic level, of negative and positive charges. The charges are balancing each other and on the macroscopic level, they produce a neutral charge. Applying an external electrical field $\mathbf{E}$ the charges become oriented thus formate electric dipoles. The positive charges are attracted to the negative pole and vice versa, see Fig. 2. This phenomenon is called polarization.

Two electric charges of opposite magnitudes separated by distance d form an electric dipole. The quantity representing properties of the electric dipole is called electric dipole moment $\mathbf{p}$ (Fig. 3) and it is defined as

$$\mathbf{p} = q\mathbf{d}, \tag{6}$$

where $\mathbf{d}$ is a displacement vector pointing from negative to positive charge. The previous equations describe only one dipole from a microscopic point of view. In practice, there

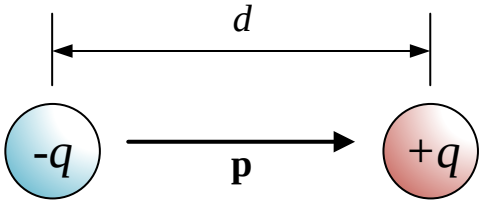

Figure 3. Electric dipole moment schematic.

is often a need to study the material from a macroscopic point of view. Thus, the materials contain a lot of electric dipoles. Then the overall dipole moment can be expressed as a sum of particular dipole moments

$$\mathbf{p} = \sum_{i=1}^{N} q_i \mathbf{d}_i = \sum_{i=1}^{N} \mathbf{p}_i, \tag{7}$$

or presuming a continuous charge distribution in a material of volume V

$$\mathbf{p}\left(\mathbf{r}\right) = \iiint\limits_{V} \rho\left(\mathbf{r}_0\right)\left(\mathbf{r}_0 - \mathbf{r}\right) d^3\mathbf{r}_0, \tag{8}$$

where $\mathbf{r}_0$ is the reference position vector, $\rho\left(\mathbf{r}_0\right)$ is the charge density and $d^3\mathbf{r}_0$ is the elementary volume of V.

The degree of the polarization of the dielectric material due to the external electrical field is given by the physical quantity called a polarization density $\mathbf{P}$, firstly mentioned in equation (2). The polarization density of the material of the volume V can be also defined by the electric dipole moment as

$$\mathbf{P} = \lim_{\Delta V \to 0} \frac{\Delta \mathbf{p}}{\Delta V}. \tag{9}$$

The quantity characterizing the polarization from the microscopic point of view is called polarizability α. The unit of the polarizability is $F \cdot m^2$. Polarizability indicates the measure of the dielectric system change due to an external electric field. Then the induced dipole moment of the particle can be expressed as

$$\mathbf{p} = \alpha \cdot \mathbf{E}_L, \tag{10}$$

where $\mathbf{E}_L$ is intensity of the local electrical field at the place of the studied particle respecting the interactions of the other particles. The polarization vector density then can be expressed the polarizability as

$$\mathbf{P} = n \cdot \mathbf{p} = n \cdot \alpha \cdot \mathbf{E}_L, \tag{11}$$

where n is an induced dipoles concentration of only one type of particles. Comparing with equation (2) leads to

$$n \cdot \alpha \cdot \mathbf{E}_L = \chi \cdot \varepsilon_0 \cdot \mathbf{E}, \tag{12}$$

using the identity (78) it leads to

$$n \cdot \alpha \cdot \mathbf{E}_L = (\varepsilon_r - 1) \cdot \varepsilon_0 \cdot \mathbf{E}, \tag{13}$$

$$\varepsilon_r = 1 + \frac{n \cdot \alpha \cdot \mathbf{E}_L}{\varepsilon_0 \cdot \mathbf{E}}. \tag{14}$$

This equation expresses the relation between microscopic and macroscopic quantities describing the dielectric materials. It also tells that it is necessary to deal with the intensity of the local electric field $\mathbf{E}_L$. The local electric field is composed of two components, the mean macroscopic external electric field (given by external voltage applied to the material and electrodes geometry) and the component given by a vector sum of the electric field of all of the particles surrounding the studied particle. It could be derived [10], that for isotropic dielectric material the local electric field is equal to

$$\mathbf{E}_L = \frac{\varepsilon_r + 2}{3} \cdot \mathbf{E}. \tag{15}$$

The total polarization of the material can be caused by the external electric field applied to the dielectric material. There are also different mechanisms allowing the material to be polarized even without the activity of the external electric field. It is, for example, piezoelectric polarization, caused by mechanical stress of the dielectric material. However, this work will further deal only with polarization mechanisms dependent on the external electric field.

Types of polarization induced by the external electric field can be divided by charge carrier type. In general, the whole polarization density contribution can be expressed as [11]

$$\mathbf{P}_{total} = \mathbf{P}_e + \mathbf{P}_i + \mathbf{P}_o + \mathbf{P}_d + \mathbf{P}_s + \mathbf{P}_{others}, \tag{16}$$

where $\mathbf{P}_e$ is an electronic polarization, $\mathbf{P}_i$ is an ionic polarization, $\mathbf{P}_o$ is an orientational polarization, $\mathbf{P}_d$ is a space charge polarization, $\mathbf{P}_s$ is a spontaneous polarization and $\mathbf{P}_{others}$ covers other types of polarizations which are out of this thesis scope.

Electronic Polarization

If an atom is not affected by the external electric field the center of the electron shell and atomic nuclei are at the same point. Thus, the atom is not polarized and it does not have an electric dipole moment. When the atom is affected by the external electric field, the track of the electrons stretches along the direction of the electric field. This causes the atom to obtain the dipole moment of the magnitude dependent on the electric field magnitude and the ability of the material to get polarized (electric polarizability). Fig. 8 shows the electronic polarization phenomenon on a hydrogen atom.

Because the electronic polarization mechanism takes place inside the atom, the mechanism is not affected by the heat movement of the atoms. The settle time may vary between $10^{-16} - 10^{-13}\,s$. Therefore the electronic polarization is not dependent on the temperature and it does not cause energy loss. The electronic polarization takes place at each substance and state of matter [10].

Ionic Polarization

Applying the external field to a material built up with positive and negative ions held together by ionic bonds, the distance changes between the particulars ions. The mechanism is described in the Fig. 5 using the sodium chloride ion.

The settle time varies between $10^{-13} - 10^{-12}\,s$ [10]. That means the ionic polarization is frequency independent. The ionic bond is strong enough to the ionic polarization be considered as temperature-independent too and therefore lossless.

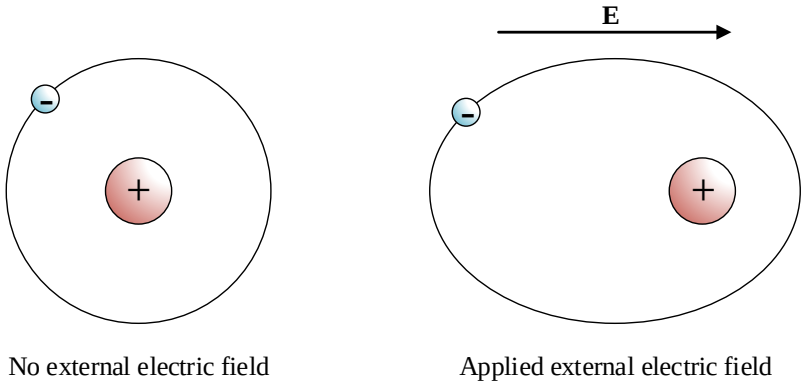

Figure 4. Electronic polarization mechanism described on the hydrogen atom.

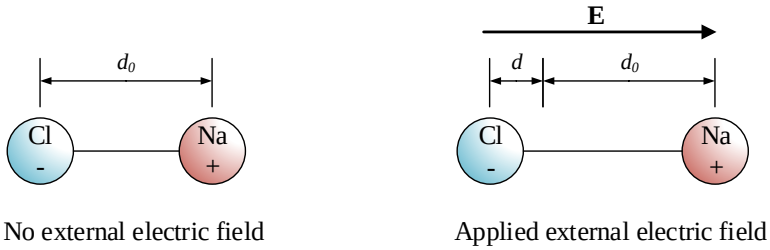

Figure 5. Ionic polarization mechanism described on the sodium chloride ion.

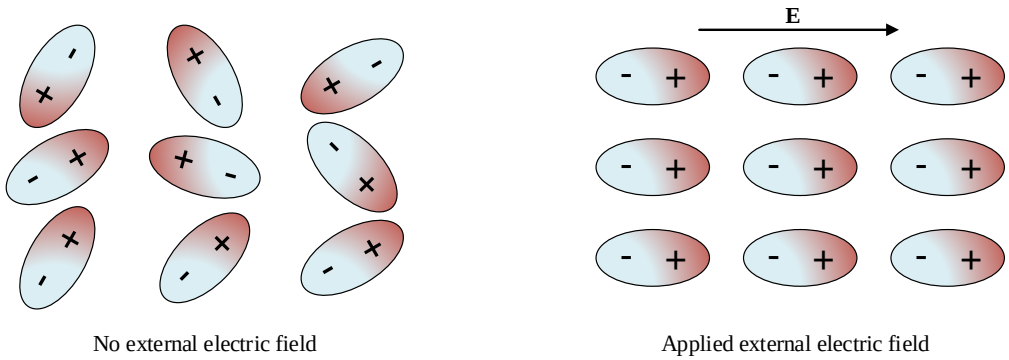

Figure 6. Orientational polarization mechanism.

Orientational Polarization

Applying the external electric field to polar molecules, the randomly oriented dipoles round along the electric field intensity vector. This mechanism is called orientational polarization. The scheme of the mechanism is shown in Fig. 6. The orientational polarization is temperature and frequency dependant. It is not even an "instant" process. It takes some time while the dipole turns around along the electric field direction. The phenomenons related to the noninstant dielectric response to the external electric field are further discussed in chapter 1.1.4.

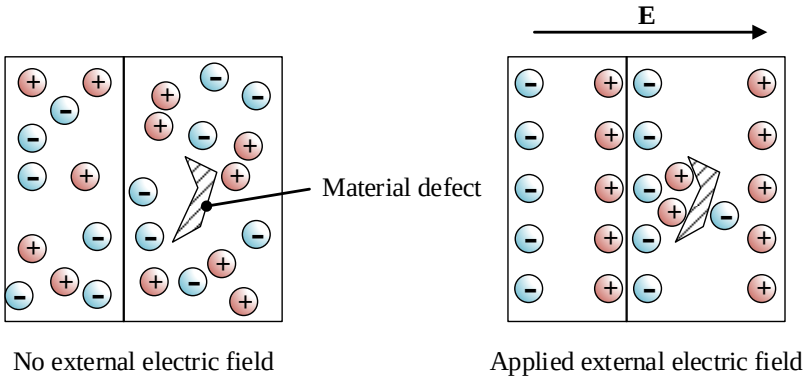

Figure 7. Space charge polarization mechanism.

1.1.3. Space Charge Polarization

Besides the bound charges, the free charges can participate in the polarization mechanism too. Two conditions have to be fulfilled to be the material able of space charge polarized. First, there should be free charges present in the material. Second, the material should contain some nonhomogeneity. For example voids, bubbles, cracks, or other defects. The free charges start to migrate over the material due to excitation by the external electric field. The migrating free charges are caught on the inhomogeneities and thus act like a polarized volume of the dielectric material from a macroscopic point of view. The process is schematically drawn on the Fig. 7. This polarization mechanism is the slowest one among all discussed mechanisms and causes signification losses [10].

1.1.4. Dielectric Relaxation

Until this point, the previous text presumed that the dielectric material can react instantly to changing external electric field. In the real world, this is not possible and it takes some time while the material particles take place along the exciting electric field. Due to this reason, it is necessary to slightly improve the previous quantities definitions. Let's assume time variable intensity of electric field and time-variable electric displacement field

$$\mathbf{E}(t) = E \cdot e^{j\omega t}, \tag{17}$$

$$\mathbf{D}(t) = D \cdot e^{j(\omega t - \delta)}, \tag{18}$$

where bold symbols indicates a vector quantity and regular symbol their magnitudes. The phase angle δ represents the lag of the non instant dielectric response. Therefore, the equation (4) can be rewritten to the form

$$\mathbf{D}(t) = \varepsilon_0 \hat{\varepsilon}(j\omega)\, \mathbf{E}(t), \tag{19}$$

where $\hat{\varepsilon}(j\omega)$ is a frequency dependant complex relative permittivity. According to it is a complex number, it can be written

$$\hat{\varepsilon}(j\omega) = \varepsilon'(\omega) - j \cdot \varepsilon''(\omega), \tag{20}$$

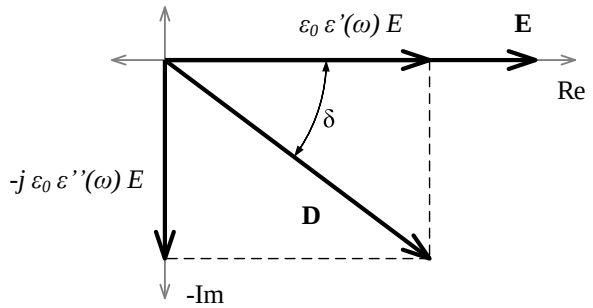

Figure 8. Complex relative permittivity interpretation. Similar picture at [10]

where $\varepsilon'(\omega)$ is a real and $\varepsilon''(\omega)$ is an imaginary part of $\hat{\varepsilon}(j\omega)$. The real part expresses a capacitance character of the dielectric, whereas the imaginary part is a measure of the losses in the dielectric material stressed by the alternating external electric field. A graphical representation of the vectors is shown on Fig. 8.

Neglecting the dc conductivity it can be defined

$$\begin{aligned} &\varepsilon'(\omega \to 0) = \varepsilon_s, \\ &\varepsilon'(\omega \to \infty) = \varepsilon_\infty, \\ &\varepsilon''(\omega \to 0) = 0, \\ &\varepsilon''(\omega \to \infty) = 0, \end{aligned} \tag{21}$$

where ε_s is a static relative permittivity and ε_∞ is a theoretical value of relative permittivity belonging to an infinity frequency.

When the polarization processes are not able to instantly follow the external electric field, but they are characterized by a certain finite time response, this phenomenon is called **dielectric relaxation**. A Dutch-American physicist Peter Debye derived the equation for weak polar liquid dielectrics

$$\hat{\varepsilon}(j\omega) = \varepsilon_\infty + \frac{\varepsilon_s - \varepsilon_\infty}{1 + j\omega\tau}, \tag{22}$$

where τ is a temperature dependent and time independent characteristic time of relaxation. The equation respects only one particular time of relaxation related to the on of the polarization mechanism. Diving the equation to the real and the imaginary part leads to

$$\hat{\varepsilon}(j\omega) = \varepsilon_\infty + \frac{\varepsilon_s - \varepsilon_\infty}{1 + j\omega^2\tau^2} - j\frac{(\varepsilon_s - \varepsilon_\infty)\,\omega\tau}{1 + \omega^2\tau^2}, \tag{23}$$

comparing with the equation (20) leads to decomposing into real and imaginary parts

$$\varepsilon'(\omega) = \varepsilon_\infty + \frac{\varepsilon_s - \varepsilon_\infty}{1 + j\omega^2\tau^2}, \tag{24}$$

$$\varepsilon''(\omega) = \frac{(\varepsilon_s - \varepsilon_\infty)\,\omega\tau}{1 + \omega^2\tau^2}. \tag{25}$$

Fig. 8 provides an imagination how to express the phase delay δ. Using the goniometric functions it can be written

$$\tan\delta = \frac{\varepsilon_0 \cdot \varepsilon''(\omega) \cdot E}{\varepsilon_0 \cdot \varepsilon'(\omega) \cdot E} = \frac{\varepsilon''(\omega)}{\varepsilon'(\omega)}. \tag{26}$$

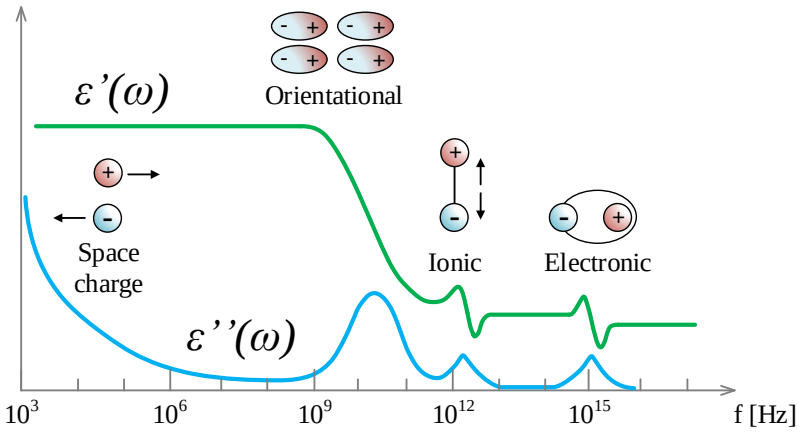

Figure 9. Frequency response of dielectric mechanisms. Reproduced picture from [12]

.

As it was stated above, the imaginary part of the complex relative permittivity represents the losses in the dielectric material excited by the alternating electric field. Therefore, the ratio of the imaginary and the real part is considered as a measure of the dielectric losses. In other words, it is called a **dissipation factor**. Combining the equations (24), (25) and (26) lead to

$$\tan\delta = \frac{\varepsilon''(\omega)}{\varepsilon'(\omega)} = \frac{(\varepsilon_s - \varepsilon_\infty)\cdot\omega\cdot\tau}{\varepsilon_s + \varepsilon_\infty\omega^2\tau^2}. \tag{27}$$

Fig 9. displays a frequency dependence of the relative permittivity of a model dielectric material. The different types of polarization mentioned in Chapter 1.1.2 produce a permittivity contribution in a different characteristic section. For example, the orientational polarization is strongly presented at microwave frequencies (around the units of GHz). This effect is widely used in microwave ovens. Because the water molecules are permanent dipoles, orientational polarization takes place. Even the imaginary part of the relative permittivity forms a peak around these frequencies and the dissipation factor rises. The process is then very lossy and that is why the food inside the oven gets hot.

It should be mentioned that each type of polarization has its cut-off frequency. As the frequency is rising the slower polarization mechanism fades and the permittivity contribution of the faster mechanisms takes place. There are also peaks of the imaginary part of the relative permittivity formed at the areas near these cut-off frequencies. In the other words, the different types of polarization have a different contributions to the entire relative permittivity dependence both frequency and the magnitude value.

Except for the frequency dependence, there is also a temperature dependence of the relative permittivity. The molecules in the material are still randomly moving around its equilibrium positions. This movement is caused by thermal motion. The higher temperature the greater influence of the thermal motion, hence the molecules are moving faster. Applying the external electric field the molecules are still under influence of the thermal motion, but their equilibrium position aligns with the field. The equilibrium can be understood as an average orientation of the studied molecule over a long period. As the amplitude of the thermal motion rises with the temperature, the molecules move so significantly, that they cease to be perfectly aligned with the external electric field,

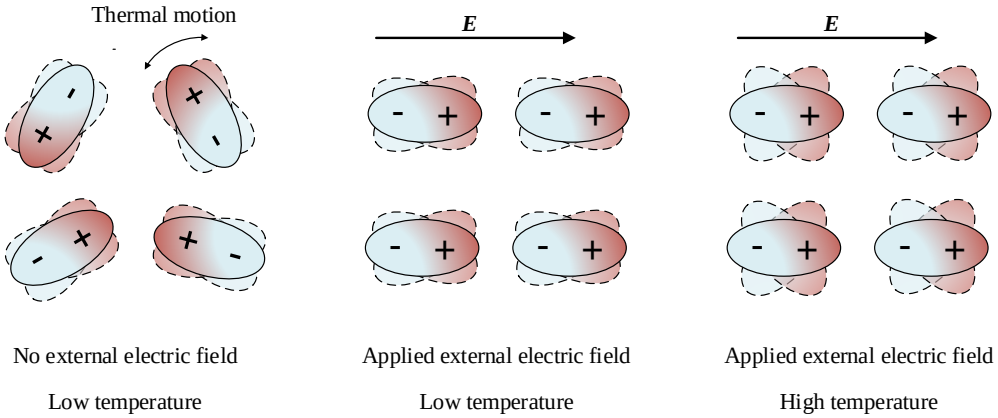

Figure 10. Thermal motion of the molecules affected by the external electric field.

see Fig. 10. It causes a degradation of the polarization effect, therefore the dielectric constant (real part of the complex relative permittivity) decreases. This is a reason that it has to be respected the temperature has a significant effect on the dielectric constant.

1.1.5. Dielectric Absorption

Dielectric absorption is a common name for non-stationary processes that are taking place in the dielectric material inserted between two electrodes of the capacitor and excited by the direct voltage [10]. As it was stated in previous chapters, the real dielectric material is not able to follow the external stimuli instantly, and therefore it is not able to react to a step function of the exciting voltage.

Fig. 11 shows an approximation of the electric charge (blue line) and electric current (red line) time course flowing through the capacitor formed by the studied dielectric material. A step of the direct voltage is present from time $t = 0$ until the time t_v. Hence, the diagram could be divided in two separated periods. A charging section occupies the time interval $t = 0...t_v$ and a discharging section occupies the time interval $t = t_v...\infty$.

The charging period is characterized by four stages.

- An initial charge increase Q_0 - charging of a geometric capacitance of the capacitor. The charge corresponds to a capacitor of the same dimensions but with vacuum instead of the studied dielectric material.
- The following charge increase Q_d - this charge increase is caused by the very fast electronic (Chapter 1.1.2) and ionic (Chapter 1.1.2) polarization types with the settle time between $10^{-16} - 10^{-12}\ s$.
- A relaxation charge increase Q_r - this charge increase is caused by the slower polarization mechanisms such as orientational (Chapter 1.1.2) and space charge polarization (Chapter 1.1.3). Due to the slower response of these polarization types, the time course of the increasing charge has to be considered. Hence, it can be written

$$Q_r\left(t\right) = Q_s \cdot \left(1 - e^{-\frac{1}{\tau}}\right), \tag{28}$$

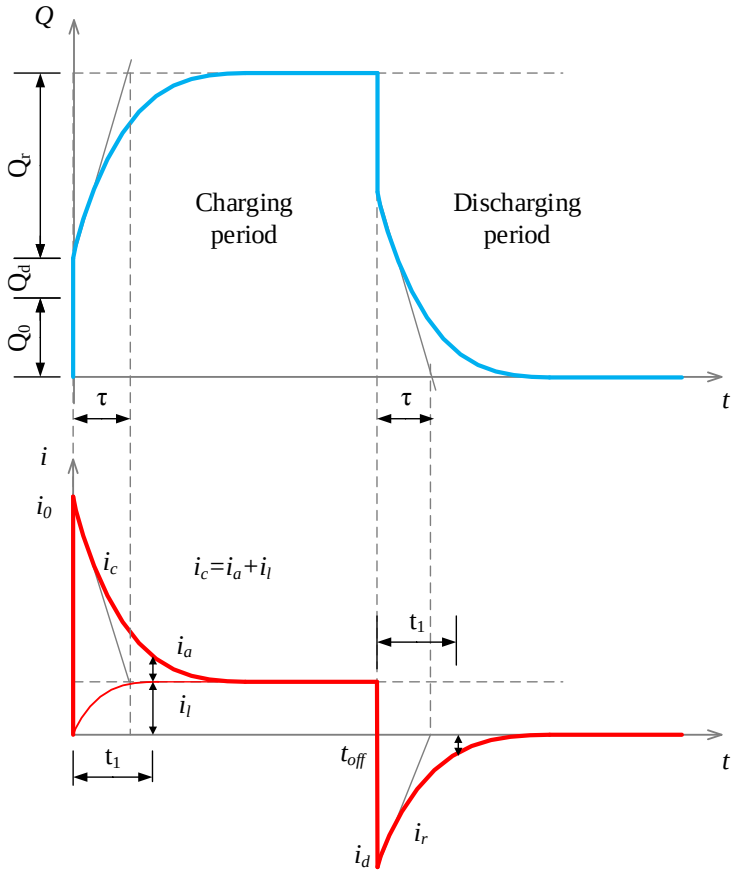

Figure 11. Time course of electric charge and current during charging and discharging a capacitor. Reproduced picture from [10]

.

where Q_s is a magnitude of the settled charge $Q_r(t)$ and τ is a time constant also known as a **relaxation time**.

- Once the polarization processes are settled a conductive current (caused by a DC conductivity of the material) is only flowing through the dielectric.

During the discharge period, the external voltage source is disconnected and capacitor terminals are shorted. This period is in contrast with the charging period characterized by the reverse order of the mentioned stages. The charge magnitude is asymptotically approaching zero over time.

Fig. 11 shows that the electric current is composed of a several components.

- An initial current i_0 - corresponds to the charging of the geometric capacitance and fast polarization mechanisms (electronic and ionic). Its magnitude is given by an internal resistance and voltage magnitude of the power supply and the DC conductivity of input wires and terminals.
- A charging current i_c - corresponds to the charging of the slower polarization mechanism. Once the initial current subsides, the current flowing through the dielectric rapidly decreases with the time constant $\tau = R_0 \cdot C$, where R_0 is an electrical resistance of the wires and input terminals plus internal resistance of the power supply and C is the electric capacitance of the capacitor forms by the

studied dielectric material.

The charging current is composed of two components

$$i_c(t) = i_a(t) + i_l(t), \tag{29}$$

where $i_a(t)$ is an absorption current and $i_l(t)$ is a leakage current. The absorption current is composed of the sum of the polarization currents corresponding to the slower polarization mechanisms (orientational and space charge). The absorption current is time variable and its decrease rate is dependent on the structure and state of the dielectric material. It can be written

$$Q_r(t) = \int_0^t i_a \mathrm{d}t = Q_s\left(1 - e^{-\frac{t}{\tau}}\right). \tag{30}$$

The leakage current is caused by the DC conductivity of the dielectric material. The magnitude of the absorption current is asymptotically approaching the leakage current value over time. The value of the leakage current is usually very low assuming the dry inviolate insulation.

After the time t_{off} the excitation voltage is disconnected and the capacitor terminals are shorted. This causes a discharging current i_d starts to flow through the capacitor. The discharge current subsides very quickly. Then a resorption current i_r takes place. It is a time variable and it is asymptotically approaching zero. It should be mentioned that

$$i_a(t_1) \neq -i_r(t_{off} + t_1), \tag{31}$$

because a part of the charge discharged thorough the leakage inside the material.

At the base of the equation (30), the absorption current time course should have an exponential shape. It could be true only if the current was formed by only one time the polarization mechanism. As it was stated above, in the real world there are several types the polarization and therefore the absorption current decreases slower and does not fit the perfect exponential curve.

The decreased rate of the charging current is an important parameter in the technical diagnostic. It can help to assess the current state of the dielectric system. The diagnostic methods utilize direct sampling and integrating the time course of the charging current or they define different types of indexes. Commonly used term is a **dielectric absorption ratio** (DAR).

There are two types of frequently used indexes. Both of them are characterized as a ratio of two readings of the charging current at a different time from the time of connection to the external voltage source. The literature [13] defines 60/30-Second Ratio as

$$r_{60/30} = \frac{i_c(30)}{i_c(60)} = \frac{R_i(60)}{R_i(30)}, \tag{32}$$

where $i_c(30)$ and $i_c(60)$ are charging current readings at the time 30 seconds and 60 seconds after the excitation voltage has been connected, $R_i(30)$ and $R_i(60)$ are isolation resistance readings at the time 30 seconds and 60 seconds after the measurement start.

The second very frequently used index is a polarization index. The polarization index p_i is defined as a ratio of the charging current reading at 10 minutes and 1 minute after

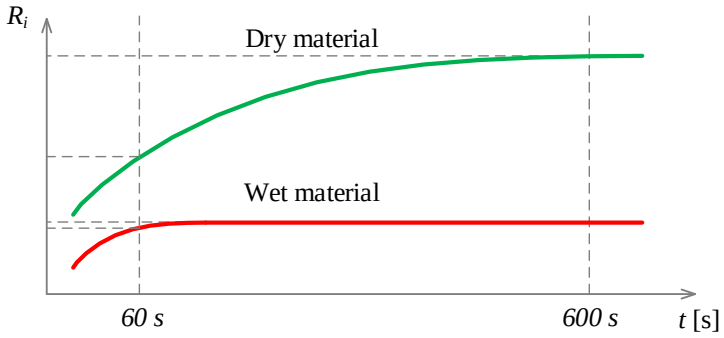

Figure 12. Time course of isolation resistance of dry and wet dielectric material. Similar pictures in [10] and [13]

.

Table 1. Condition of insulation indicated by the dielectric absorption ratio [13].

Insulation Condition	$r_{60/30}$	p_i
Dangerous	-	Less than 1
Questionable	1.0 to 1.25	1.0 to 2.0
Good	1.4 to 1.6	2.0 to 4.0
Excellent	Above 1.6	Above 4.0

external voltage connection [13]

$$p_i = \frac{i_c\,(600)}{i_c\,(60)} = \frac{R_i\,(60)}{R_i\,(600)}, \tag{33}$$

where the meaning of the quantities used is similar to the equation above. It is interesting, the literature [10] defines the polarization index using the times 60 and 15 seconds as well. Fig. 12 shows an example of the isolation resistance time course of a dry and a wet dielectric material. It is possible to see the difference between resistance reading at 60 s and 600 s. Therefore the polarization index will differ. The higher polarization index, the more dry is the material. Table 1 shows a simple guidelines how to interpret the dielectric absorption ratios.

1.1.6. Dielectric Conductivity

The main role of the dielectric material is to provide reliable insulation between places with different electric potentials. Nevertheless, there is not a perfect dielectric material that is able of absolute isolation. Due to different additions and impurities, there is the leakage current and therefore the isolation conductivity is non-zero.

A practical reasons led to a definition of an electric resistance and an electric conductance. The mutual relation between these quantities can be expressed as

$$\sigma = \frac{1}{\rho}, \tag{34}$$

where σ is the conductance of the dielectric material and ρ is the resistance of the

material. The resistance can be further expressed

$$\rho = R_i \cdot \frac{S}{h}, \tag{35}$$

where R_i is the measured isolation resistance, S is area of the electrodes and h is thickness of the material sample.

1.1.7. Dielectric Loss

In Chapter 1.1.4, there was outlined that the imaginary part of the complex relative permittivity is a measure of a dielectric loss. The dielectric loss could be understood as an amount of energy that is transformed in the exciting dielectric material into another undesirable type of energy. Mostly it is heated. The dielectric loss could be caused by a lot of factors. For example, it is a type of dielectric material, structure, properties, purity of the material. A major cause can be the temperature of the material and the slower types of polarization mechanisms such as orientational and space charges. The last but not least loss contribution is the leakage current. It is proportional to the isolation conductivity of the material. It can be written that the frequency dependant conductivity is equal

$$\sigma(\omega) = \omega \cdot \varepsilon_0 \cdot \varepsilon''(\omega), \tag{36}$$

where $\sigma(\omega)$ is the frequency dependent conductivity, ω is the angular velocity, ε_0 is the vacuum permittivity and $\varepsilon''(\omega)$ is the imaginary part of the complex relative permittivity (see Chapter 1.1.4).

In the case of DC electric field, the dielectric loss is only formed by the isolation conductivity. Then it can be expressed

$$P_{W_{DC}} = R_i \cdot I^2 = \frac{U^2}{R_i}, \tag{37}$$

where $P_{W_{DC}}$ is a dissipation power due to DC electrical field, R_i is the isolation resistance of the material, U is an excitation voltage and I is a steady electric current flowing through the studied material.

A more complex situation occurs when the dielectric is stressed by an AC electric field. The dissipation caused by slower polarization mechanisms takes place and it is also necessary to consider the noninstant reaction of the dielectric material. A phasor diagram of the voltage and current related to a capacitor formed by the studied dielectric material is shown in Fig. 13. If the dielectric material was lossless, the angle between voltage phasor u and the current phasor i would be precisely 90 degrees. Hence, there is a dissipation, the current phasor is rotated by a dissipation angle δ in the direction of the voltage phasor.

The current phasor can be decomposed to a vector sum of the initial current i_0, the absorption current i_a, and the leakage current i_l. These quantities were further discussed in Chapter 1.1.5. The absorption current can be further decomposed to the real i'_a and imaginary i''_a part. Then a dissipation current component is a vector sum of the real part of the absorption current i'_a and the leakage current i_l. Then the dissipation power due to an AC electric field can be expressed

$$P_{W_{AC}} = U \cdot (i'_a + i_l) = U \cdot I \cdot \sin\delta. \tag{38}$$

Let's assume a linear process inside the dielectric material. Then, the dielectric dissipation can be studied using equivalent serial or parallel circuits. In the other

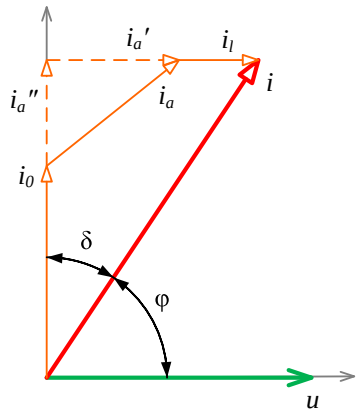

Figure 13. The phasor diagram of a real dielectric. Reproduced pictures from [10]

.

words, the dielectric can be understood as an electric circuit formed by a resistor and a capacitor. This circuit simulates the vector parameters of the current and the voltage of the dielectric. Nevertheless, they do not explain the physical meaning of the dielectric phenomena.

Serial Equivalent Circuit

Fig. 14 shows a serial equivalent circuit of the dielectric material with a corresponding phasor diagram. The circuit is formed by a serial combination of a resistor R_s and a capacitor C_s. Based on the phasor diagram, it can be expressed

$$\tan\delta = \frac{U_R}{U_C}, \tag{39}$$

where $\tan\delta$ is the dissipation factor, firstly mentioned in equation (26), U_R is voltage on the resistor U_C is voltage on the capacitor. These voltages can be further expressed using the Ohm‘s law as

$$U_R = R_s \cdot I, \tag{40}$$

$$U_C = \frac{I}{\omega \cdot C_s}, \tag{41}$$

where I is a current flowing through the circuit, R_s is a resistance of the serial equivalent circuit and C_s is a capacitance of the serial equivalent circuit. Combining these expressions with the equation (39) the dissipation factor can be expressed as

$$\tan\delta = \omega \cdot R_s \cdot C_s. \tag{42}$$

The total complex electric impedance of the serial equivalent circuit can be expressed as a serial combination of the resistance R_s and an impedance of the capacitor C_s

$$\mathbf{Z} = R_s + \frac{1}{j \cdot \omega \cdot C_s}, \tag{43}$$

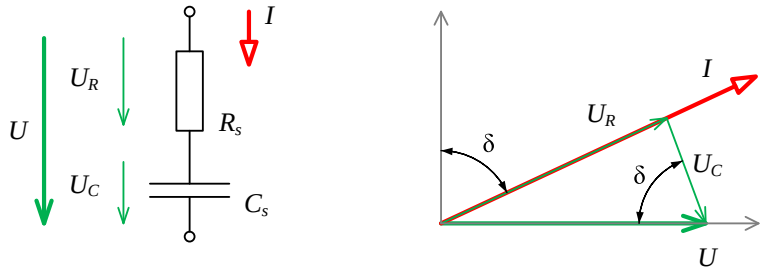

Figure 14. Serial equivalent circuit with corresponding phasor diagram

.

then the magnitude of the impedance

$$Z = |\mathbf{Z}| = \sqrt{R_s^2 + \frac{1}{\omega^2 \cdot C_s^2}}. \tag{44}$$

Using the Ohm's law again, the current can be expressed as

$$I = \frac{U}{Z}. \tag{45}$$

Parallel Equivalent Circuit

Fig. 15 shows a parallel equivalent circuit of the dielectric material with a corresponding phasor diagram. The circuit is formed by a parallel combination of a resistor R_p and a capacitor C_p. Based on the phasor diagram, it can be expressed

$$\tan\delta = \frac{I_R}{I_C}, \tag{46}$$

where $\tan\delta$ is the dissipation factor, I_R is a current flowing through the resistor and I_C is a current flowing through the capacitor. These currents can be further expressed using the Ohm's law as

$$I_R = \frac{U}{R_P}, \tag{47}$$

$$I_C = \omega \cdot C_p \cdot U, \tag{48}$$

where U is a voltage on the parallel combination, R_p is a resistance of the parallel equivalent circuit and C_p is a capacitance of the parallel equivalent circuit. Combining these expressions with the equation (46) the dissipation factor can be expressed as

$$\tan\delta = \frac{1}{\omega \cdot R_p \cdot C_p}. \tag{49}$$

The total complex electric impedance of the serial equivalent circuit can be expressed as a parallel combination of the resistance R_p and an impedance of the capacitor C_p

$$\mathbf{Z} = \frac{1}{\frac{1}{R_p} + j \cdot \omega \cdot C_p}, \tag{50}$$

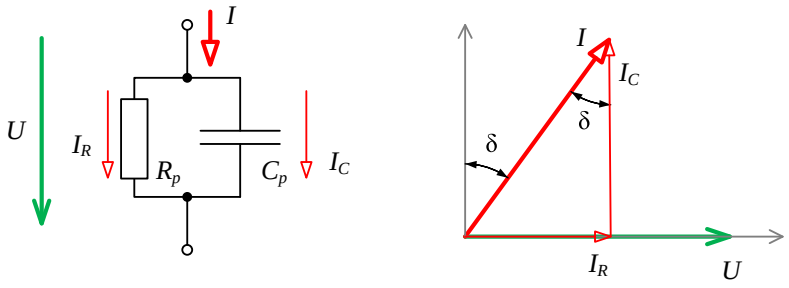

Figure 15. Parallel equivalent circuit with corresponding phasor diagram

.

then the magnitude of the impedance

$$Z = |\mathbf{Z}| = \frac{1}{\sqrt{\frac{1}{R_p^2} + \omega^2 \cdot C_p^2}}. \tag{51}$$

Using the Ohm's law again, the current can be expressed as

$$U = I \cdot Z. \tag{52}$$

Circuit Transition Identities

It is useful to know some identities that help to transform one type (serial or parallel) equivalent circuit into another. Comparing the equations (42) and (49) it gives the following transition identities

$$R_p = \frac{1 + \tan^2 \delta}{\tan^2 \delta} \cdot R_s, \tag{53}$$

$$C_p = \frac{C_s}{1 + \tan^2 \delta}. \tag{54}$$

1.1.8. Dielectric Strength

The dielectric materials are mostly used to electrically isolate two parts of the electric machine with different electric potentials. In the other words, the insulator has to be able to prevent flowing the electric current between these parts. It may seem a lot of materials can fulfill this requirement. But, it has to be considered a lot of ambient conditions such as temperature, moisture, and last but not least the magnitude of the acting electric field. If the magnitude of the electric field exceeds a certain limit it causes a rapid increase of the free charge carriers' amount and their movability. Hence, a rapid decrease of the isolation resistance and uncontrollable increase of the dielectric conductivity occurs. The process ends with a breakdown when the exposed places are connected by a conductive path with very low resistance.

A quantity representing the maximum limit the dielectric can withstand is called dielectric strength. It can be expressed as

$$E_S = \frac{U_{\max}}{d} \left[V \cdot m^{-1}\right], \tag{55}$$

where $U_{\max}$ is a breakdown voltage and d is a thickness of the material.

2. State of the Art

This chapter describes the current development state of the dielectric spectroscopy method. A brief description of the dielectric materials theory is mentioned. Basic terminology and principles are stated. Then an overview of the dielectric spectroscopy method is stated. Two approaches frequency domain and time-domain spectroscopy are mentioned. A comparison of market available instruments implementing the dielectric spectroscopy is stated. Other widely used measurement methods in the field of HV machines are described at the end of the chapter.

2.1. Dielectric spectroscopy

Dielectric spectroscopy methods are based on studying the changes of dielectric properties of the insulation materials. The dielectric properties are dependent on many factors, e.g. on the frequency or the time, on the temperature and chemical composition of an individual dielectric, or on the structure of an insulation system composed of different dielectrics [14]. In power electrical engineering most of the diagnostic methods utilize the measurement of a dielectric dissipation factor. The used frequency of voltage source is equal to the power frequency i.e. the frequency the device is designed for. However, the analysis at a single frequency may not detect even a strong change in the dielectric properties. Therefore, a method that utilized a measurement in a wider frequency range was developed.

2.1.1. Dielectric response

Chapter 1.1 describes phenomena taking place at dielectric material stressed by the external electric field. It was mentioned, any real dielectric material can react to these stimuli instantly. The relation between electric displacement, external electric field, and

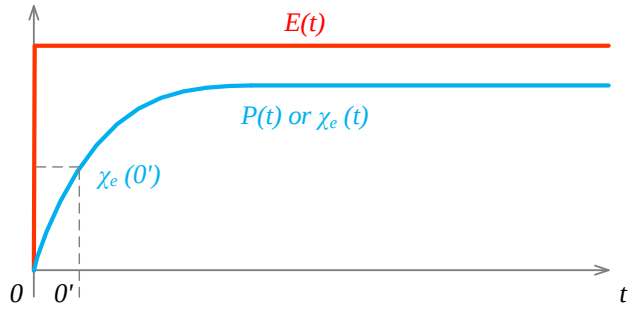

Figure 16. Dielectric polarization time course in dielectric material exposed by external electric field.

dielectric polarization was expressed as

$$\mathbf{D}(t) = \varepsilon_0 \cdot \mathbf{E}(t) + \mathbf{P}(t) = \varepsilon_0 \cdot \mathbf{E}(t) + \chi_e(t) \cdot \varepsilon_0 \cdot \mathbf{E}(t). \tag{56}$$

The time delay between external electric field $\mathbf{E}(t)$ and dielectric polarization $\mathbf{P}(t)$ is then characterized by the electric susceptibility $\chi_e(t)$. The time variant susceptibility then covers the polarization processes from the fast electronic and ionic polarization to the slowest orientational and space charge polarization. Lets assume an ideal step function of the external excitation electric field, see Fig. 16. Then the dielectric polarization may be expressed as

$$\mathbf{P}_1(t) = \chi_e(t) \cdot \varepsilon_0 \cdot \mathbf{E}(t) \cdot 1(t), \tag{57}$$

where $1(t)$ is a step function and $\mathbf{P}_1(t)$ is a dielectric polarization step response function. Assuming a liner and isotropic dielectric material we can calculate the time dependent electric polarization $\mathbf{P}(t)$ using the liner system theory for any other time dependent electric field $\mathbf{E}(t)$. Knowing the step response from equation (57) the resulting polarization can be computed by the time domain convolution or Duhamel's integral [15]. The Duhamel's integral can be defined as

$$b(t) = \frac{d}{dt} = \int_0^t a(z)\, b_1(t-z)\, dz = b_1(0)\, a(t) + \int_0^t a(z)\, \frac{db_1(t-z)}{dt} dz, \tag{58}$$

where $a(t)$ is a general force acting on a system fulfilling the condition $a(t) = 0$ for $t < 0$, $b(t)$ is an effect to the system at any place of the system and $b_1(t)$ is the known effect to the system exciting by step function (step response). Assuming the liner and isotropic dielectric material the equation can be simplified using a non-vector quantities. Recognizing the identities

$$a(t) \Leftrightarrow E(t), \tag{59a}$$
$$b(t) \Leftrightarrow P(t), \tag{59b}$$
$$b_0(t) \Leftrightarrow P_1(t), \tag{59c}$$

and combining with equation (56) the dielectric polarization response to an arbitrary external electric field $\mathbf{E}(t)$ can be expressed as

$$P(t) = \varepsilon_0 \cdot \chi_e(0) \cdot E(t) + \varepsilon_0 \int_0^t E(\tau)\, \frac{d\chi_e(t-\tau)}{dt} d\tau. \tag{60}$$

The derivative of the electric susceptibility can be declared as

$$f(t) = \frac{d\chi_e(t)}{dt}, \tag{61}$$

where $f(t)$ is a dielectric response function. Thus, the equation (60) can be rewritten as

$$P(t) = \varepsilon_0 \cdot \chi_e(0) \cdot E(t) + \varepsilon_0 \int_0^t E(\tau)\, f(t-\tau)\, d\tau. \tag{62}$$

The dielectric polarization is not a directly measurable quantity. However, according to James Clark Maxwell, the external electric field applied to the dielectric material generates a current density $j\,(t)$, which can be expressed

$$j\,(t) = j_c\,(t) + j_d\,(d) = \sigma \cdot E\,(t) + \frac{dD\,(t)}{dt}, \tag{63}$$

where $j\,(t)$ is a total current density flowing through the material sample, $j_c\,(t)$ is a conduction current caused by the dielectric conductivity (see Chapter 1.1.6), $j_d\,(d)$ is a displacement current and σ is the conductivity of the dielectric material. Using the equations (56), (62) and (63), the total current density can be expressed as

$$\begin{aligned} j\,(t) &= \sigma_0 \cdot E\,(t) + \varepsilon_0\,(1 + \chi_e\,(0'))\,\frac{dE\,(t)}{dt} + \varepsilon_0 \frac{d}{dt}\int_{0'}^{t} f\,(t-\tau)\,E\,(\tau)\,d\tau \\ &= \sigma_0 \cdot E\,(t) + \varepsilon_0\,(1 + \chi_e\,(0'))\,\frac{dE\,(t)}{dt} + \varepsilon_0 \cdot f\,(0')\,E\,(t) + \varepsilon_0 \int_{0'}^{t} \frac{d\,f\,(t-\tau)}{dt} E\,(\tau)\,d\tau, \end{aligned} \tag{64}$$

where $0'$ is a time instant shortly after the time zero, see Fig. 16 and term $(1 + \chi_e\,(0'))$ is the real part of the complex permittivity. This equation represents a basis of the dielectric response function experimental determination. There are two approaches how to measure, first time domain method and the second frequency domain method. They will be briefly discussed in the next chapters.

2.1.2. Time domain spectroscopy

The time-domain spectroscopy is based on the measurement of charging and resorption currents, see Chapter 1.1.5. Some literature denotes these quantities as polarization and depolarization currents, see Fig. 17. Other literature and instruments operational manuals indicate this method as PDC measurement [14]. There is shown a principle of the PDC measurement in Fig. 17 and a base schematic of a measurement circuit in Fig. 18.

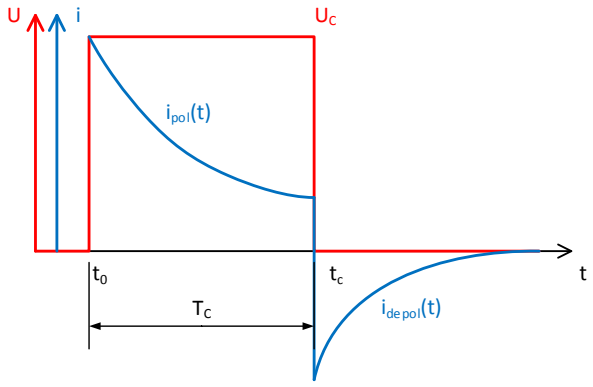

Figure 17. The principle of the time domain spectroscopy measurement [14]

In practice, a direct measurement of electric current density is not being used. Instead, it is used to measure the electric current amplitude. Since the equation (64)

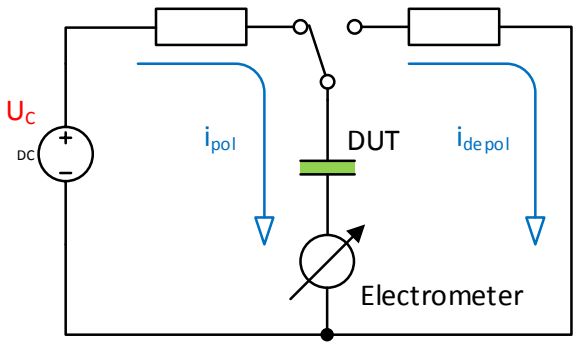

Figure 18. The base schematic of the time domain spectroscopy measurement [14]

is expressing the relation of the current density, it is necessary to define a relation between the electric current (as a measurable quantity) too. One of the most known expression is

$$i\left(t\right) = \oint_{S} j\left(t\right) dS, \tag{65}$$

where S is the area of the integration. It could be presume, the dimensions of the tested material sample are known and constant. Therefore, the area of the integration is constant and known, then the described theory can be expressed using the current density.

Let's assume the dielectric material of the device under test (DUT) or its insulation is completely discharged at the beginning of the measurement ($t < t_0$). At the time of t_0 a step function of the electrical field is applied to the DUT using a low ripple DC power supply source U_C. The power supply causes an i_{pol} current is flowing through the DUT and an electrometer records the current time course. The polarization current can be expressed as [16]:

$$i_{pol}\left(t\right) = C_0 U_C \left[\frac{\sigma_0}{\varepsilon_0} + f\left(t\right)\right], \tag{66}$$

where C_0 is a geometric capacitance of the DUT, U_C is the step DC charging voltage applied to the DUT, σ_0 is a DC conductivity of the DUT.

In next step a switch is put into the opposite position at the time of t_C. The charge stored in the DUT is now discharged through the electrometer that is also sampling the i_{depol} current. The depolarization current can be expressed as [16]:

$$i_{depol}\left(t\right) = -C_0 U_C \left[f\left(t\right) - f\left(t + T_C\right)\right]. \tag{67}$$

There are also stated two resistors with a small resistance in the schematic. Their role is only to limit flowing currents and they have no significant effect on the measured quantities. The measured currents values vary in the range of approximately 1 pA to 10 nA. The time duration of the measurement is usually up to three hours [17]. A typical result of the PDC measurement is shown in Fig 19.

2.1.3. Frequency domain spectroscopy

The frequency-domain spectroscopy (FDS) is one of the methods suitable for studying the polarization phenomena. Every kind of insulation material consists, at an atomic

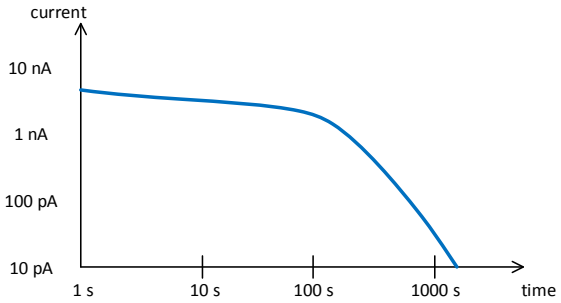

Figure 19. The typical result of the PDC measurement [17]

level, of negative and positive charges. The charges are balancing each other and on the macroscopic level, they produce a neutral charge. Applying an external electrical field E the charges become oriented thus formate dipoles. The positive charges are attracted to the negative pole and vice versa. This phenomenon is called polarization.

The FDS is a method that utilized an AC current excitation of studied material (transformer insulation). The capacitance and the dissipation factor are measured as a function of frequency of the excitation signal [18], that can be expressed using an equation

$$\mathbf{I}(\omega) = j\omega C(\omega)\,\mathbf{U}(\omega) \tag{68}$$

where $\mathbf{I}(\omega)$ is the measuring current, $C(\omega)$ is the capacitance of the measured material sample $\mathbf{U}(\omega)$ is the excitation voltage. The frequency range is usually between 1 mHz and 1 kHz and the voltage level of hundreds of volts is needed [19].

A base block diagram of an FDS analyzer with a typical connection to a device under test (DUT) is shown in Fig. 20. The DUT is represented by a transformer with a primary winding H and two secondary windings A and B. There are also shown parasitic capacitances C_{HA}, C_{HB}, and C_{HG} that can be measured using the FDS analyzer. The FDS analyzer consists of a frequency sweep generator (FSG), a high-voltage amplifier, and two ammeters. The FSG generates a sinus waveform with an adjustable frequency. This signal is amplified using the high-voltage amplifier to an amplitude of hundreds of volts. A studied parasitic capacitance of the DUT is excited by the amplified signal. A current flowing through the studied capacitance and a normal capacitor is measured by the ammeters. To computation of capacitance and dissipation factor, it is necessary to measure both the current amplitude and the current phase concerning the generating signal. The measured parameters are calculated using the following equation.

$$\mathbf{Z_X} = \frac{\mathbf{I_N}}{\mathbf{I_X}}\mathbf{Z_N}, \tag{69}$$

where $\mathbf{Z_X}$ is the measured electrical impedance, which can be decomposed to electrical capacitance and the dissipation factor, $\mathbf{Z_N}$ is a normal capacitance, $\mathbf{I_X}$ is electric current flowing through the DUT and $\mathbf{I_N}$ is current flowing through the normal capacitor. A typical dissipation factor course measured using the FDS method is shown in Fig. 21.

The dielectric properties in the frequency domain can be described using the Laplace or Fourier transformation [15]. Let‘s still assume an ideal electric field or excitation voltage step function starting at time $t = 0$. Let’s further assume the following identities

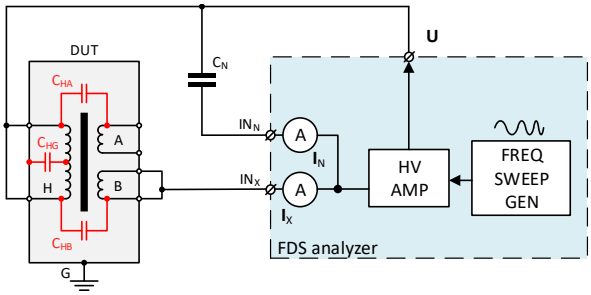

Figure 20. The block diagram of the dual channel FDS analyzer

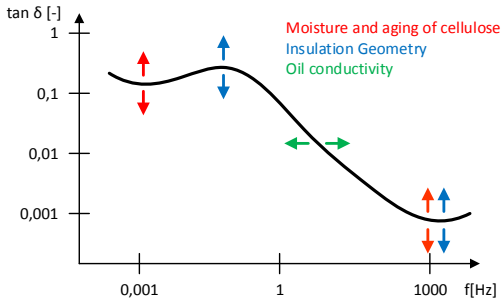

Figure 21. The typical FDS measurement result and factors affecting the dissipation factor, similar picture in [19]

$$\begin{aligned} j(t) &\Rightarrow j(p), \\ E(t) &\Rightarrow E(p), \\ \frac{dE(t)}{dt} &\Rightarrow pE(p), \\ f(t) &\Rightarrow F(p), \end{aligned} \tag{70}$$

then the equation (64) can be transform into the following form

$$j(p) = \sigma_0 E(p) + \varepsilon_0 p E(p) + \varepsilon_0 p F(p) E(p), \tag{71}$$

where the last term of the sum forms a convolution of $F(p)$ and $E(p)$. Since, $p = j\omega$, it can be rewritten to the form

$$j(\omega) = E(\omega)\left[\sigma_0 + j\omega\varepsilon_0 (1 + F(\omega))\right]. \tag{72}$$

Thus, the dielectric response function $f(t)$ is the time domain of the frequency dependant susceptibility $\chi(\omega)$, which is defined as the Fourier transform of the dielectric response function $f(t)$, so it can be written

$$\chi(\omega) = F(\omega) = \chi'(\omega) - j\chi''(\omega) = \int_0^\infty f(t) \exp(-j\omega)\, dt. \tag{73}$$

Now, the frequency dependant polarization can be expressed as

$$P(\omega) = \varepsilon_0 \chi(\omega) E(\omega). \tag{74}$$

The equation 63 can be transformed to

$$j(\omega) = \sigma_0 E(\omega) + j\omega D(\omega) \tag{75}$$

and using the equations (56) and (73) it can be expressed

$$\begin{aligned} j(\omega) &= \left\{ \sigma_0 + i\omega\varepsilon_0 \left[1 + \chi'(\omega) - j\chi''(\omega)\right] \right\} E(\omega) \\ &= \left\{ \sigma_0 + \varepsilon_0\omega\chi''(\omega) + i\omega\varepsilon_0 \left[1 + \chi''(\omega)\right] \right\} E(\omega). \end{aligned} \tag{76}$$

The frequency dependant electric displacement can be now expressed using the complex relative permittivity

$$D(\omega) = \varepsilon_0\varepsilon_r(\omega) E(\omega) = \varepsilon_0 \left[1 + \chi'(\omega) - j\chi''(\omega)\right] E(\omega), \tag{77}$$

where

$$\varepsilon_r(\omega) = \varepsilon_r'(\omega) - j\varepsilon_r''(\omega) = \left(1 + \chi'(\omega)\right) - j\chi''(\omega). \tag{78}$$

For a practical determination of the dielectric response function from the equation (76), there is no measurement equipment able to distinguish between the current contribution of the dielectric conductivity and that caused by the dielectric loss [15]. That simple means, that the effective measured permittivity $\tilde{\varepsilon}_r$ is different from the relative permittivity used in equations (76) and (77). If the effective relative permittivity is defined by the equation

$$j(\omega) = j\omega\varepsilon_0\tilde{\varepsilon}_r(\omega) E(\omega), \tag{79}$$

then

$$\begin{aligned} \tilde{\varepsilon}_r(\omega) &= \varepsilon_r'(\omega) - i\left[\varepsilon_r''(\omega) + \frac{\sigma_0}{\varepsilon_0\omega}\right] \\ &= 1 + \chi'(\omega) - j\left[\chi''(\omega) + \frac{\sigma_0}{\varepsilon_0\omega}\right]. \end{aligned} \tag{80}$$

The real part of the equation defines the electric capacitance of the tested dielectric sample and the imaginary part represents the losses. Both of the quantities are frequency dependant. Finally, the dissipation factor can be expressed as

$$\tan\delta(\omega) = \frac{\varepsilon_r''(\omega) + \sigma_0/\varepsilon_0\omega}{\varepsilon_r'(\omega)}. \tag{81}$$

2.1.4. Related definitions

Recommended terms related to dielectric spectroscopy are defined in an IEEE standard. The following definitions are mentioned in [20].

- **Absorption (polarization) current** (I_A): A current resulting from molecular polarizing and electron drift, which decays with the time of voltage application at a decreasing rate from a comparatively high initial value to nearly zero, and depends on the type and condition of the bonding material used in the insulation system.
- **Conduction current** (I_G): A current that is constant in time, that passes through the bulk insulation from the grounded surface to the high-voltage conductor, and that depends on the type of bonding material used in the insulation system.

- **Electroendosmosis effect**: A phenomenon occasionally observed, more often on older windings, when, in the presence of moisture, different insulation resistance values may be obtained when the polarity of the tester leads are reversed. Typically for older wet windings, the insulation resistance for reverse polarity, where the ground lead is connected to the winding and the negative voltage lead to the ground, is much higher than for normal polarity.
- **Insulation resistance** (IR_t): The capability of the electrical insulation of a winding to resist the direct current. The quotient of the applied direct voltage of negative polarity divided by the current across machine insulation was corrected to 40 °C and taken at a specified time (t) from the start of voltage application. The voltage application time is usually 1 min (IR_1) or 10 min (IR_{10}), however, other values can be used. Unit conventions: values of 1 through 10 are assumed to be in minutes, values of 15 and greater are assumed to be in seconds.
- **Geometric capacitive current** (I_C): A reversible current of comparatively high magnitude and short duration, which decays exponentially with the time of voltage application, and which depends on the internal resistance of the measuring instrument and the geometric capacitance of the winding.
- **Polarization index** ($PI_{t2/t1}$): Variation in the value of insulation resistance with time. The quotient of the insulation resistance at time (t_2) divided by the insulation resistance at time (t_1). If times t_2 and t_1 are not specified, they are assumed to be 10 min and 1 min, respectively. Unit conventions: values of 1 through 10 are assumed to be in minutes, values of 15 and greater are assumed to be in seconds (e.g., $PI_{60/15}$ refers to IR_{60s}/IR_{15s}).
- **Surface leakage current** (I_L): A current that is constant with time, and which usually exists over the surface of the end-turns of the stator winding or between exposed conductors and the rotor body in insulated rotor windings. The magnitude of the surface leakage current is dependent upon temperature and the amount of conductive material, i.e., moisture or contamination on the surface of the insulation.

2.2. Measuring instruments

The market offers several types of instruments intended for both time domain and frequency domain spectroscopy. The instruments are supplied with all necessary cables for the DUT connection and evaluation software. In the following text, three of them will be described.

2.2.1. Omicron Dirana

The Omicron Dirana instrument combines both time and frequency domain spectroscopy analysis in one piece of instrument [21]. Combining these two methods it is rapidly decreased the time of measurement. The view of the instrument is shown in Fig. 22. The basic parameters of the Dirana instrument are stated in Table 2.

2.2.2. Omicron Spectano 100

The Omicron Spectano is a measurements instrument also utilizing both time and frequency domain spectroscopy methods. The photograph of the instrument is shown in Fig. 23.

Figure 22. View of the instruments Dirana manufactured by Omicron [21]

Table 2. The basic parameters of Dirana

Number of inputs	2
Capacitance range	10 pF - 100 µF
Capacitance accuracy	0.5% + 1 pF
Dissipation factor range	0 - 10
Dissipation factor accuracy	1% + 3×10^{-4}, 1 mHz < f < 100 Hz 2% + 5×10^{-4}, f <1 mHz and f > 100 Hz
Time domain Current Measurements	
Range	± 20 mA
Resolution	0.1 pA
Accuracy	0.5 % ± 1 pA
Outputs	
Max. voltage range	0 - 200 V peak
Max. current range	0 - 50 mA peak
Frequency range	50 µHz - 5 kHz

Figure 23. View of the Spectano 100 instrument manufactured by Omicron [22]

Table 3. The basic parameters of Spectano 100

Number of inputs	1
Capacitance range	10 pF - 100 µF
Capacitance accuracy	0.5% + 1 pF
Dissipation factor range	0 - 10
Dissipation factor accuracy	1% + 3×10^{-4}, 1 mHz < f < 100 Hz 2% + 5×10^{-4}, f <1 mHz and f > 100 Hz
Time domain Current Measurements	
Range	± 10 mA
Resolution	0.1 pA
Accuracy	0.5 % ± 1 pA
Outputs	
Max. voltage range	0 - 200 V peak
Max. current range	0 - 50 mA peak
Frequency range	50 µHz - 5 kHz

2.2.3. Megger IDAX 300/350

Megger IDAX 300 and 350 are insulation diagnostic analyzers. The instruments provide power frequency tan delta / power factor measurement, power frequency capacitance measurements, DC insulation testing (insulation resistance, polarization index, and dielectric absorption ratio) [23]. The maximum test voltage is 200 V DC and peak AC. The output voltage can be amplified using an optional HV amplifier up to 2 kV DC and peak AC. The photograph of the instruments is shown in Fig. 24. The basic instruments parameters are stated in Table4.

Figure 24. View of the instruments IDAX 300 and IDAX 350 manufactured by Megger [23]

Table 4. The basic parameters of IDAX 300 and 350

Number of inputs	2
Capacitance range	10 pF - 100 µF
Capacitance accuracy	0.5% + 1 pF
Dissipation factor range	0 - 10
Dissipation factor accuracy	< 0.5% + 0.0002, 45 - 70 Hz, C > 300 pF < 1% + 0.0003, 1 mHz - 100 Hz, C > 1000 pF < 2% + 0.0005, 100 Hz - 1 kHz, C > 1000 pF
Time domain Current Measurements	
Range	± 20 mA
Resolution	0.1 pA
Accuracy	0.5 % ± 1 pA
Outputs	
Max. voltage range	0 - 200 V peak
Max. current range	0 - 50 mA peak
Frequency range	DC - 10 kHz

2.3. Other Diagnostic methods

The insulation of the high voltage machines can be made of various materials. The insulation material can be solid, liquid, gas, or a combination of these such as paper impregnated with oil. These materials should possess good insulating properties over a wide range of operating parameters, such as a wide temperature range and a wide frequency range [4]. Since it is difficult to test the materials in the whole range of operation. It is also expected that the measured material is not destructed during the measuring procedure.

2.3.1. DC resistivity measurement

There is shown a measuring circuit of the DC resistivity of an insulation specimen in Fig. 25. The insulation specimen is formed by a material with a defined shape so that the resistivity could be easily calculated [4]. To reduce the surface conductivity effect the specimen connection is realized with three electrodes. An unguarded electrode is connected to the high potential of a supply voltage. The unguarded electrode completely covers the specimen surface. There is a smaller guarded electrode surrounded by a guard electrode on the bottom of the specimen. The guarded electrode forms the second measuring pole and the guard electrode is connected to the ground.

The specimen is excited with a high voltage source. The supply voltage is measured by a voltmeter V. The flowing current produces a voltage drop on a resistor R_{sh}. The measured specimen resistivity is then given by

$$R = \frac{V}{V_{sh}} R_{sh}. \tag{82}$$

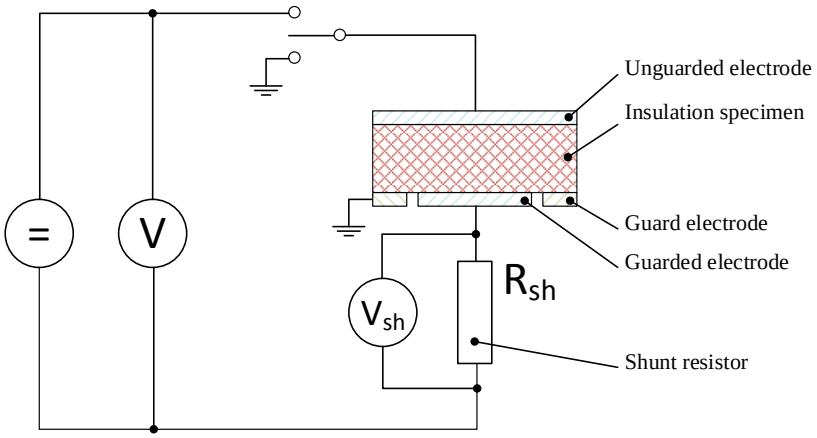

Figure 25. Measuring of DC resistivity

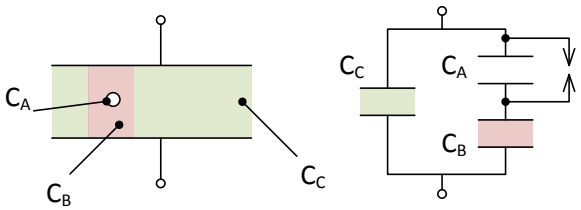

Figure 26. Insulation void equivalent circuit, similar picture in [4]

2.3.2. Partial discharge measurement

It was found that weak points in insulation like voids, cracks, and other imperfections lead to internal or intermittent discharges in the insulation [4]. In modern terminology, they are called partial discharges. The partial discharges over time could cause a reduction of insulation strength, a partial failure, or even the breakdown of the insulation.

The electrical imperfections or voids can be represented by a simplified equivalent circuit shown in Fig. 26. Consider a void in the insulation with capacitance C_A. The capacitance C_A is a series with the rest of the capacitance C_B. The C_C represents a void-free capacitance. When the voltage across the capacitor raise and voltage across the capacitor C_A exceeds a critical value a discharge occurs through the capacitor C_A. A charge that was present in the capacitor C_A flows through C_B and C_C and produces a voltage pulse across the capacitor C_C.

The often-used definition of partial discharge according to [4] is: Partial discharge is an electrical discharge that only partially bridges the dielectric or insulating medium between two conductors. Examples are internal discharges, surface discharges, and corona discharges.

There exist electrical, chemical, acoustic, or optical measurement methods for the detection of partial discharges. The electrical methods are based on a measurement of electrical resonance caused by partial discharges excitations. The frequency range of the measurement is up to 1.5 GHz [24]. This method is capable to detect and locate the source of partial discharge source.

The chemical methods are based on collecting a chemical measuring of oil and gas samples released during the partial discharge occurrence. The samples have to be collected and then chemical analysis can start. Due to this reason, the chemical methods are not suitable for real-time monitoring.

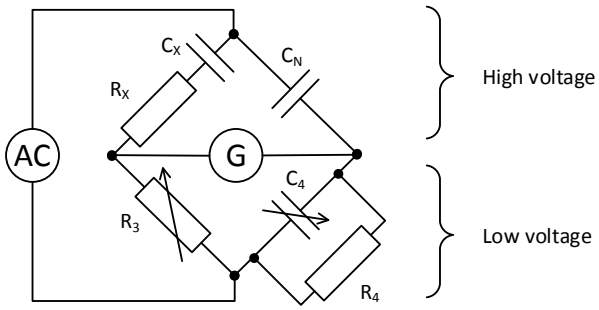

Figure 27. Principle circuit of the Schering bridge, similar picture in [25]

The acoustic methods study the propagation of the acoustic waves generated by the partial discharge. The acoustic waves are detected using acoustic sensors, e.g. piezoelectric sensors. The sensor could be placed inside the tested device into the oil tank representing liquid machine insulation. The location of the partial discharge occurrence is estimated by measuring the time of travel of the acoustic waves and position information about all used sensors.

The optical methods utilize optical fiber sensors. The main advantages of these sensors are small size, high sensitivity, lightweight, high-frequency response and high immunity against the electromagnetic interference [24]. The optical detection is based on fiber optic intrinsic interferometers. Due to the measurement sensitivity, the optical method has restricted use for partial discharge detection.

2.3.3. Capacitance and dissipation factor measurement

Capacitance and dissipation factors are material and equipment depending on values. Their trends could give hints for changes in the machine or insulation material. For example, increasing the capacitance of bushing or capacitors could be a result of the discharge between partial capacitances inside the equipment. An increasing dissipation factor could come from increasing humidity or structural changes caused by aging. Also, the high partial discharge inception could be detected by an increasing the dissipation factor [25].

One of the commonly used measuring techniques is a usage of a Shering bridge. A principle circuit of the Schering bridge is shown in Fig. 27. The measured impedance is represented by the capacitor C_X and the resistor R_X. The measured impedance is compared with the normal capacitor C_N with known capacitance and dissipation factor. The bridge is balanced using the elements R_3 and C_4. The advantage is the balancing elements do not have to be dimensioned for high voltage. A balanced state is indicated by indicator G. When indicators display zero value the measured capacitance and dissipation factor can be expressed as

$$C_X = C_N \frac{R_4}{R_3}, \tag{83}$$

$$\tan \delta = \omega C_4 R_4. \tag{84}$$

The second discussed method is direct current measurement. This method is based on the calculation of the capacitance and the dissipation factor using a directly measured current vector. The simplified schematic is shown in Fig. 28. The measured impedance is also represented by a capacitor C_X and a resistor R_X. It is connected

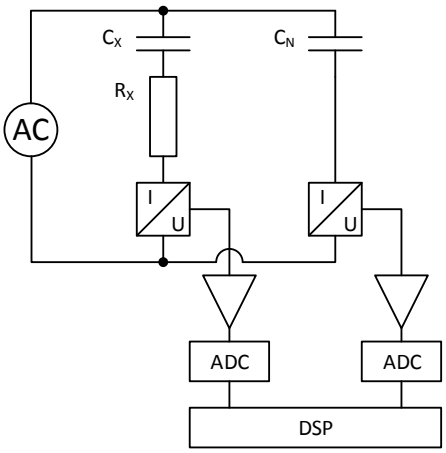

Figure 28. Principle circuit of the digital capacitance and dissipation factor method

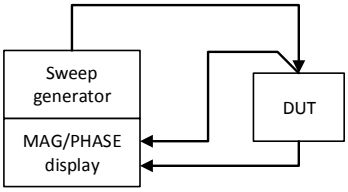

Figure 29. Principle circuit of the frequency response analysis method

to a high voltage AC source along with a normal capacitor C_N. The currents flowing through the measured impedance and the normal capacitor are converted to voltages using appropriate I to U converters. The analog to digital converters (ADC) provide a conversion of the voltages into the digital form. Digital signal processing (DSP) provides computation of the capacitance and the dissipation factor using the known currents magnitudes, phases, and the normal impedance. The measured impedance is hence given by

$$\mathbf{Z_X} = \frac{\mathbf{I_N}}{\mathbf{I_X}}\mathbf{Z_N}. \tag{85}$$

2.3.4. Frequency response analysis

A frequency response analysis (FRA) is a method based on measuring how well is the transformer winding able to transmit a low voltage signal that varies in frequency [26]. Changes in the frequency response measured by the FRA method may indicate a physical change inside the transformer or a failure. A loss of mechanical integrity may occur due to large mechanical forces caused by fault currents, a winding shrinkage causing the release of clamping pressure, transformer transportation or relocation, and also from some external causes such as lightning stroke, etc.

The simplified measuring circuit is shown in Fig. 29. The device under test (DUT) represents the tested object, for example, transformer winding. The DUT is excited by the sweep generator. The generator produces a signal with a voltage of tens of volts and varying frequency. The voltage on the DUT terminal and the output current is measured. A block diagram of the FRA analyzer and the connection to the DUT

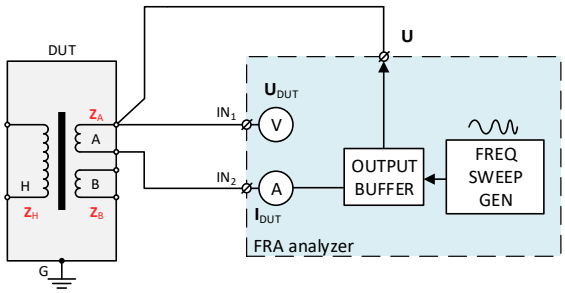

Figure 30. A block diagram of the frequency response analyzer

is shown in Fig. 30. The method analyzes how the winding electrical impedance is changing with the frequency of the excitation signal. The electric impedance can be then expressed as

$$\mathbf{Z_X}\left(\omega\right) = \frac{\mathbf{U}_{DUT}}{\mathbf{I}_{DUT}\left(\omega\right)}, \tag{86}$$

where $\mathbf{Z_X}$ is the measured winding footprint, $\mathbf{U}_{DUT}$ is excitation voltage measured on DUT terminal and $\mathbf{I}_{DUT}$ is measured current flowing through the examined winding.

The measured impedance characteristic can be considered as a footprint of a particular winding. The operator of the transformer then studies how the footprint changes over the transformer duty period. If changes occur in the footprint it can be interpreted as upcoming or even present failure of the particular winding.

3. Aims of the Doctoral Thesis

The main aim of the thesis is to improve the parameters of the instrumentation used in the field of dielectric spectroscopy (DSP) of high voltage machines. The special interest was intended to the improvement of the accuracy and repeatability of the instrumentation. This thesis is a partial result of larger scientific teamwork dealing with a high voltage machine diagnostic in a wider scope. Besides DSP, our scientific group is interested in the Frequency Responses Analysis (FRA) as well. Hence, other efforts have been developed to try to design a hardware instrumentation platform suitable for both the DSP and FRA method.

The first goal of the thesis is to perform market research of the DSP instrumentation for HV machines. The research should contain an identification of the parameters to be improved. The research should act as a set of requirements for the next goal.

The most important goal of the thesis is to design the hardware instrumentation platform. Due to the high complexity of such a design, the work was divided between the author of the thesis and the author's co-worker Ing. Ján Tomlain. Therefore, special care should be intended to clarify a delegation of the work among particular researchers. It was decided to design the platform as a modular type and to split the platform into four functional blocks. Each functional block is carried by a single printed circuit board (PCB). The platform topology is depicted in Fig. 31. The role of a power supply block is to deliver a necessary power supply for all other blocks. The motherboard serves as the main computation unit and provides a communication interface between the platform and a control PC application. A daughterboard is equipped with ADC and DAC circuits necessary to comply with the requirements found out in the previous goal. Finally, an excitation board acts as an interface between the platform and a device under test (DUT). The design of the power supply unit, excitation board, and motherboard was delegated to Mr. Tomlain. The design of the daughterboard was delegated to the author as Fig. 31 shows. This topology has several advantages. Each block or module can be designed separately therefore, a redesign of the whole platform is not needed in case of a mistake made during the design work. And secondly, if any improvements have been needed, it would affect only a particular block.

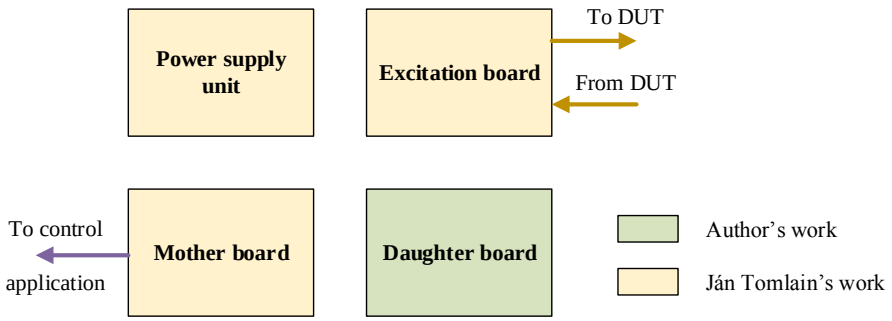

Figure 31. Topology of the platform functional blocks.

Modern instrumentation has no or very limited user interface, in contrast with older instrumentations with classic seven-segment displays and numbers of buttons, knobs, and LEDs. These controls usually occupied a lot of room on the instrumentation panel and made the instrumentation even larger. Today's trends show an effort to reduce the physical controls situated on the panel of the instrumentation. Instead, the instrumentation is delivered with a control software application fully substituting the old-style controls. Due to these circumstances, our research group decided to follow these trends. Therefore, the next goal of this thesis is to develop a control PC application to make the user be able to act with the instrument. The application should be cross-platform to cover a wide range of potential users. It has to implement the necessary communication interfaces to establish a reliable and fast connection with the instrument. Finally, because the hardware platform is supposed to be covering both DSP and FRA methods, the application has to implement all computation necessary to fulfill both methods' requirements. Hence, there would be only one control application needed for both methods.

Last but not least goal of the thesis is to perform a proper evaluation of the prosed instrumentation system. The first tests are expected to be performed in laboratory conditions. These tests should reveal the platform suitability for the measuring methods and confirm the parameters given in the previous goals. Field experiments should follow laboratory tests. The field experiments should be performed on real objects in the real environment. These tests will review all the instrumentation systems from the instrumentation DUT interface up to the control application.

To conclude all thesis goals and sub-goals the following list is stated.

1. To make an overview of the DSP method and market research of existed instrumentations.

2. To design the hardware platform of the instrumentation.
   a) To delegate the work amount among the research team.
   b) To identify the key parameters and possibilities of improvement.
   c) To design the electric schematic of the daughter board.
   d) To design a printed circuit board of the daughter board.
   e) To create FPGA VHDL design collecting the data from ADCs.

3. To design the control application.
   a) To ensure a cross-platform functionality.
   b) To implement the computations necessary for DSP and FRA methods.
   c) To design a graphic user interface to display the results of the measurements.
   d) To design a communication protocol for the platform.

4. To examine the measurement uncertainties.
   a) To derive equations leading to uncertainties evaluation.
   b) To perform computations to quantify measurement uncertainties.

5. To verify the platform functionality.
   a) To perform laboratory tests.
   b) To perform field tests with real tested objects.

6. To propose an evaluation method of measured dataset.

4. Hardware Platform

This thesis is a partial result of a scientific project covering larger scope in the field of non-destructive diagnostics of high voltage machines. The scientific team involved in the project, the author was a member of, was dealing with FDS and FRA method. The initial goal of the project was to develop a separate hardware platform for FDS and FRA methods and try to improve the precision parameters of existing instruments performing these methods. These topics also intersect the goals of this thesis, one of them is to develop an FDS hardware platform.

If we make a survey of the FDS and FRA instrument block diagrams shown in Fig. 20 and Fig. 30, we could observe several similar blocks. Both of the diagrams consist of a frequency sweep generator (FSG). The FSG output signal is amplified in both cases. However, in the case of FDS, a high voltage amplifier is used to obtain higher excitation voltage, which can be covered by an external HV amplifier. Both of the diagrams need two measurement channels. In the case of FDS the channels measure electric current and in the case of FRA one channel is intended for voltage measurement. These similarities led the scientific team to a decision to develop one hardware platform for both FDS and FRA methods. The platform would consist of blocks required by the measuring methods such as FSG, output buffer, and input channels capable to measure vectors of electric current or voltage. The next requirements have been related to user interaction with the platform and instrument powering with emphasis on battery power possibility.

The concept of the platform performing the FDS measurement is outlined in Fig. 32. The hardware platform is shown on the left side of the figure. The FSG output is amplified by a high voltage amplifier and the amplified signal is led into the desired device under test (DUT) terminal and into the normal impedance. The second terminal of the DUT and the normal impedance are led back to the instrument platform to analog to digital (ADC) inputs. Since the ADC inputs are voltage inputs, sensing resistors are necessary to convert electric current to voltage. The measured signals are processed on the platform and sent to a control application for user interaction.

Fig. 33 shows the platform performing the FRA method for the illustration. The HV amplifier is removed due to the lower voltage level (tens of Volts) required for the FRA method. In contrast with the FDS method, the ADC input 1 measures voltage, therefore the sensing resistor adjacent to the ADC input 1 is also removed. Comparing the Fig. 32 and Fig. 33 reader can see the utilization of the platform performing both measurement methods.

The requirements on the platform yielded to a quite complex hardware design, the development of which can be very difficult and time-consuming. Consequently, the scientific team decided to split the design into several parts represented by printed circuit boards. One reason for splitting the design was the workload of the development can be distributed among the scientific team more effectively. The multi PCB topology can also take advantage if an error in PCB occurs in the development stage. In that case, only one PCB needs to be redesigned which saves manufacturing and human resources costs.

The platform was split into four PCBs, namely a power supply unit (PSU), a motherboard, a daughterboard, and an excitation board. The complex diagram showing the

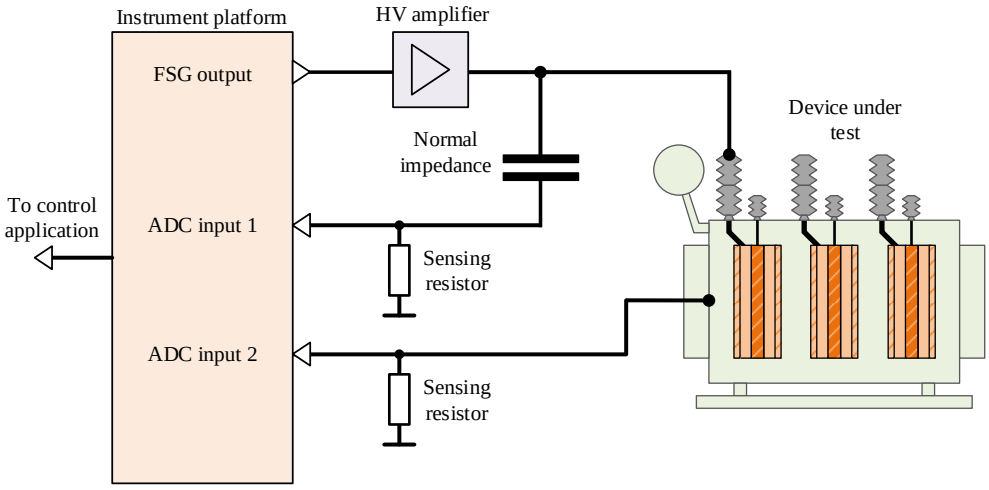

Figure 32. Connection schematic of the platform and the device under test for FDS method.

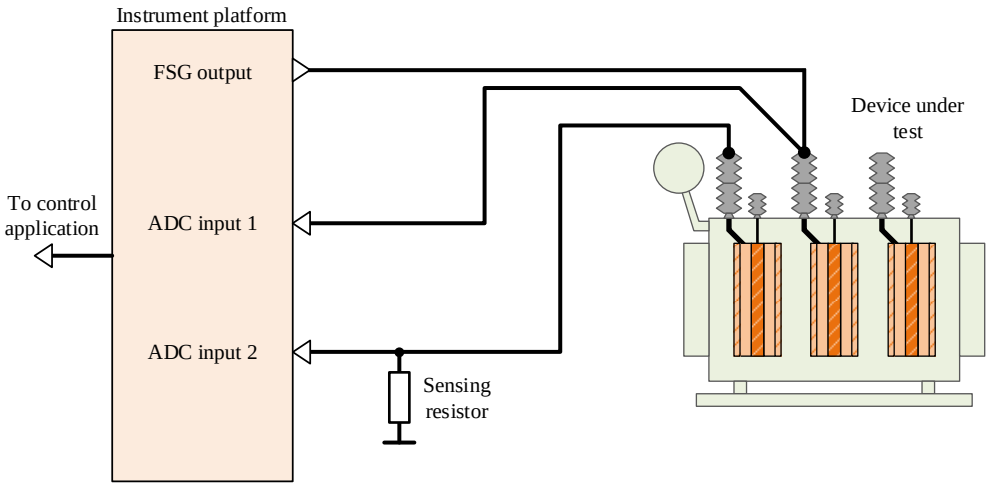

Figure 33. Connection schematic of the platform and the device under test for FRA method.

interconnection of all of the PCBs is shown in Fig. 34. The PSU board consists of four LiIon batteries connected to two serial and two parallel formations. The board also consists of a battery charger allowing to charge the batteries from an external 12 V power supply adapter. There are also power conditioning circuits placed on the board providing a battery management function.

The motherboard serves as the main unit of the instrument platform. The main task of the motherboard is to manage and process the data from the daughterboard, control the communication with the PC control application, and provide service information on the in-built LCD. A detailed block diagram of the motherboard is shown in Fig. 35. The central part of the motherboard is a field-programmable gate array (FPGA) of family Arria V manufactured by the Altera company. The reason for the FPGA choice was that the FPGA can perform parallel computation tasks in contrast with convenient

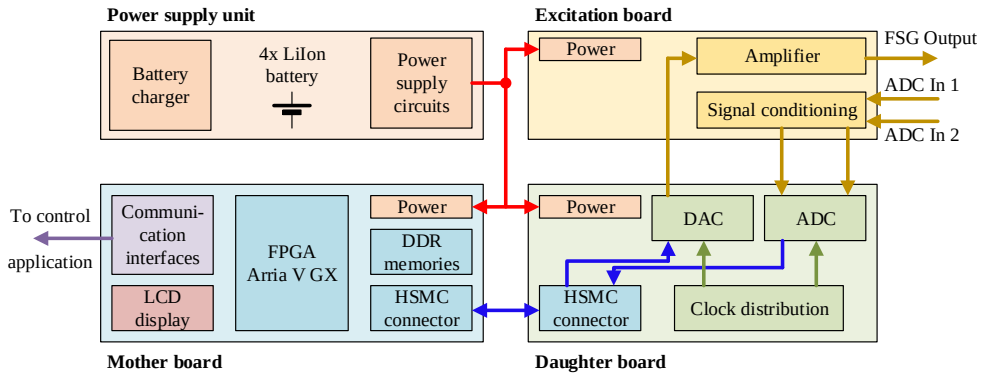

Figure 34. Topology of the instrument platform printed circuit boards.

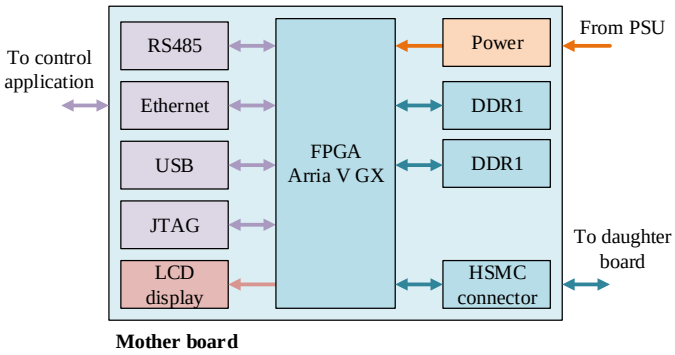

Figure 35. A detailed block diagram of the motherboard

processors. It means, the FPGA can for instance read two analog-to-digital converters in one moment, then store the measured data and send it to the further process while driving the DAC output value at the same time. The motherboard is also equipped with two DDR memories intended for storing the sampled data. There are also Ethernet, USB, and RS485 communication interfaces. The Ethernet interface is used for communication with the control application over the TCP/IP protocol. A high-speed mezzanine connector (HSMC) is used for interconnection between the motherboard and the daughterboard. The communication interfaces of the DAC and the ADC are directly connected to the FPGA via the HSMC. The FPGA controls the reading of the DAC samples and the output value of the DAC.

The daughterboard provides necessary analog to digital conversions and vice versa to fulfill the FDS method requirements. If it occurs the DAC and ADC are not suitable for the instrument for some reason, it has to be redesigned only on this board. This is the next advantage of the split PCB design. The detailed description of the daughterboard is stated in Chapter 4.1 because it is the author's main contribution to the scientific project.

The excitation board acts as a signal conditioning part for the daughterboard. There is an amplifier placed on the board that filters and amplifies the signal from the DAC placed on the daughterboard. The amplified signal is then led into the output connector

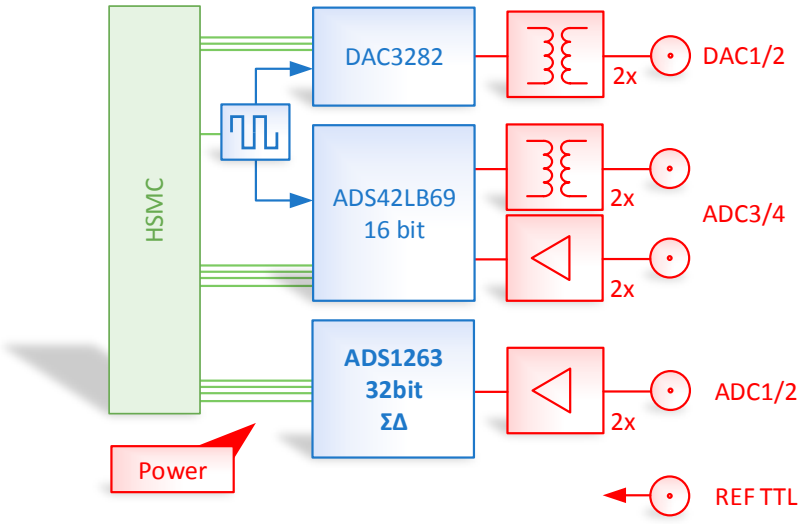

Figure 36. The block diagram of the designed analog front-end board

of the instrument platform. Also, the signals led from the DUT are preprocessed on the board and then led into ADCs placed on the daughterboard.

Thesis aim No. 2a refers to a work delegation among members of the scientific team. Based on the members' experience and preferences it was decided the author's task will be a design of the daughter board and development of the PC control application. Therefore, this thesis will further deal with the daughterboard only. The other boards were designed by Mr. Ján Tomlain, another member of the scientific team. The detailed description of these boards is one of the parts of his doctoral thesis. The description of the PC control application is the topic of Chapter 5.

4.1. Daughter Board Design

A board equipped with analog-to-digital (ADC) and digital-to-analog (DAC) converters was designed. The board is mainly intended for the measurement method described in chapter 2.1.3. A block diagram of the board is shown in Fig. 36 and a 3D model of the designed front-end is shown in Fig. 37.

The board consists of one dual-channel DAC type DAC3282 (16-bit, 625 Msps). Its output is led to an SMA connector. The board is also equipped with two dual-channel ADC. The first ADC is type ADS42LB69 with 16-bit resolution and 250 Msps sampling rate. An input signal is led from the SMA connector is coupled to both AC (transformers) and DC (operational amplifier) ways. This topology allows using the ADC in a wide frequency range of the input signals. The second ADC was used type dual-channel ADS1263 with a 32-bit resolution, maximum sampling rate 38 ksps, and a sigma-delta architecture. In comparison with the first ADC, it provides better resolution and accuracy in the range of low frequencies.

Clock impulses for DAC and ADC are generated using a circuit Si5338. The Si5338 is a programmable any-output any-frequency quad clock generator. The board also contains all necessary power supply circuits. The power supply circuits provide all

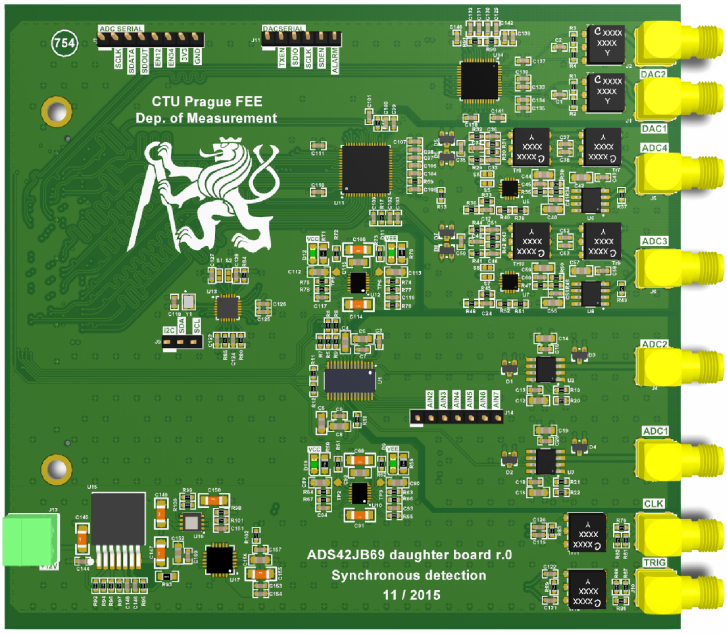

Figure 37. The 3D model of the designed front-end

voltage levels for ADC, DAC, and signal preconditioning for analog circuits. A REFTTL signal is led into a high-speed mezzanine connector HSMC is proposed to a sensing of a square wave reference signal. This can be used for internal phase-locked loop synchronization. An HSMC connector is used as an interconnection between daughter and motherboard.

4.1.1. Power Circuits

The power circuits supply energy to the other electric components placed on the daughterboard. Since the daughterboard is a very complex piece of hardware there is a lot of specific integrated circuits demanding various power supply voltage levels. The main power of the daughterboard is supplied from the PSU board in form of 12 V voltage level. The other voltage levels are derived from 12 voltage level input. A topology of the power supplies derivation is shown in Fig. 38. There are two 3.3 V voltage levels one for digital and one for analog circuits. Both of the levels have their ferrite bead filters. The same topology is repeated in the case of 1.8 V levels. These levels are used to supply the ADCs. Finally, there are power circuits used to generate 2.5 V and -2.5 V voltage levels. They are used to supply preconditioning circuits situated between the ADCs inputs and the input connectors. To be the supplies as close as possible to the ADCs, each ADC has its power circuit.

4.1.2. Analog to Digital Converters

The measuring platform is designed for a relatively wide measuring bandwidth to cover the requirements of both FRA and DSP methods. Merging the bandwidth intervals leads to a range of units of millihertz up to hundreds of megahertz. It could be very difficult to cover such a bandwidth with one analog to digital converter (ADC). Therefore two ADCs had been chosen to be placed on the daughterboard. An ADS1263 had been chosen for lower frequencies and an ADS42LB69 for higher frequencies.

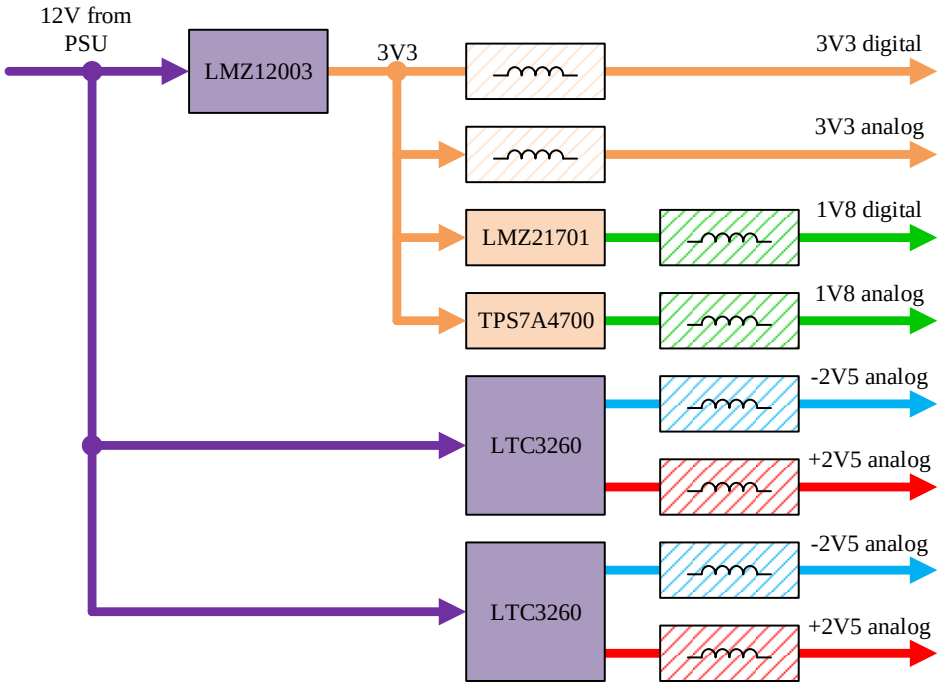

Figure 38. Topology of the power circuits.

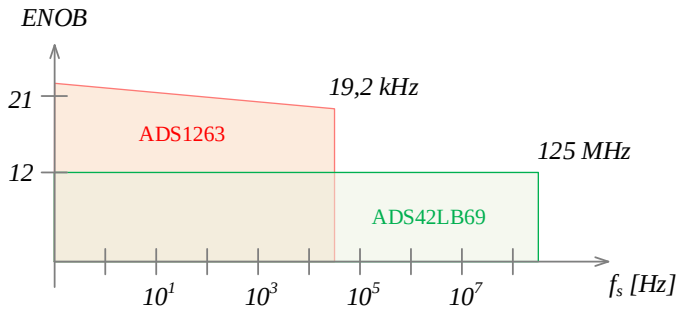

Figure 39. Comparison of ENOB versus bandwidth of the ADCs used.

A comparison of an effective number of bits (ENOB) versus frequency bandwidth of the ADCs is shown in Fig. 39. The ADS1263 is a low noise delta-sigma architecture with internal voltage reference, programmable gain amplifier (PGA), and fault monitoring. It offers 32 bits resolution with a sampling rate of up to 38.400 kSPS. The ENOB value is decreasing from 22 down to 20 bits with increasing sampling rate [27]. The dependence is outlined in the figure by the red polygon. The ADS42LB69 is a high linearity dual-channel ADC. If offers a 14-bits resolution with a maximum 250 MSPS sampling rate. The ADS provides a double data rate (DDR) or quadruple data rate (QDR) LVDS interface. If offers an ENOB of 20 bits [28]. The ENOB of the ADS is outlined by a green polygon in the figure.

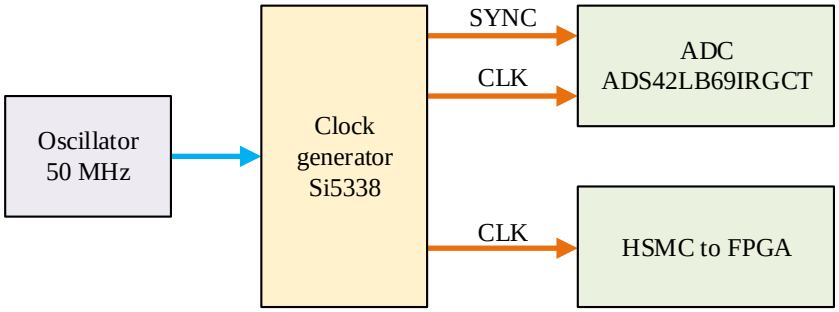

Figure 40. The clock distribution topology.

4.1.3. Digital to Analog Converter

According to chapter 2.1.3, the FDS method requires a frequency sweep generator. The designed platform implements the generator consisting of a digital to analog converter (DAC), analog output circuits, and a software block implementing a direct digital synthesis (DDS) algorithm. A detailed description of the DDS is out of the scope of this thesis and it can be found for instance in [29].

A DAC904 manufactured by Texas Instruments was chosen. The DAC904 is a 14-bit converter with an internal voltage reference and current output utilizing a current steering technique. The DAC offers up to a 165 MSPS sampling rate. It is equipped with a parallel 14-bit communication interface [30].

4.1.4. Clock Distribution Circuit

The daughterboard is equipped with a fast analog to digital converter, in which sampling frequency can rise to 250 MSPS. For the correct function of the converter proper clock signal generation and distribution has to be ensured. Usually, for such high frequencies, the required frequency is not generated directly. Instead, an oscillator with lower frequency (tens of megahertz) is used and this signal is led into a phased locked loop (PLL) circuit. The PLL is a circuit multiplying the input frequency, with an adjustable multiplying factor. Fundamentals of the PLL architecture can be found in [31].

Fig. 40 shows the clock generation and distribution solution how it is used on the daughterboard. An oscillator with an output frequency of 50 MHz is used as a source of the clock signal. This signal is then led into a clock generator circuit Si5338. The Si5338 is an I^2C programmable clock generator capable of synthesizing four independent user-programmable output frequencies up to 350 MHz. The output drivers supply four differential clock outputs or eight single-ended output or a combination of both types. The drivers can be configured into several common output formats such as LVPECL, LVDS, HCSL, CMOS, HSTL, and SSTL [32].

The clock distribution topology of the daughterboard shows that three output channels of the clock generator are used. All three output channels are set as LVDS outputs. Two of them are led into the ADC inputs SYNC and CLK. The SYNC input is usually used for the synchronization of more ADCs on the board and in this case, the SYNC input could be left floating. The CLK input of the ADC is a standard clock input used for synchronization of the internal ADC circuits and control of the input analog signal

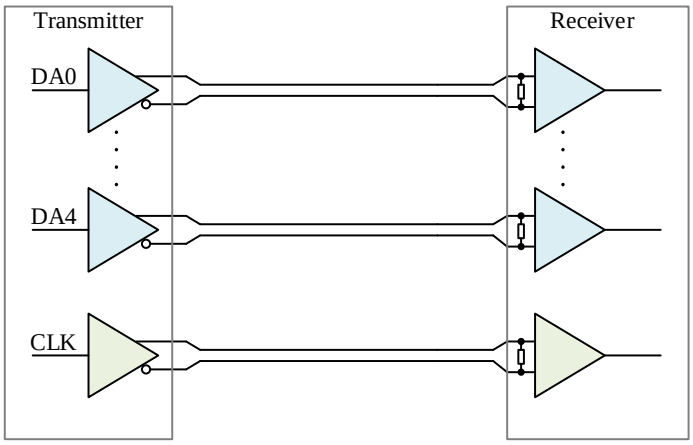

Figure 41. The LVDS interface topology example.

sampling. The third output of the clock generator is led into the HSMC connector and therefore to the FPGA located on the motherboard. This signal serves to provide the time synchronization for the FPGA.

4.1.5. LVDS Communication Interface

The LVDS is a communication interface capable of high-speed transmission of the binary over the copper wires on the printed circuit board (PCB). The LVDS interface consists of several differential data pairs and a differential clock output [33]. The logic level of the pair is then given by a direction of the current flow through the wire pair. The main advantage of the differential pairs topology, the transmission line is much resistive against the external electromagnetic noise and also it emits much less electromagnetic noise to the surrounding environment. A typical example of the LVDS pairs topology with four data pairs and one clock pair is shown in Fig. 41. Four data bits are transmitted each time during one period of the clock output.

4.1.6. Printed Circuit Board Layout

The first step of any PCB design should be a brief outline of the board layout. Especially if the board consists of very fast integrated circuits, mixed-signal circuits, and transmission lines. There is a lot of literature dealing with this topic. A pretty comprehensive overview of the problems with high-speed PCB design can be found in [34].

The proposed design of the measuring platform consists of fast digital converters, analog circuits, and even transmission lines carrying the communication between the converters and the FPGA. The fast digital circuits produce current peaks from the power supply circuits when the output pins change the logic level. The higher frequency of the changes the high effect of power transmission. This phenomenon may harm analog circuits connected to the same power transmission. The current peaks can transfer to the input conditioning circuit through the power transmission and it can influence the measured analog quantity. Hence, the accuracy of the measurement is rapidly decreased. Therefore, it is necessary to strictly separate all analog circuits from the other.

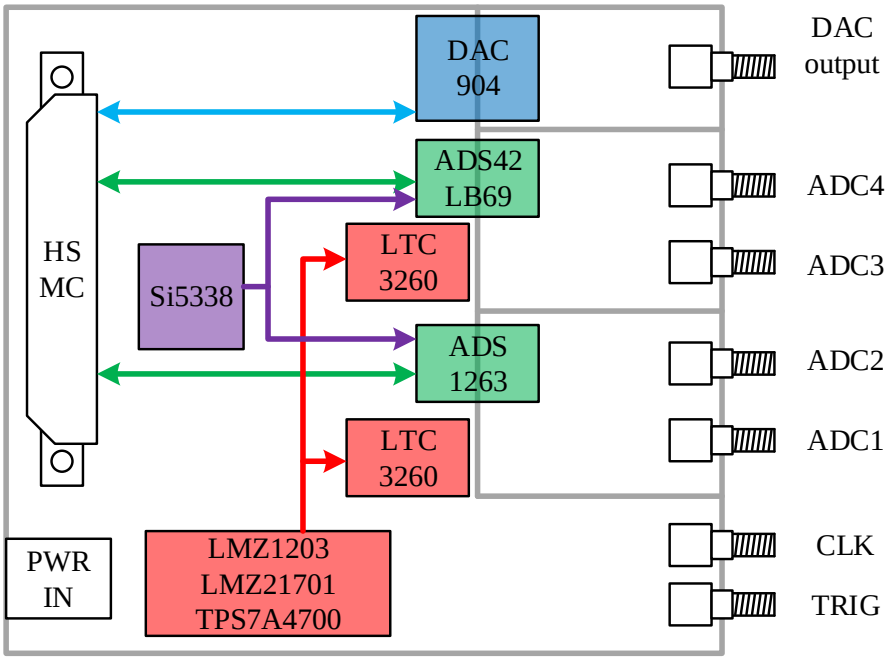

Figure 42. Board layout schematic of the daughter board.

Fig. 42 shows the schematic of the daughterboard layout. It can be noticed, the DAC and DACs have their section of the PCB. The grey line below the converters depicts isolation barriers. The converters are placed with their digital parts on the left side of the isolation area and with their analog part on the right side of the isolation area. The converters have their input conditioning circuits. These circuits need a power supply too. To ensure the power supply does not affect the other converter, there are two separated power supplies (LTC3260) for both of the ADCs (see Fig. 38). These circuits are supplied from the LMZ1203 power supply situated on the left bottom side of the board near the power supply input connector.

The daughterboard is designed to fit the motherboard dimensions and to be possible to enclose the board into an industry-made aluminum enclosure. Special attention was paid to the ergonomic assembling of the device. The photograph of the connected mother and daughter board is shown in Fig. 43.

4.2. Platform Software and VHDL design

The role of the proposed hardware platform is to provide measured data for the control application which is used for solving the equation (69). Once, the measured electric impedance has been computed the capacitance and the dissipation factor can be derived. The equation (69) requires vectors of measured electric current. Therefore, the platform VHDL design has to implement an algorithm capable to measure both amplitude and phase shift of the measured channels. The VHDL design also implements a System On Chip NIOS processor. The role of the NIOS is to collect data from VHDL data and interact with PC control application.

A basic vector voltmeter implementation was designed to provide vector-based elec-

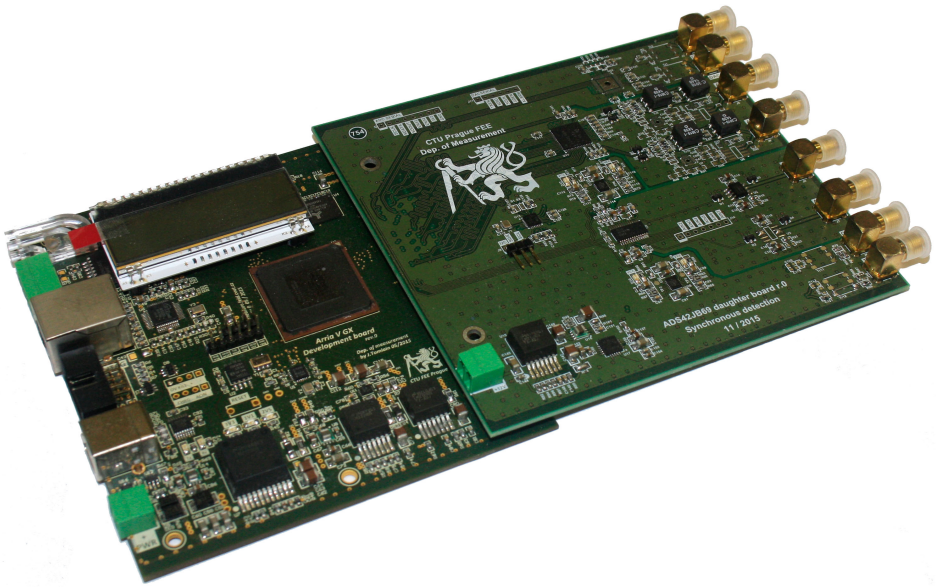

Figure 43. The photograph of the connected motherboard and the daughterboard.

tric current measurement from ADC data. The implementation is running on the motherboard utilizing the daughterboard measured data provided via HSMC. A brief principle of the used algorithm is shown in Fig. 44 and it is also well-known as a lock-in amplifier (LIA). The algorithm consists of two multipliers, two low pass filters, and a phase shifter. U_S is an input sinus wave signal and U_R is a reference sinus wave signal.

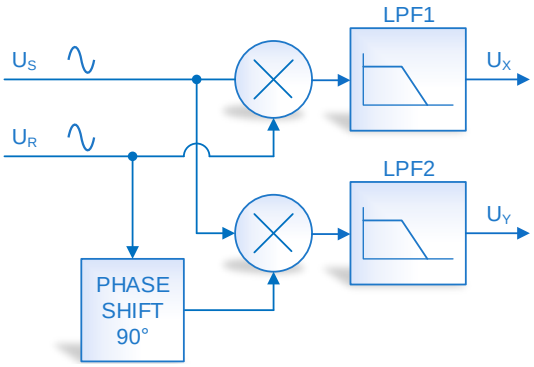

Figure 44. The principle of the lock-in amplifier

Then the output signals U_X and U_Y can be expressed as

$$\begin{aligned} U_X = &\frac{1}{2}U_S U_R \cos\left[(\omega_S - \omega_R)\, t + \theta_S - \theta_R\right] - \\ &\frac{1}{2}U_S U_R \cos\left[(\omega_S + \omega_R)\, t + \theta_S + \theta_R\right] \end{aligned} \tag{87}$$

$$\begin{aligned} U_Y = &\frac{1}{2}U_S U_R \sin\left[(\omega_S + \omega_R)\, t + \theta_S + \theta_R\right] + \\ &\frac{1}{2}U_S U_R \sin\left[(\omega_S - \omega_R)\, t + \theta_S - \theta_R\right] \end{aligned} \tag{88}$$

where ω_S, ω_R are natural frequencies of the signals U_S and U_R, θ_S θ_R are phase shift of the signals. Supposing that $\omega_S = \omega_R$ and after filtration the frequency $\omega_S + \omega_R$ using LPF1 and LPF2 we get output signals

$$U_X = \frac{1}{2} U_S U_R \cos\left[\theta_S - \theta_R\right] \tag{89}$$

$$U_Y = \frac{1}{2} U_S U_R \sin\left[\theta_S - \theta_R\right] \tag{90}$$

that indicates that the output signal U_X is proportional to a real part of the input signal and the output signal U_Y is proportional to an imaginary part of the input signal.

A block diagram of a VHDL implementation suitable for the motherboard is shown in Fig. 45. An ADS1263 VHDL driver provides an interface between ADC and FPGA circuits. Sampled data are continuously provided in the bus data. The sampled data are multiplied in multiplier MUL32. The second input of the multiplier is fed by an all-digital phase-locked loop PLL. The PLL generates a sine wave and a cosine wave digital waveform with a phase shift respected to the REF signal. The filtration of the frequency $\omega_S + \omega_R$ is provided by a PERAVG and a MOVAVG filter. The PERAVG is designed as an average of one period of the input signal and MOVAVG is designed as a moving average filter. The filtered signal proportional to the real and imaginary part of the input data is led into a NIOS processor block.

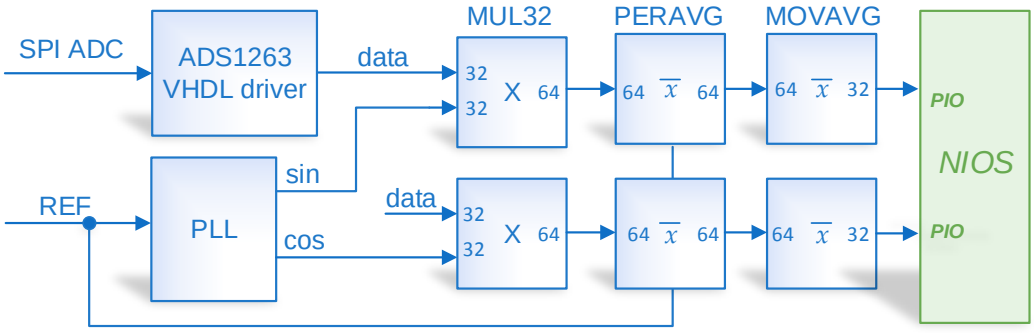

Figure 45. The VHDL implementation of one channel LIA

An overview of the complete software equipment of the proposed platform is outlined in Fig. 46. The VHDL blocks are drawn blue colored and the NIOS block is drawn, green colored. The NIOS processor implements a communication protocol used for interaction with the PC control application. The detailed description of the protocol is stated in Chapter 5.1. The PC control application determines a frequency set point. NIOS then retranslates the setpoint to the DDS algorithm block. The DDS generates a data set of a sine wave with desired frequency and also generates the reference signal for two LIA blocks. The DAC3282 LVDS driver block feeds the DAC with data from the DDS block.

The DAC generated signal returns through the normal capacitance to the CH1 input and DUT to CH2 input (see Fig. 32). The block ADS1263 SPI driver and ADS42 LVDS driver is responsible for data collection from both AD converters. Each of the AD has two channels. Channel 1 of each AD measures the normal capacitance current and Channel 2 measures the DUT current. The data collected by the drivers are led to the LIA block through two multiplexers. The multiplexers are controlled by

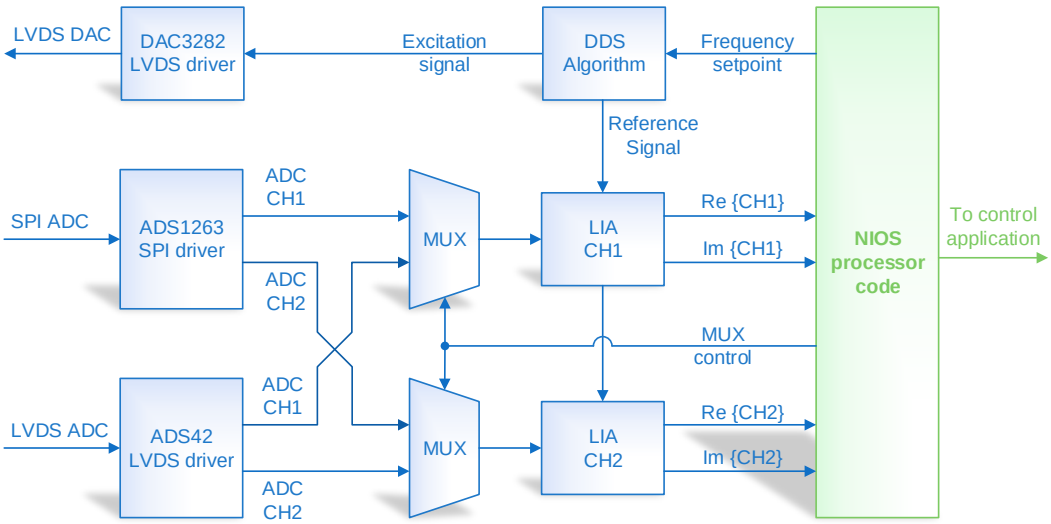

Figure 46. The overview of complete platform software

the NIOS processor concerning the excitation signal frequency. If Nyquist–Shannon sampling theorem can adhere the AD1263 is preferred due to the higher ENOB value. Otherwise, the data from ADS42 are used. Two LIA block implements the algorithm as it is shown in Fig. 45 and decomposed both input current into its real and imaginary parts. NIOS processor sends these values to the PC control application.

4.3. Summary

This chapter describes the ideas that led the members of the scientific team to design and develop the measuring hardware platform. A team has been established and work has been delegated to each member which corresponds to aim No. 2a. It was shown how the platform can be used for FDS and FRA methods. The team identified this feature together with improving measuring precision as the main improvement of the current State of The Art (aim No. 2b). The physical topology of the platform has been introduced and reasons for the topology choice have been stated.

The proposed platform consists of four PCBs each of which had to be designed. Based on the workload delegation the schematic and PCB has been created and manufactured. The author's responsibility has been the development of the daughterboard (aims No. 2c and 2d). The software and VHDL design of the platform has been described. The main role of the software is to interact with the PC control application. Based on the commands issued by the application the software drives the DDS algorithm, ADC data collection, and decomposition of the measured currents into its real and imaginary parts (aim No. 2e). The decomposed values are sent to the application for further processing.

The four PCBs and the software equipment form the hardware platform for measuring instruments capable of battery operation and providing features enabling the user to perform the FDS and FRA method. However, the capacitance and the dissipation factor values are not computed by the platform itself. The platform computes only vectors of the measured currents. Performing the rest of the computation is the role of the PC control application. The description of the application is the topic of the next chapter.

5. Software Equipment

The software equipment of the measuring platform provides an interface between the user and the instrument. It consists of a control application and a communication protocol. The control application is designed as a multi-platform application. Using the application the user can control the instrument, read and manage the results of the measurements. The communication protocol defines the way how the application communicates with the instrument on a hardware layer. A brief description of these interface features is stated in further text.

5.1. Communication Protocol

Today trends in measurement instrumentation show, that the classic human-to-machine interface consisting of buttons, switches, LEDs, or displays mounted on the front panel of the instruments is fading away. The instrument manufacturers prefer to create a virtual instrument panel, represented by a computer application instead. The user can install the virtual panel into his computer and then directly control the instrument to set measuring ranges, read out the measured values and control another function the instrument provides.

Technically, to fulfill the requirement the virtual panel can interact with the instrument, a communication interface has to be defined. The physical OSI (Open System Interconnection model) layer of the interface can be formed by one of the most used interfaces of today's computers, for instance, USB or Ethernet. On the other hand, the RS232 and the GPIB physical interfaces are not suitable for today's application, because there are fewer and fewer computers equipped with these interfaces and therefore it is necessary to use an interface converter.

The higher communication layers can be implemented by the manufacturer proprietary. Nevertheless, there are efforts to standardize these communication layers. For example, LXI Consortium defines a standard using the Ethernet connection recommend for instrumentation devices [35]. They can be mentioned in other widely used industry standards such as Modbus [36] or IEC 60870-5 [37].

For the testing platform purposes, it has been chosen a proper communication protocol. The LXI and the IEC 60870-5 are very complex protocols and it would be very time-consuming to implement such extensive protocols. So the first author's choice was to use the Modbus protocol. The protocol utilized strictly separated data and command parts. It means the server holds a memory space of input and output variables and the client can read or write them. There are defined separate commands to write and read from the specified address of the memory space. Therefore, there it is not necessary to implement a special command type when a new server value is required to be defined. On the other hand, the protocol implements only two types of variables binary and sixteen-bit numbers. The protocol also does not support an asynchronous event. It means, when an event occurs, that changes a particular output variable, the client has to explicitly ask for the value. Since our scientific team is working on projects which require processing the asynchronous events, it was decided a proprietary protocol will be designed, however, inspired by Modbus protocol.

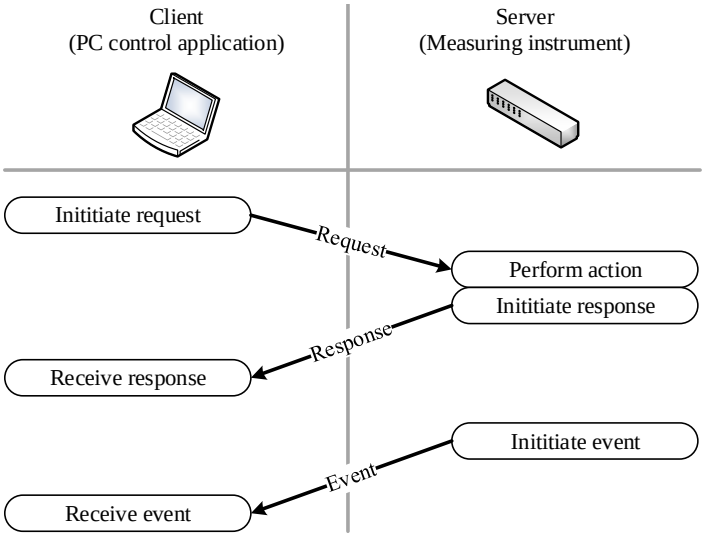

Figure 47. Client-Server topology and protocol transaction

The designed protocol can be used over TCP/IP or USB Virtual COM port (VCP) layer. An example of communication transactions is shown in Fig. 47. A detailed description of the protocol is stated in Appendix A. However, all reader needs to know is the control application can write frequency set points to the platform and collect measured electric current value decomposed to its real and imaginary parts.

5.2. Control Application

As it was outlined in Chapter 5.1, most modern instruments utilized virtual instruments which allow the remote control of the instruments via PC. The instrument manufacturers provide an application that the user can install on his computer and he can easily control the instrument, read out the measured data, and even store it in many different ways. This form of control allows huge flexibility for the instrument developer. This was one of the reasons to implement such a virtual instrument in this thesis.

The main requirements for the control application are stabile communicate with the instrument and to provide necessary information for the user. From the communication point of view, the application has to use one of the most used communication interfaces for PC (such as USB or Ethernet, see Figure 48). This makes the user comfortable because there is no necessity to use any kind of interface converter. The last but not least task for the control application is to read the data from the instrument, compute necessary quantities and display the data on the PC screen.

5.2.1. Application Framework

There is a lot of application development framework on the market. Based on the author's experience a Qt framework has been chosen to develop the instrument control application. The Qt is a cross-platform, graphic, application development toolkit that enables developers to compile and run applications on a variety of operating systems such as Windows, Mac OS X, Linux, and Unix [38]. It was originally developed as an extension for C++ language. A comprehensive overview of the C++ language

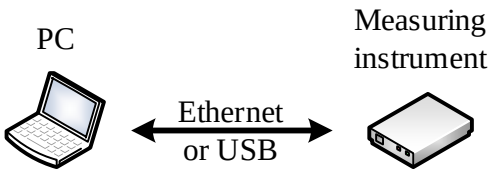

Figure 48. Instrument connection topology.

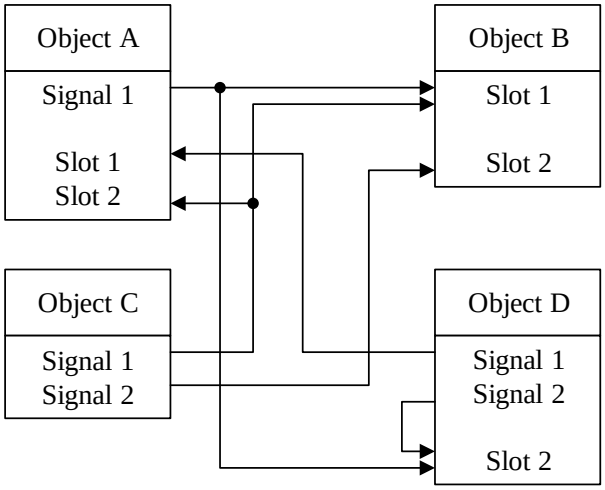

Figure 49. Example of the signals and slots interconnection mechanism.

can be found in [39] or in [40]. The Qt framework is distributed with a very strong development tool Qt Creator. It enables a rapid GUI application development. A very detailed overview of how to use the Qt Creator can be found in [41].

One of the hugest strengths of the Qt frameworks are signals and slots features, which is a very flexible way how to interconnect objects while helping to keep the code clear and reusable. A signal is a method emitted (not executed) when an event occurs. As the event can be understood a situation when the user clicked on the button, hovered the mouse above a particular area, or even when data arrived via TCP socket. There is no implementation of the signal method allowed, just a declaration of the method.

A slot is a member function declared in a special section of the class declaration, which can be used as a reaction to an emitted signal. In the contrast with the signal, the slot has to have its implementation. To declare which slot has to react to which signal, it is necessary to connect the signal with the slot. Usually, it is executed in a part of the code when the application is initializing, but it is also possible to connect the slots during the application run time and even disconnect existing connections. There can be data transmitted over the signal and slot connection. For example, when the user changes the text in a line edit field, the changed text can be transmitted over the connection and the slot implementation does not need to access the line edit value. Generally, the single slot can be connected to many signals and the single signal can be connected to many slots. An example of one of the interconnection possibilities is shown in Fig. 49.

Table 5. Server data space for float data type.

Float address	Unit	Description
0	V	Channel 1 - Real part of the measure voltage
1	V	Channel 1 - Imaginary part of the measure voltage
2	V	Channel 2 - Real part of the measure voltage
3	V	Channel 2 - Imaginary part of the measure voltage
4	Hz	Frequency of the output sine wave generator

Table 6. Server data space for uint8 data type.

Uint8 address	Unit	Description
0	-	On/Off output channel (0 - ON, 1 - OFF)

5.2.2. Measurement Calculations

There were computational requirements for the DSP method outlined in the Chapter 2.1. The hardware measuring platform described in the Chapter 4.1 and 4.2 is designed to fit these requirements and ensure a low computational load of the hardware. Therefore, a lot of calculations are performed in the PC control application instead. A data interface between the control application and the hardware platform should be designed. In the other words, it had to be defined which data or quantities will be transmitted to the control application to ensure all of the necessary quantities for the FDS method can be computed.

As it was stated in Chapter 4.2, the main role of the platform is to act as a remote control frequency sweep generator and the dual-channel vector ammeter at the same time. Therefore, the data interface can be formed by setting the frequency of the output signal wave and reading both channel voltage vector components.

Table 5 documents an address map of the float data type. The first four address serves to hold the measured voltage values of both of the channels decomposed to their real and imaginary values. All of these values are represented in the Volt unit. The last value of the data space serves to set the output sine wave frequency and the value is represented in the Hertz unit. To ensure the application can turn on and off the output signal an uint8 data space contains one value to control the output, see Table 6. Writing one to the zero address of the uint8 data space causes turning on the output signal with a frequency defined by address four of the float data space.

As it was stated in the previous chapters, one FDS measurement is represented by a set of electrical capacitance and dissipation factors at a given excitation frequency. It can be understood, the FDS measurement consists of several single-frequency measurements (measurement points). Each of the measurement points determines two voltage vectors for the frequency setting. The hardware platform is designed to perform only one single frequency measurement at each time. Therefore, it is necessary to serialize the single measurements at the time. A flowchart showing the process of the FDS measurement is shown in Fig. 50. Once, the measurement is started, the application creates the measurements point. It means a set of frequencies is generated for each measurement point. For a detailed description of the creation of measurement, points see Chapter 5.2.3. Then, the frequency of the first measurement point is set to the instrument and the output sine wave generator is turned on. After some user-specified

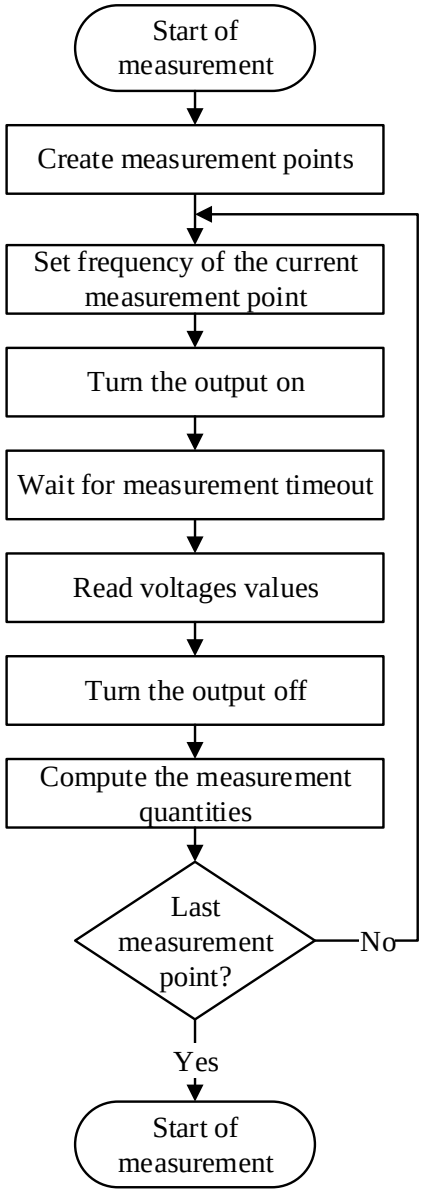

Figure 50. DSP measurement flow chart.

time, the voltage values are read, the output generator is turned off and all necessary FDS quantities are computed. This process repeats until all of the measurement points are performed.

According to the previous chapters dealing with the theory, a lot of calculations works with complex numbers. To make the programming clear and comfortable it was necessary to choose a proper object representation of the complex numbers. Therefore, a C++ class defining the complex number has been written. The class defines complex numbers using rectangular or polar forms. It also provides transformation between these forms. The class further provides basic math operations such as addition, subtraction, multiplication, division, reading the module, and the angle of the complex number. For more comfortable work operator member functions have been declared as it is shown in the listing below.

```
ComplexNumber operator+(const ComplexNumber &other);
ComplexNumber operator+(const float &other);
ComplexNumber operator-(const ComplexNumber &other);
ComplexNumber operator-(const float &other);
ComplexNumber operator*(const ComplexNumber &other);
ComplexNumber operator*(const float &other);
ComplexNumber operator/(const ComplexNumber &other);
ComplexNumber operator/(const float &other);
```

These operator member functions allow using standard binary operators (+, -, *, /) for mathematical operation over the complex number data type. Therefore, it is possible to use a notation as it is shown in the listing below.

```
ComplexNumber A(10, 1);          // A = 10 + 1i
ComplexNumber B(5, -14);         // B = 5 - 14i
ComplexNumber C = A + B;
ComplexNumber D = A*B + A/B;
ComplexNumber E = A*5 + B*8;
```

Once the electric current data is received, the application performs the calculations based on the following equation

$$\mathbf{Z}_x = \mathbf{Z}_n \left(\frac{\mathbf{U}_1}{\mathbf{U}_2} - 1 \right), \tag{91}$$

where $\mathbf{Z}_x$ is an unknown impedance, $\mathbf{Z}_n$ is the reference impedance with known and stable parameters, $\mathbf{U}_1$ and $\mathbf{U}_2$ are the measured voltage vectors. Once, the unknown impedance is determine, the electrical capacitance and the dissipation factor can be computed using the known excitation frequency and equations stated in Chapter 1.1.7. During the measurement the application draws a diagram of the measured valued. Hence, the user can watch the progress of the measurement online.

5.2.3. Graphical User Interface

The proposed instrument platform has been designed to be capable to perform FDS and FRA methods as well. Therefore, the PC control application has been created concerning the requirements of both methods. A screenshot of the main window of the control application is shown in Fig. 51. There is the main toolbar at the top of the window. The toolbar consists of several buttons. The first button on the left side is a connect button. The connect button serves to trigger the application to attempt of establishing the connection with the instrument. When the application is started, the state of the instrument connection is set to the Disconnected state. Once, the connect button on the main toolbar is clicked, the instrument proceeds to an Opening state. The application tries to open a TCP socket. If the socket open procedure fails, the instrument connection state returns to the Disconnected state. Otherwise, it proceeds to a Connecting state. Then the application tries to issue a protocol request. The request can be formed by reading a value from the instrument data space or issuing a ping command. If the response is not received within one second, the instrument connection status returns to the Disconnected state. If the application receives the response it

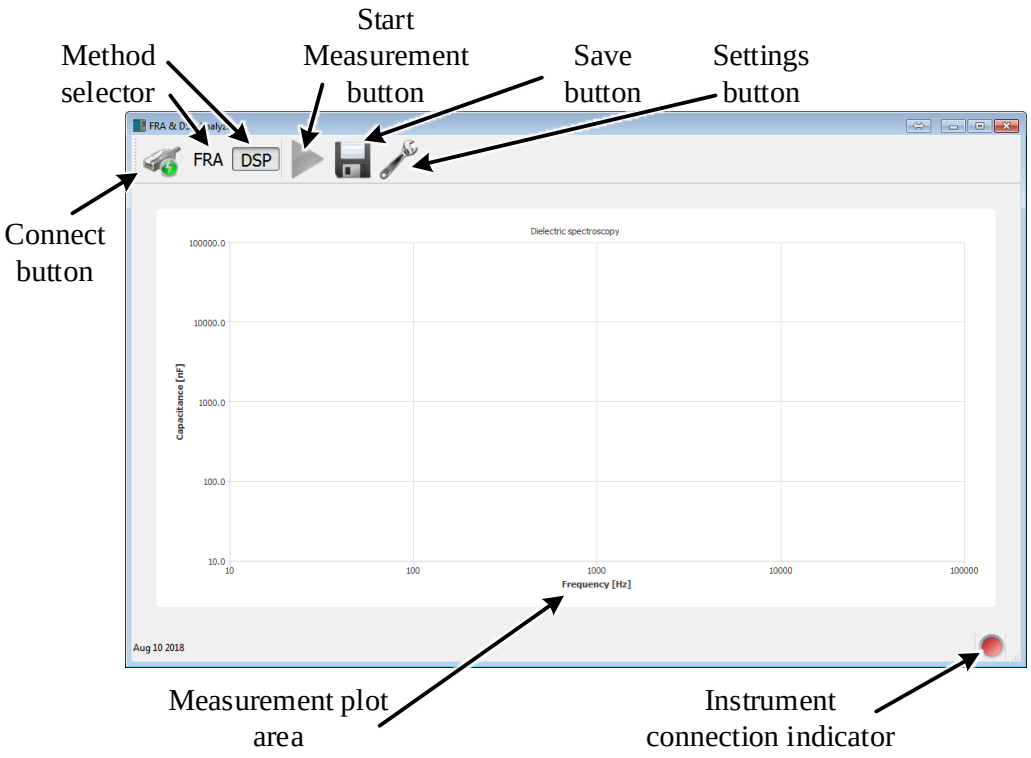

Figure 51. Screenshot of the control application main window.

can be understood as the instrument is reacting via the communication properly and the instrument connection status proceeds to a Connected state. If there is a need to connect to the PC more instruments implementing the communication protocol, can be distinguished by the different IP addresses of the local network. When the instrument connection status is in the Connected state, the application sends periodically every one second a ping request. If the instrument does not respond within one second, it causes the closing of the socket and the instrument connection status returns to the Disconnected state. The disconnection of the instrument can be also performed by clicking on the Disconnect button which is the same button as the Connect button.

The user is informed about the current instrument connection state by an instrument connection indicator. The indicator is situated at the bottom right corner of the application main window (see Fig. 51). The indicator is drawn as a three-state LED and each state is indicated by a different color.

The next GUI control is a Method selector (see Fig. 51). As it was mentioned at the beginning of this chapter, the control application was designed to perform both the DSP and the FRA method. The method selector serves to choose which measurement method has to be performed. The selector consists of two excluding buttons which means only one button can be checked at each time.

There is a start measurement button next to the method selector. The start button serves to initiate the measurement sequence following the flowchart shown in Fig. 50. When the user clicks the start button, the measurement procedure starts and the button changes its icon to a blue rectangle indicating a stop of the measurement function. So, the user can stop the procedure at each moment of the measurement procedure. However, if the measurement is stopped before its proper end, the measured values are

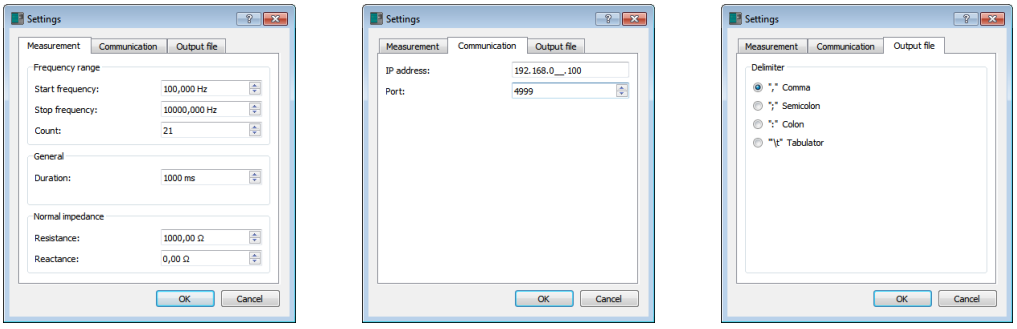

(a) Measurement settings **(b)** Communication settings **(c)** Output file settings

Figure 52. Screenshot of the application settings dialog.

discarded.

The next button of the main toolbar is a save button. Clicking on the button shows a save file dialog demanding a file name to save the measured values. The format of the saved file can be partly user modified and it is further described in the text below. A setting button served to show an application settings dialog. The dialog consists of three tabs, see Fig. 52.

The measurement parameters can be set on a measurement tab. A screenshot of the measurement tab is shown in Fig. 52a. A frequency range section consists of three spin boxes setting the frequency range of the measurement. The user can set a start frequency, stop frequency, and several measurement points. The application then computes the particular frequency for every single measurement point, so that the frequencies are equidistantly distributed over the set range on the logarithmic axis. Each frequency point could be then expressed as

$$f_i = 10^{\frac{\log(f_{stop})-\log(f_{start})}{N-1}\cdot i+\log(f_{start})}, \tag{92}$$

where f_{start} is the starting frequency, f_{stop} is the stop frequency, N is the number of the measurement points required and i is an index of the particular measurement point.

A general section allows setting a duration of one measurement point. It means the time between turning on the output generator and readout of the measured values, see the *Wait for measurement timeout* procedure at flowchart shown in Fig. 50. The last section allows setting the normal impedance used in the equation (91). The user can type the resistance and the reactance of the normal impedance. The vector of the normal impedance is then defined as

$$\mathbf{Z}_n = R_n - jX_n, \tag{93}$$

where R_n is the resistance and X_n is the reactance of the normal impedance.

A communication tab offers basic communication parameters. A screenshot of the tab is shown in Fig. 52b. The user can set the IP address and TCP port of the measuring instrument.

A screenshot of an output file tab is shown in Fig. 52c. The tab offers to the user to choose a delimiter of the CSV file generated by the save button. The possible options are comma, semicolon, colon, and tabulator.

5.3. Summary

This chapter documents the software equipment of the platform. The hardware platform does not implement any knobs or display to interact with the user. It is equipped with LAN and USB interface instead. The control commands and data readout is done via the PC control application. The use of the PC application offers a much more flexible and comfortable solution in contrast with hardware parts such as knobs and displays situated on the hardware itself. These would have also a negative impact on the instrument's physical dimensions.

The PC control application has been designed to be cross-platform, which corresponds with the thesis aim No. 3a. It was one of the reasons for the choice of the Qt framework. It offers a development environment for every commonly used operating system. The application has been designed to provide computing for FDS and FRA methods. As it was stated in Chapter 4 the platform sends real and imaginary parts of the measured electric currents. Knowing the normal capacitance value, the application can determine the vector of electrical impedance. Then, the capacitance and dissipation factor is computed concerning the frequency of the excitation signal. The frequency is also sent from the platform in one bulk together with the electric current values. Once the vector of electrical impedance is determined, the application can also compute the impedance magnitude which is the quantity needed for the FRA method. Therefore, the application can provide computation for both methods, which directly corresponds to the thesis aim No. 3b.

When the necessary values are computed the application plots the results into a graph. The user can examine the diagram, store values, or decide to repeat the measurement with a changed set of the excitation frequencies if needed. The ability of the control application to handle the measured data corresponds to thesis aim No. 3c.

The way how the measured data are transferred from the platform to the PC application is a role of the communication protocol. A proprietary communication protocol has been designed for the platform. It corresponds with thesis aim No. 3d. The protocol has been inspired by the well-known standard Modbus TCP and offers all necessary functions to control the platform and collect the measured data. The control application together with the proposed instrument platforms forms, external HV amplifier, the normal capacitance, and the sensing resistors forms a complete measuring platform for the FDS method.

6. Measurement Uncertainty Analysis

As no man-made device or invention is perfect and efficient, no measurement instrument is absolutely accurate. In the other words, it is not possible to make a measurement not affected by any error. Therefore, we have to define a term measurement uncertainty. The uncertainty of the result of measurement reflects the lack of exact knowledge of the value of the measurand. The result of measurement after correction for recognized systematic effects is still only an estimate of the value of the measurand because of the uncertainty arising from random effects and imperfect correction of the result for systematic effects [42]. There can be various sources of measurement uncertainties, for example, the incomplete definition of the measured quantity, insufficient knowledge of phenomena affecting the quantity, parallax error, limited instrument resolution, reference inaccuracy, inaccurate constant values used from external sources, approximations, and assumption in measurement method [43].

There are two types of uncertainties. A type-A uncertainty (u_a) is obtained by statistical methods from the results of measurements made and its value decreases with an increasing number of repeated measurements. A type B uncertainty (u_b) is obtained by identification of known effect to the measured value. Its value is not affected by the increasing value of measurement repeated. If the result of the measurement is composed of various estimations and both types of uncertainties are involved, the resulting uncertainty is then called combined uncertainty (u_c). In some commercial, industrial and regulatory applications (especially where health and safety are concerned) it is necessary to count with a wider range of distribution of measured values. This value is then called an expanded uncertainty and it can be expressed as

$$U = ku_c(y), \tag{94}$$

where U is the expanded uncertainty, k is a coverage factor and $u(y)$ is the combined uncertainty of quantity y.

For further discussion about determining the type A and B uncertainty, it is useful to define the following variables. Let's suppose Y is an indirectly measured quantity and X_i is the directly measured quantity necessary to determine quantity Y, then

$$Y = f\left(X_1, X_2, \ldots, X_m\right), \tag{95}$$

where f is a known function. An estimation y of quantity Y is then

$$y = f\left(x_1, x_2, \ldots, x_m\right), \tag{96}$$

where $x_1, x_2, \ldots, x_m$ are estimations of quantities $X_1, X_2, \ldots, X_m$. If more than one measurement of the same quantity are concerned, than an arithmetic mean value of series of n measurements can be expressed as

$$\overline{y} = \frac{1}{n}\sum_{i=1}^{n} y_i, \tag{97}$$

where y_i represent particular measurement of quantity Y. Its standard uncertainty of type A is then the standard deviation, which can be expressed as

$$u_{Ay} = \sqrt{\frac{1}{n\,(n-1)} \sum_{i=1}^{n} (y - \overline{y})^2}, \tag{98}$$

where n is the number of measurement executed. The type B standard uncertainty can be estimated by scientific judgement based on all available information on the possible variability of X_i. The sources of information can be previous measurement data, experience with or general knowledge of the behaviour and properties of relevant materials and instruments, manufacturer's specification, data provided in calibration and other certificates, uncertainties assigned to reference data taken from handbooks. In general, assuming non correlated direct measured quantities X_i the type B standard uncertainty can be expressed as

$$u_{By} = \sqrt{\sum_{j=1}^{m} A_{y,xj}^2 u_{xj}^2}, \tag{99}$$

where u_{xj}^2 is type B uncertainty of determination of X_j quantity and

$$A_{y,xj} = \left. \frac{\partial f\,(X_1, \ldots, X_m)}{\partial X_j} \right|_{X_1 = x_1, \ldots X_m = x_m}. \tag{100}$$

The total standard uncertainty of determination of quantity Y is then expressed as

$$u_{Cy} = \sqrt{u_{Ay}^2 + u_{By}^2}. \tag{101}$$

This concludes with a very brief introduction to the determination of measurement uncertainties. Further text will discuss an analysis of a particular case study of the proposed instrument platform.

6.1. Platform Measurement Chain

The proposed platform does not measure the quantities required for dielectric spectroscopy directly, but rather measures the electric current flowing through the normal impedance and the DUT (see Chapter 4). Which implies that the equation (95) has to be considered in order to estimate the uncertainties. The following equations documents the overall computation flow from instrument input value to dissipation factor and capacitance. The serial equivalent circuit will be considered in further text (see Chapter 1.1.7). The dissipation factor can be expressed as

$$\tan \delta = \frac{Re\,\{\mathbf{Z_X}\}}{Im\,\{\mathbf{Z_X}\}} \tag{102}$$

where $\mathbf{Z_X}$ is the electric impedance of the studied insulation at particular frequency. The proposed instrument platform does not measure the impedance directly. Instead it measures a voltage proportional to the electric current flowing through to the measured impedance as it is shown in Fig. 32. Sensing resistors with resistance R_{sense} are used to convert the measured electric current to voltage and feed the inputs of the instrument platform. Moreover, the figure shows a layout where a normal impedance is used to eliminate the necessity to measure voltage on the measured impedance. Instead, two

currents are measured one flowing through the measured impedance $\mathbf{I_X}$ and the second current flowing through the normal impedance $\mathbf{I_X}$. Therefore, the measured impedance can be expressed as

$$\mathbf{Z_X} = \mathbf{Z_N}\frac{\mathbf{I_N}}{\mathbf{I_X}} = \mathbf{Z_N}\frac{\mathbf{U_{ADC1}}}{\mathbf{U_{ADC}2}} \cdot \frac{R_{sense1}}{R_{sense2}} \tag{103}$$

where $\mathbf{Z_N}$ is a vector of the normal impedance shown in Fig. 32, $\mathbf{U_{ADC1}}$ and $\mathbf{U_{ADC2}}$ are the vectors of voltages measured by the AD converters, R_{sense1} and R_{sense2} are electric resistances of the sensing resistors.

If we look at the vector values of the previous equations as number expressed in rectangular forms and execute all the multiplications and divisions than we can decompose the equation into real and imaginary part respectively. Assuming the resistance of the sensing resistors are equal or at least very close the real part of the measured impedance can be expressed as

$$\begin{aligned} Re\{\mathbf{Z_X}\} =& \frac{Re\{\mathbf{Z_N}\}Re\{\mathbf{I_N}\}Re\{\mathbf{I_X}\} - Im\{\mathbf{Z_N}\}Im\{\mathbf{I_N}\}Re\{\mathbf{I_X}\}}{Re\{\mathbf{I_X}\}^2 + Im\{\mathbf{I_X}\}^2} + \\ &+ \frac{Re\{\mathbf{Z_N}\}Im\{\mathbf{I_N}\}Im\{\mathbf{I_X}\} + Im\{\mathbf{Z_N}\}Re\{\mathbf{I_N}\}Im\{\mathbf{I_X}\}}{Re\{\mathbf{I_X}\}^2 + Im\{\mathbf{I_X}\}^2} \end{aligned} \tag{104}$$

and the imaginary of the measured impedance as

$$\begin{aligned} Im\{\mathbf{Z_X}\} =& \frac{Re\{\mathbf{Z_N}\}Im\{\mathbf{I_N}\}Re\{\mathbf{I_X}\} - Re\{\mathbf{Z_N}\}Re\{\mathbf{I_N}\}Im\{\mathbf{I_X}\}}{Re\{\mathbf{I_X}\}^2 + Im\{\mathbf{I_X}\}^2} + \\ &+ \frac{Im\{\mathbf{Z_N}\}Re\{\mathbf{I_N}\}Re\{\mathbf{I_X}\} + Im\{\mathbf{Z_N}\}Im\{\mathbf{I_N}\}Im\{\mathbf{I_X}\}}{Re\{\mathbf{I_X}\}^2 + Im\{\mathbf{I_X}\}^2}. \end{aligned} \tag{105}$$

Combining the equations (102), (104) and (105) we get

$$\begin{aligned} \tan\delta =& \frac{Re\{\mathbf{Z_N}\}Re\{\mathbf{I_N}\}Re\{\mathbf{I_X}\} - Im\{\mathbf{Z_N}\}Im\{\mathbf{I_N}\}Re\{\mathbf{I_X}\} + \cdots}{Re\{\mathbf{Z_N}\}Im\{\mathbf{I_N}\}Re\{\mathbf{I_X}\} - Re\{\mathbf{Z_N}\}Re\{\mathbf{I_N}\}Im\{\mathbf{I_X}\} + \cdots} \\ & \frac{\cdots + Re\{\mathbf{Z_N}\}Im\{\mathbf{I_N}\}Im\{\mathbf{I_X}\} + Im\{\mathbf{Z_N}\}Re\{\mathbf{I_N}\}Im\{\mathbf{I_X}\}}{\cdots + Im\{\mathbf{Z_N}\}Re\{\mathbf{I_N}\}Re\{\mathbf{I_X}\} + Im\{\mathbf{Z_N}\}Im\{\mathbf{I_N}\}Im\{\mathbf{I_X}\}} \end{aligned} \tag{106}$$

which express the total equation for dissipation factor computation for the instrument platform proposed.

The second quantity considered in the FDS method is the electric capacitance of the studied material. The general electric impedance can decompose to a resistor-capacitor equivalent circuit in two ways. It can be transformed into either serial or parallel circuits. In this section, we will deal with the serial equivalent circuit only. Therefore the capacitance taking part in the overall impedance can be expressed as

$$C_s = -\frac{1}{2\pi f Im\{\mathbf{Z_X}\}} \tag{107}$$

where C_S is a serial equivalent circuit capacitance of the studied material and f is frequency of the electrical current used to excite the studied material. Combining the

equation with (105) we get

$$\frac{1}{C_S} = \frac{-\omega Re\{\mathbf{Z_N}\} Im\{\mathbf{I_N}\} Re\{\mathbf{I_X}\} + \omega Re\{\mathbf{Z_N}\} Re\{\mathbf{I_N}\} Im\{\mathbf{I_X}\}}{Re\{\mathbf{I_X}\}^2 + Im\{\mathbf{I_X}\}^2} - \\ - \frac{\omega Im\{\mathbf{Z_N}\} Re\{\mathbf{I_N}\} Re\{\mathbf{I_X}\} + \omega Im\{\mathbf{Z_N}\} Im\{\mathbf{I_N}\} Im\{\mathbf{I_X}\}}{Re\{\mathbf{I_X}\}^2 + Im\{\mathbf{I_X}\}^2} \tag{108}$$

where ω is the natural frequency of the excitation current. The inverse value of the C_S has been shown due to typographic complexity of the fraction. Noting

$$\mathbf{I_N} = \mathbf{U_{ADC1}} R_{sense}, \tag{109}$$

$$\mathbf{I_X} = \mathbf{U_{ADC2}} R_{sense}, \tag{110}$$

equations (106) and (108) forms a complete set of equation to perform the FDS measurement. The measured values are $\mathbf{U_{ADC1}}$ and $\mathbf{U_{ADC1}}$ whereas $\mathbf{Z_N}$ and R_{sense} are constants.

For further investigation of the measurement uncertainties we will assume that we are able to determine the quantities $\mathbf{Z_N}$, R_{sense1} and R_{sense2} with uncertainties much more lower than uncertainty of the determination of $\mathbf{U_{ADC1}}$ and $\mathbf{U_{ADC2}}$. Then we will assume the time and temperature stability of the quantities $\mathbf{Z_N}$, R_{sense1} and R_{sense2} are so high that these do not have a negative effect on the measured value. Therefore uncertainties of these three quantities will be neglected. We will also neglect statistical uncertainties type A. Only type B will be considered. According to the equation (99) the total uncertainties of dissipation factor and capacitance can be expressed as

$$u_{\tan\delta} = \sqrt{\begin{array}{c} A^2_{\tan\delta, Re\{\mathbf{U_{ADC1}}\}} u^2_{Re\{\mathbf{U_{ADC1}}\}} + A^2_{\tan\delta, Im\{\mathbf{U_{ADC1}}\}} u^2_{Im\{\mathbf{U_{ADC1}}\}} + \\ + A^2_{\tan\delta, Re\{\mathbf{U_{ADC2}}\}} u^2_{Re\{\mathbf{U_{ADC2}}\}} + A^2_{\tan\delta, Im\{\mathbf{U_{ADC2}}\}} u^2_{Im\{\mathbf{U_{ADC2}}\}} \end{array}}, \tag{111}$$

$$u_{C_S} = \sqrt{\begin{array}{c} A^2_{C_S, Re\{\mathbf{U_{ADC1}}\}} u^2_{Re\{\mathbf{U_{ADC1}}\}} + A^2_{C_S, Im\{\mathbf{U_{ADC1}}\}} u^2_{Im\{\mathbf{U_{ADC1}}\}} + \\ + A^2_{C_S, Re\{\mathbf{U_{ADC2}}\}} u^2_{Re\{\mathbf{U_{ADC2}}\}} + A^2_{C_S, Im\{\mathbf{U_{ADC2}}\}} u^2_{Im\{\mathbf{U_{ADC2}}\}} \end{array}}. \tag{112}$$

The sensitivity factors can be expressed according to the equation (100). For clarity reason let's consider the following substitutions

$$\begin{aligned} a &= Re\{\mathbf{Z_N}\}, \\ b &= Im\{\mathbf{Z_N}\}, \\ c &= Re\{\mathbf{U_{ADC1}}\}, \\ d &= Im\{\mathbf{U_{ADC1}}\}, \\ e &= Re\{\mathbf{U_{ADC}}2\}, \\ f &= Im\{\mathbf{U_{ADC}}2\}. \end{aligned} \tag{113}$$

The the sensitivity factors can be expressed

$$A_{\tan\delta, Re\{\mathbf{U_{ADC1}}\}} = \frac{\partial \tan\delta\,(a, b, c, d, e, f)}{\partial c} \tag{114}$$

$$A_{\tan\delta,Im\{\mathbf{U_{ADC1}}\}} = \frac{\partial \tan\delta\,(a,b,c,d,e,f)}{\partial d} \tag{115}$$

$$A_{\tan\delta,Re\{\mathbf{U_{ADC2}}\}} = \frac{\partial \tan\delta\,(a,b,c,d,e,f)}{\partial e} \tag{116}$$

$$A_{\tan\delta,Im\{\mathbf{U_{ADC2}}\}} = \frac{\partial \tan\delta\,(a,b,c,d,e,f)}{\partial f} \tag{117}$$

$$A_{C_s,Re\{\mathbf{U_{ADC1}}\}} = \frac{\partial C_s\,(a,b,c,d,e,f)}{\partial c}, \tag{118}$$

$$A_{C_s,Im\{\mathbf{U_{ADC1}}\}} = \frac{\partial C_s\,(a,b,c,d,e,f)}{\partial d}, \tag{119}$$

$$A_{C_s,Re\{\mathbf{U_{ADC2}}\}} = \frac{\partial C_s\,(a,b,c,d,e,f)}{\partial e}, \tag{120}$$

$$A_{C_s,Im\{\mathbf{U_{ADC2}}\}} = \frac{\partial C_s\,(a,b,c,d,e,f)}{\partial f}. \tag{121}$$

The derivatives have been computed using mathematical software and can be expressed as

$$A_{\tan\delta,Re\{\mathbf{U_{ADC1}}\}} = \frac{d\,(a^2+b^2)\,(e^2+f^2)}{(-acf+ade+bce+bdf)^2}, \tag{122}$$

$$A_{\tan\delta,Im\{\mathbf{U_{ADC1}}\}} = -\frac{c\,(a^2+b^2)\,(e^2+f^2)}{(-acf+ade+bce+bdf)^2}, \tag{123}$$

$$A_{\tan\delta,Re\{\mathbf{U_{ADC2}}\}} = -\frac{f\,(a^2+b^2)\,(c^2+d^2)}{(-acf+ade+bce+bdf)^2}, \tag{124}$$

$$A_{\tan\delta,Im\{\mathbf{U_{ADC2}}\}} = \frac{e\,(a^2+b^2)\,(c^2+d^2)}{(-acf+ade+bce+bdf)^2}, \tag{125}$$

$$A_{C_s,Re\{\mathbf{U_{ADC1}}\}} = -\frac{(af-be)\,(e^2+f^2)}{\omega\,[a\,(cf-de)+b\,(-ce-df)]^2}, \tag{126}$$

$$A_{C_s,Im\{\mathbf{U_{ADC1}}\}} = -\frac{(ae-bf)\,(e^2+f^2)}{\omega\,[a\,(cf-de)+b\,(-ce-df)]^2}, \tag{127}$$

$$A_{C_s,Re\{\mathbf{U_{ADC2}}\}} = -\frac{(ad+bc)\,(-e^2-f^2)}{\omega\,(-acf+ade+bce+bdf)^2} - \frac{2e}{\omega\,(-acf+ade+bce+bdf)}, \tag{128}$$

$$A_{C_s,Im\{\mathbf{U_{ADC2}}\}} = -\frac{(bd-ac)\,(-e^2-f^2)}{\omega\,(-acf+ade+bce+bdf)^2} - \frac{2f}{\omega\,(-acf+ade+bce+bdf)}. \tag{129}$$

Then we need to explain how to determine the uncertainties of the real and imaginary parts of the measured voltages used in equations (111) and (112). The measured values by AD converter $\mathbf{U_{ADC1}}$ and $\mathbf{U_{ADC2}}$ are considered to be vectors. However, the AD converter can not measure vector values in principles. Instead, a series of samples

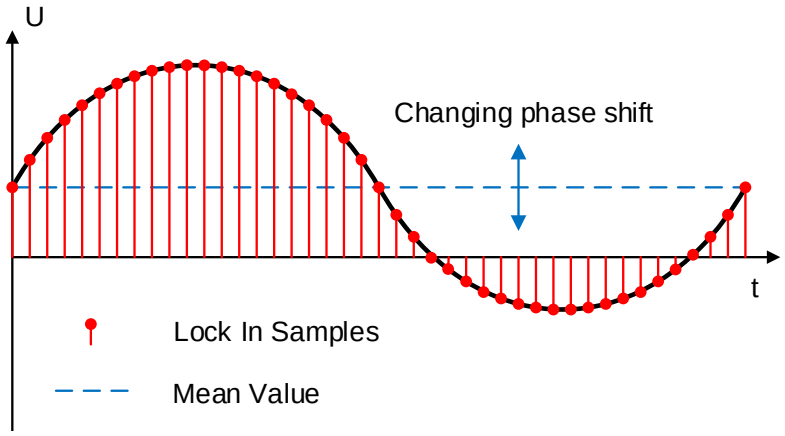

Figure 53. The output signal of the lock-in amplifier.

has to be acquired and the real and imaginary part of the complex number has to be computed separately. The computation is a job of the digital lock-in amplifier whose function has been described in Chapter (4.2) in detail. At a glance, the input data series is multiplicated by sine or cosine waveform. The mean value of the resulting product waveform carries the information about the real value or imaginary respectively. A typical output waveform of the lock-in amplifier is shown in Fig. 53. The mean value of the waveform is proportional to the real or imaginary value depending on which output of the amplifier is studied.

The next question is how to determine the standard uncertainty of measurement of real $u_{Re\{\mathbf{U_{ADCx}}\}}$ or imaginary $u_{Im\{\mathbf{U_{ADCx}}\}}$ part of the lock-in amplifier output. In this case x can be index 1 or index 2. The mean value of the real part waveform over one period can be expressed as

$$Re\left\{\mathbf{U_{ADCx}}\right\} = \frac{1}{N}\sum_{i=0}^{N-1} U_i, \tag{130}$$

where N is a number of samples and U_i are particular samples. Each sample can be expected in a form

$$U_i = U_{ADCx}[i] \cdot U_R\left[i\right], \tag{131}$$

where $U_{ADCx}[i]$ is an i-th sample of the ADC converter and $U_R\left[i\right]$ is the i-th sample of the lock-in reference signal.

If we want to analyze the standard uncertainty of this measurement we can proceed according to the equations (99) and (100). For illustration, we will derive standard uncertainty of the real part of AD converter one only. The remaining imaginary part and values for AD converter two can derive the same way. The uncertainty can be expressed as

$$u_{Re\{\mathbf{U_{ADCx}}\}} = \sqrt{\sum_{i=0}^{N-1} A^2_{Re\{\mathbf{U_{ADCx}}\},U_{ADCx[i]}} u^2_{U_i}}. \tag{132}$$

At first, we will derive the sensitivity factor $A_{Re\{\mathbf{U_{ADCx}}\}}$ with respect to the equa-

tion (100), then we can write

$$A_{Re\{\mathbf{U_{ADCx}}\},U_{ADCx[i]}} = \left.\frac{\partial Re\left\{\mathbf{U_{ADCx}}\right\}}{\partial U_{ADCx[i]}}\right|_{U_{ADCx[i]}} = \frac{U_R\left[i\right]}{N}. \tag{133}$$

Combining with the previous equation we get

$$u_{Re\{\mathbf{U_{ADC1}}\}} = \frac{u_{U_i}}{N}\sum_{i=0}^{N-1} U_R^2\left[i\right]. \tag{134}$$

The uncertainty of the i-th sample we can determine from half value of the AD converter quantization error as

$$u_{U_i} = \frac{U_{fs}}{2^M}\frac{1}{2\sqrt{3}}, \tag{135}$$

where U_{fs} is a full scale voltage of the AD converter and M is the number of bits of the AD converter. Then the total uncertainty of the real part measurement is

$$u_{Re\{\mathbf{U_{ADC1}}\}} = \frac{U_{fs}}{2^{M+1}N\sqrt{3}}\sum_{i=0}^{N-1} U_R^2\left[i\right], \tag{136}$$

which can be used for $u_{Im\{\mathbf{U_{ADC1}}\}}$, $u_{Re\{\mathbf{U_{ADC2}}\}}$ and $u_{Im\{\mathbf{U_{ADC2}}\}}$ as well. Combining these results with equations (111) and (112) we get the total uncertainty of capacitance and dissipation factor measurement.

6.2. Quantification of uncertainties

The equation stated in the section above has a few input values. The results depend mainly on the value of excitation of AD converters, number of samples gathered by Lock-in amplifier, number of bits of AD converters, and so on. The operator of the instrument or proposed instrument platform would want to know what is the uncertainty of measurement when a particular value of capacitance or dissipation factor at a given frequency is measured. Therefore, the equation stated above has to be evaluated over a range of different capacitances and also a range of excitation frequencies. Then we can get a 2D plot of uncertainties for a particular measurement value over frequency expressed in percents.

Due to the complexity of these equations, a MATLAB script has been written. The script evaluates all equations stated above and plots the 2D graph documenting a percent value of uncertainty for specific measured value and frequency. The function of the script can be summed up in a few steps:

- Read input parameters (ENOB, Lock-In lookup table width, ...).
- Generating reference sine and cosine wave for Lock-In amplifier.
- Input signal generation based on normal capacitance and measured capacitance value.
- Compute Lock-In output signal for a set of input frequencies.
- Evaluate uncertainties equations.
- Plot results.

The estimation of the total uncertainties resulting from the script described above is stated in Fig. 54 and Fig. 55. The conditions for capacitance uncertainty estimation are stated in the plot legend. It is assumed a similar value of dissipation factor of measured

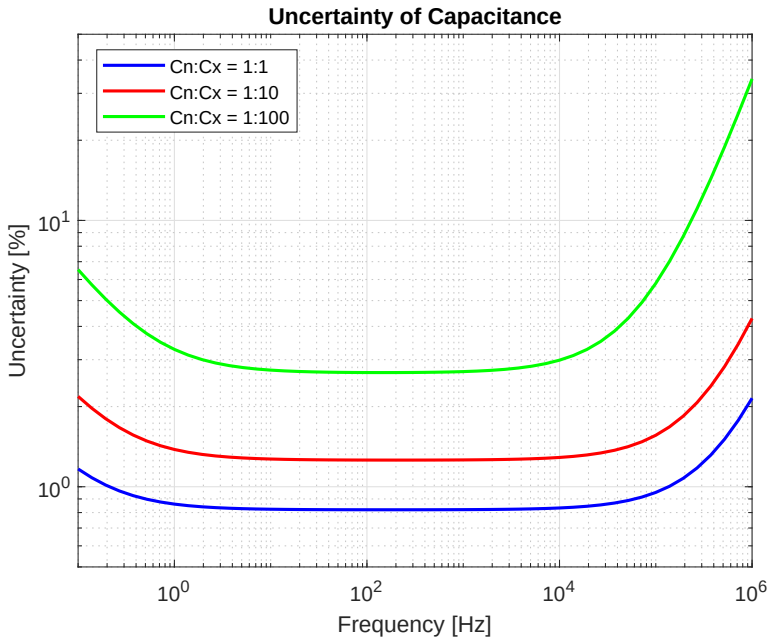

Figure 54. Quantification of capacitance uncertainty

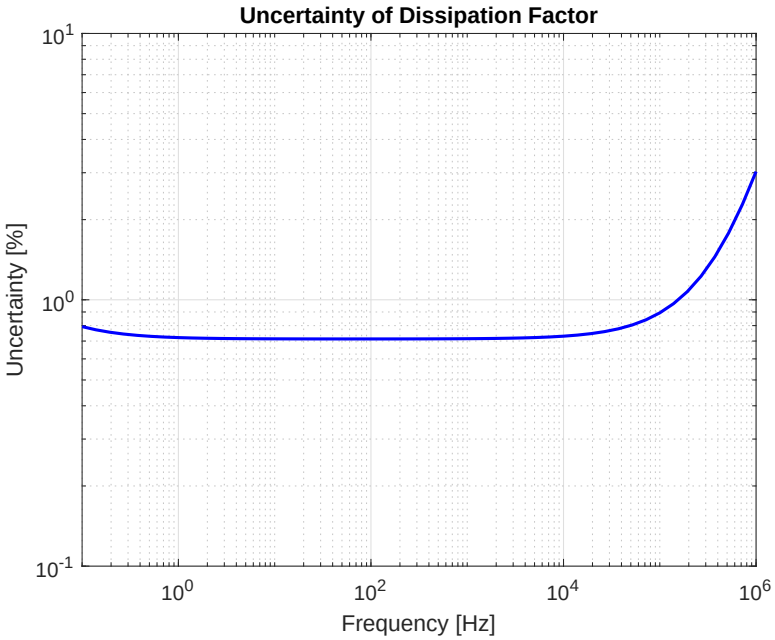

Figure 55. Quantification of dissipation factor uncertainty

and reference impedance has been considered in case of dissipation factor uncertainty estimation.

6.3. Summary

This chapter deals with the measurement uncertainty of the proposed platform. A special emphasis has been focused on the LIA implementation and its effect on the total uncertainty of data measured by the platform. The equation describing the total uncertainty has been derived. It corresponds to the thesis Aim No. 4a. The equations considered AD converter ENOB, several samples per one period, and uncertainty of one sample determination. The uncertainty of the normal capacitance and sensing resistors has been neglected. The particular computation and quantification (which corresponds to the thesis Aim No. 4b) of the total measurement uncertainty has been executed by the MATLAB tool due to the high complexity of the equations. The results revealed the proposed platform can be suitable for the DSP method with better parameters than market available instruments.

7. Verification Experiments

Few experiments were made to verify the designed board. First experiments have been executed in laboratory conditions to verify basic properties of the platform, such as long-term stability of the input circuits, the function of LIA, and cooperation with the PC control application. Then, the scientific team traveled to a remote location where experiments on real objects could be made.

7.1. Laboratory Experiments

The first experiment was focused on a long term stability of used ADC, the second experiment was focused on the sensitivity of a phase shift measurement and the third experiment was focused on the accuracy of the phase shift measurement. The block diagram of the first experiment focused on measurement stability is shown in Fig. 56. In this case, an arbitrary waveform generator 33522A manufactured by Agilent company has been used as a source of the excitation signals. Each of the ADC inputs of the platform has been excited by one of the generator's channels. A sine waveform has been chosen with amplitude $250mV$, frequency of 50 Hz and phase shift of 0 degrees against each channel has been set.

Then LIA raw output data has been captured for two hours. The captured data is shown in Fig. 57. The Figure shows the ADC input 1 data. The blue line represents the real part output of the LIA and the red line represents the imaginary part output of the LIA. During the two hours test, no drift was observed. The root mean square error was evaluated as $1.5\,\mu V_{RMS}$.

The second experiment was designed to prove the phase shift sensitivity close to $0.001\,deg$ that leads to the tangent delta of 1.75×10^{-5}. The tested signal was generated using the arbitrary waveform generator Agilent 33522A. However, the resolution of the phase shift between the two channels can be set in the step of $0.1deg$ in sine mode, the user can use arbitrary mode to get the finest resolution. The arbitrary mode allows loading the internal memory of the instrument with a user-defined set of signal samples.

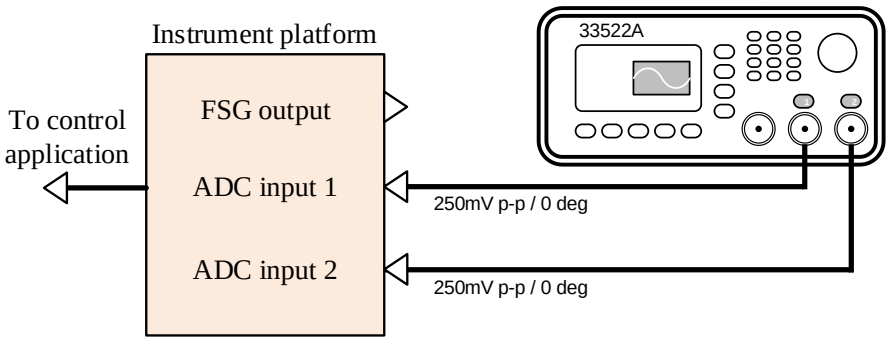

Figure 56. The block diagram of the stability experiment

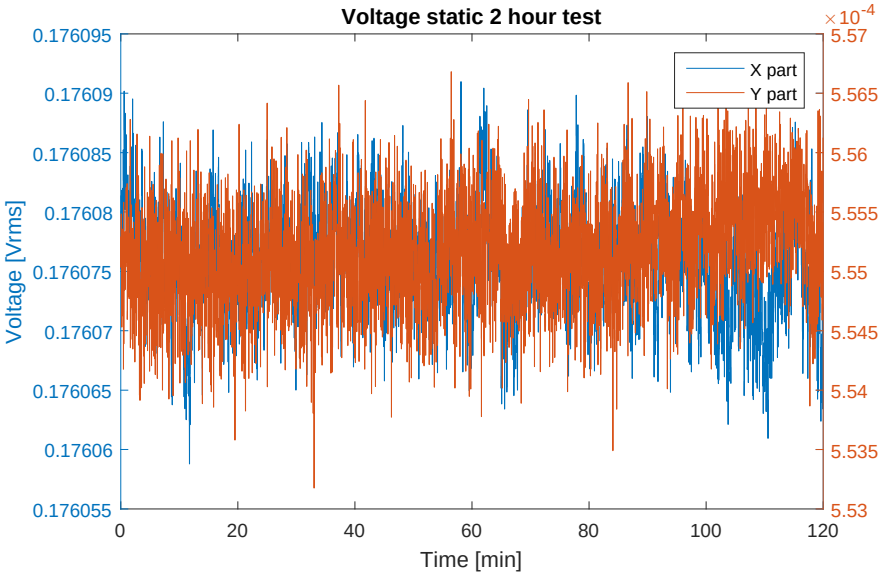

Figure 57. The measured data captured during the two hours test

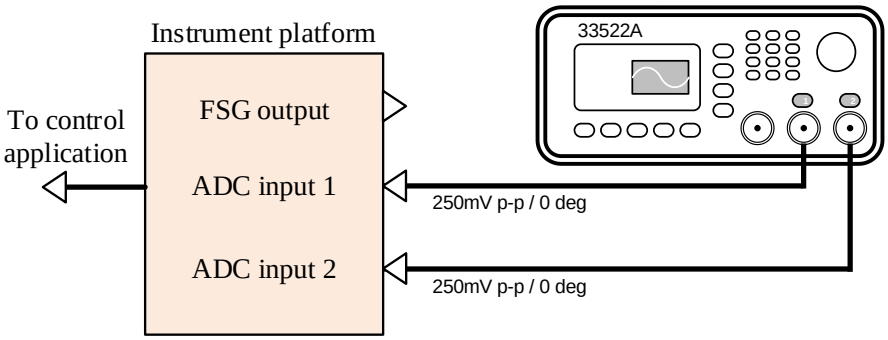

Figure 58. The block diagram of the phase shift sensitivity

The memory is 1×10^6 samples wide and each channel has separate one. It allows to prepare two sine signals with a phase shift of one sample and download them to each channel memory. Shifting the signal of one samples creates phase shift of $3.6 \times 10^{-5}\,deg$. If the phase shift is set to three samples we get $0.00108\,deg$.

The Fig. 58 shows the schematic of the phase shift sensitivity experiment. The same waveform generator has been used as in the previous case, but this time the arbitrary mode has been activated. The phase of three samples and frequency of $50\,Hz$ has been used. Fig. 59 shows raw data captured from the imaginary part output of the LIA. The blue line shows data captured by ADC input 1 and the red line shows data captured by ADC channel 2. Since data of the two channels do not overlap and even there is a voltage margin between them we can say the proposed platform can detect at least the phase shift changes of $0.00108\,deg$.

The third experiment was aimed to prove the accuracy of the measurement of the phase shift. A block diagram of the experiment is shown in Fig. 60. The front-end was excited by sin waveform with a frequency of 50 Hz and the internal phase shifter was set for different angles. Measured results are stated in Table 7, where U_{IN} is an

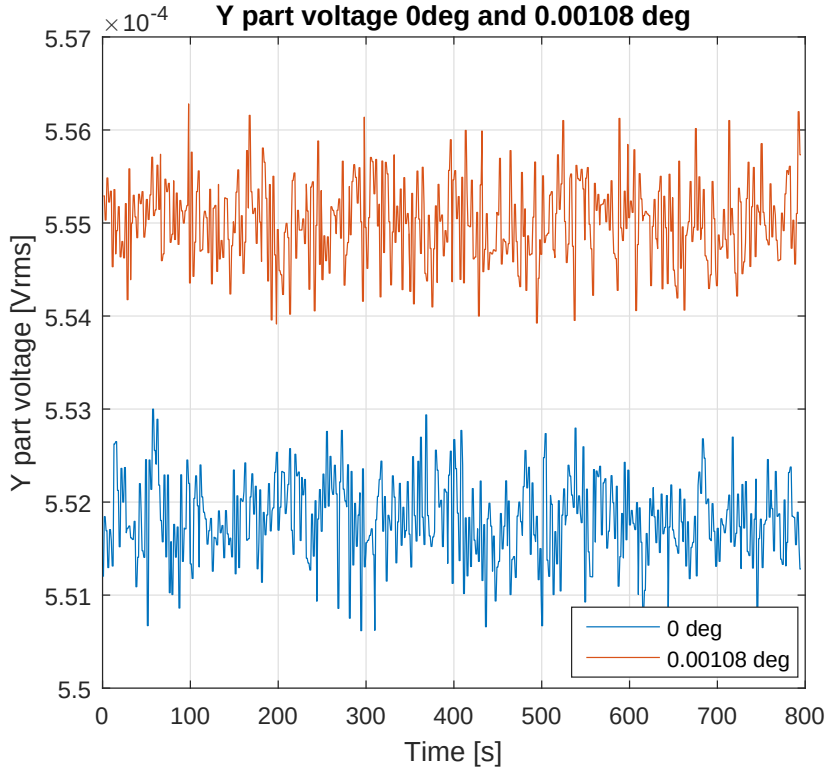

Figure 59. The measured data captured during phase shift sensitivity experiment

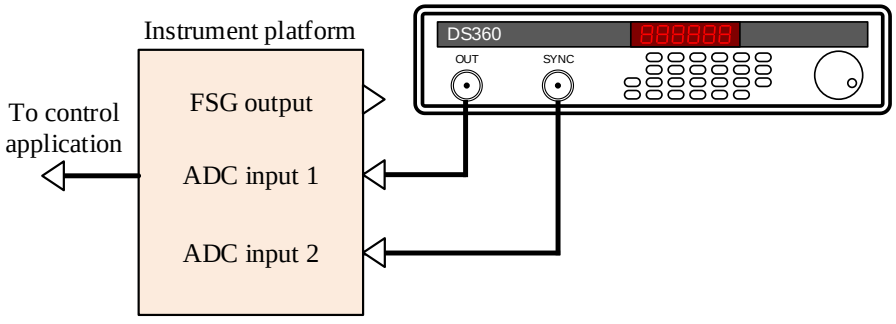

Figure 60. The measurement of phase shift accuracy

Table 7. The results of the angle measurement accuracy

$U_{IN}[V]$	$\varphi[rad]$	$\theta[rad]$	$\epsilon[rad]$
0.17966	0π	-2.55×10^{-5}	2.55×10^{-5}
0.17966	$^1/_8\pi$	0.39267	2.91×10^{-5}
0.17966	$^1/_4\pi$	0.78537	2.82×10^{-5}
0.17966	$^3/_8\pi$	1.17807	2.72×10^{-5}
0.17966	$^1/_2\pi$	1.57077	2.63×10^{-5}
0.35934	0π	1.6×10^{-5}	1.60×10^{-5}
0.35934	$^1/_8\pi$	0.39272	2.09×10^{-5}
0.35934	$^1/_4\pi$	0.78540	1.84×10^{-5}
0.35934	$^3/_8\pi$	1.17811	1.28×10^{-5}
0.35934	$^1/_2\pi$	1.57078	1.63×10^{-5}

RMS value of input voltage, ϕ is a phase shift set into the internal PLL phase shifter, θ is phase computed from output values of the implemented LIA algorithm and ϵ is an absolute error concerning the set internal phase shift.

However, the previous experiment was used to prove the basic functions of the platform, the next experiment has been designed to verify the instrument in case very similar to real usage. It includes measurement on real HV objects, for instance, transformer. Unfortunately, our scientific team had only limited access to such devices, which included one visit to a company specialized in restoring and repairing HV transformers. Therefore, the platform had to be verified in conditions as much similar as it could be possible to simulate in laboratory conditions.

A test circuit sample representing a typical impedance of the transformer has been built. An electric schematic of the circuit is shown in Fig. 61. The circuit had been physically made of real passive components. The particular values of the passive components have been chosen randomly to create a shape of electrical impedance dependent on frequency as close to the real transformer as possible. The impedance curve of the circuits is shown in Fig. 63. The circuit was used to determine platform measurement precision over a wide frequency range from 1 Hz up to 10 kHz. A professional impedance analyzer MFIA manufactured by Zurich Instruments company has been used to determine real impedance dependent on frequency. Fig. 62 shows a diagram describing the accuracy of the MFIA instrument. It can be found the accuracy of the MFIA is better than the intended accuracy of the proposed platform, therefore the measured dependency can be used to verify the accuracy of the proposed platform.

The capacitance and the dissipation factor measurement error has been analyzed according to the following formula

$$\delta_X = \frac{X_{meas} - X_{ref}}{X_{ref}} \cdot 100\%, \tag{137}$$

where X is the quantity analyzed (capacitance or dissipation factor), δ_X is measurement error of the quantity X, X_{meas} is value measured by the proposed platform and X_{ref} is value measured by the MFIA instrument. The plots of the determined measurement errors are shown in Fig. 64 and Fig. 65 respectively.

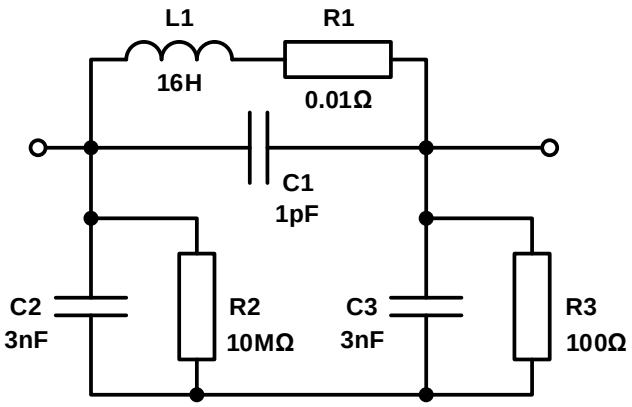

Figure 61. The electric schematic of the simulated DUT impedance

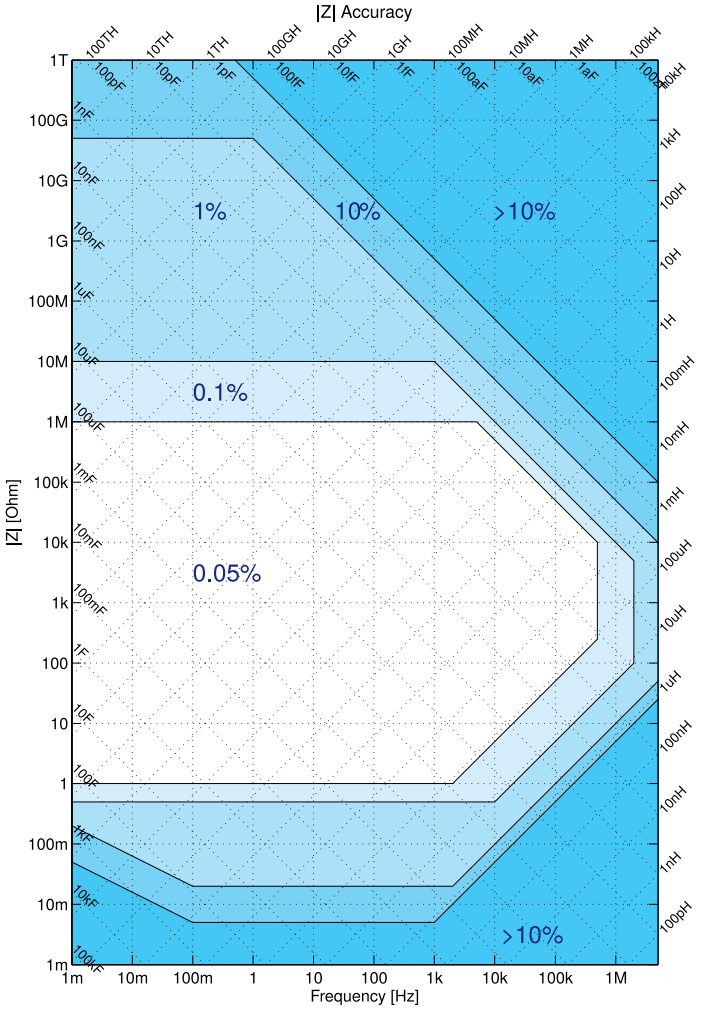

Figure 62. Reactance accuracy of Zurich Instruments MFIA instrument

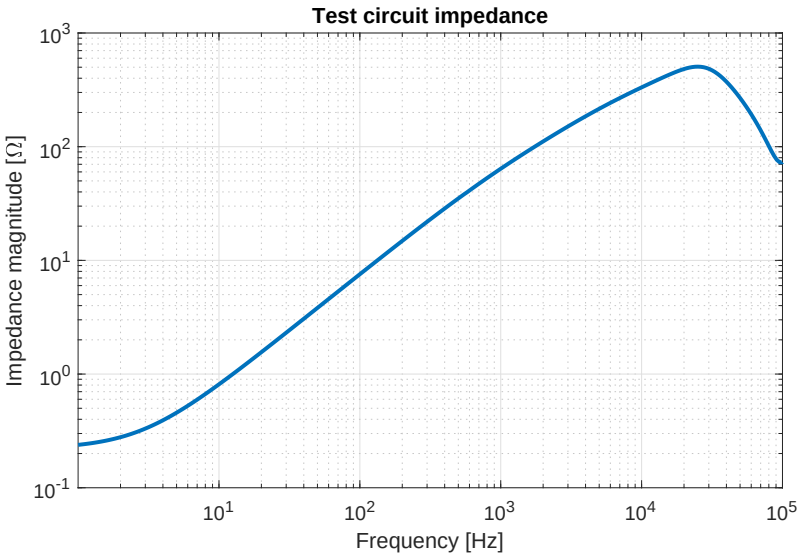

Figure 63. The test circuit impedance measured by MFIA instrument

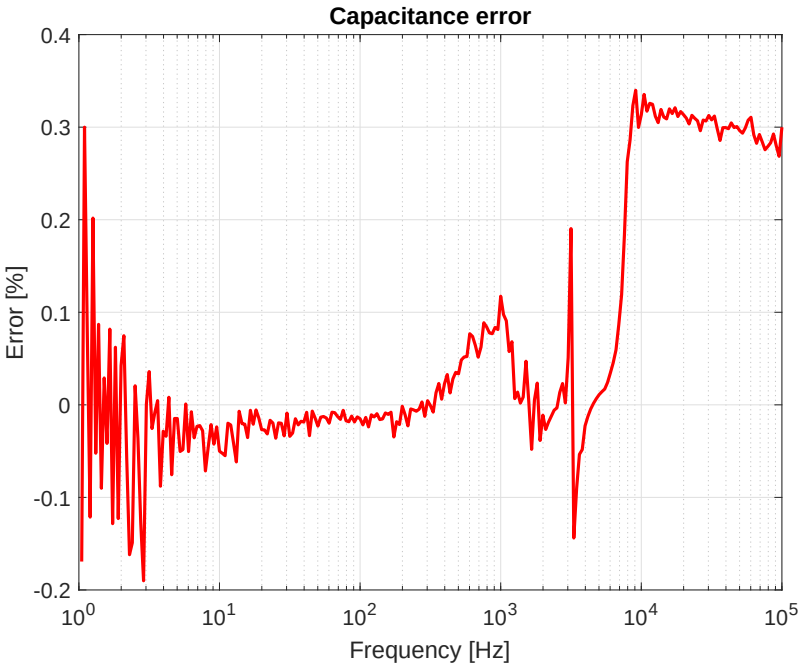

Figure 64. Relative error of capacitance measurement

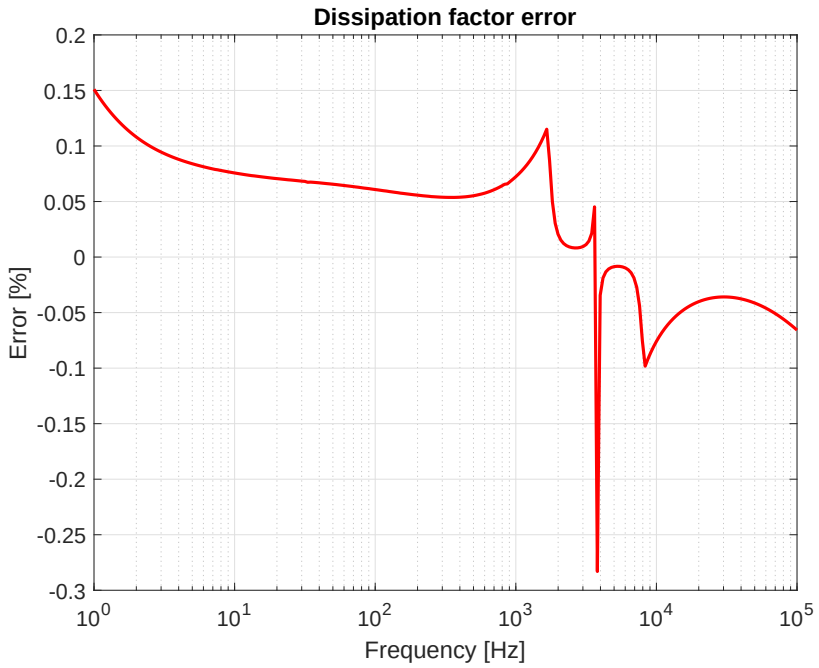

Figure 65. Relative error of dissipation factor measurement

7.2. Field experiments

To verify the designed platform in an industry environment several field experiments have been performed. As devices under test real high voltage transformers lent by OMZ Hranice were used, s. r. o. company. The company is dealing with revision and repairing high voltage transformers for electric power supply grids and railways vehicles. The company is a partner of the ORGREZ laboratory, which is contributing to working on the scientific grant this work is part of.

The company provided two test objects (HV transformers). The first object, marked as Object A, was damaged. The second object, marked as Object B, was the similar type as Object A, but it was after repair by the OMZ company. A photograph of both of the objects is shown in Fig. 66.

A schematic of the internal connection of the objects is shown in Fig. 67. The winding terminals of the transformers are marked by letters A, B, and C. The upper case letters are used to mark the high voltage side and lower case letters are used to mark the low voltage side. A ground terminal, connected with the transformer enclosure is marked by the letter g. The set of technical parameters of the tested objects is stated in Table 8.

The schematic of the experiment and the proposed measuring platform is shown in Fig. 68. The output of the measuring platform is connected to an HV amplifier TOE 7610-10. The amplifier is capable to drive 4 A of output current at 40 V. The frequency range of the amplifier is from DC to 100 kHz [44]. The amplifier drives the normal capacitance C_n as well as measured capacitances C_{Cg} or C_{cg}. Similarly, another capacitance can be measured, given by another combination of connected transformer terminals, for example, C_{Bg} is the capacitance between terminal B and ground terminal g. The driven capacitances are connected to the measuring platform, where required electrical quantities are evaluated.

Figure 66. The photograph of the tested transformers. The Object A is in the foreground of the picture.

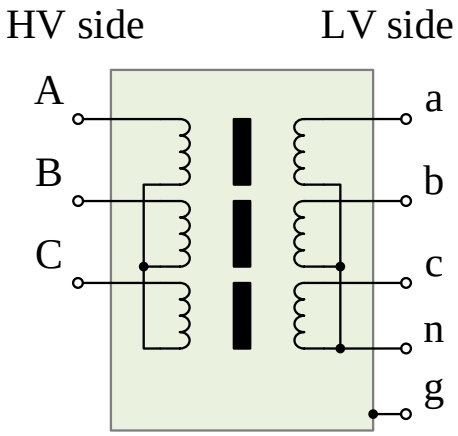

Figure 67. The schematic of the tested transformer.

Table 8. Comparison of technical parameters of the test object A and B

Parameter	Object A	Object B
Type	TOH 294/22	TO 294/22
Serial Number	312067	244398
Phase Nr.	3	3
Frequency	50 Hz	50 Hz
Input voltage	22 kV	22 kV
Output voltage	420 / 242 V	400 / 231 V
Input current	2.62 A	2.62 A
Output current	137.5 A	144.4 A
Input power	100 kV.A	100 kV.A
Output power	100 kV.A	100 kV.A
Total mass	850 kg	780 kg
Manufacturer	BEZ Bratislava	BEZ Bratislava
Year of manufacture	1995	1985

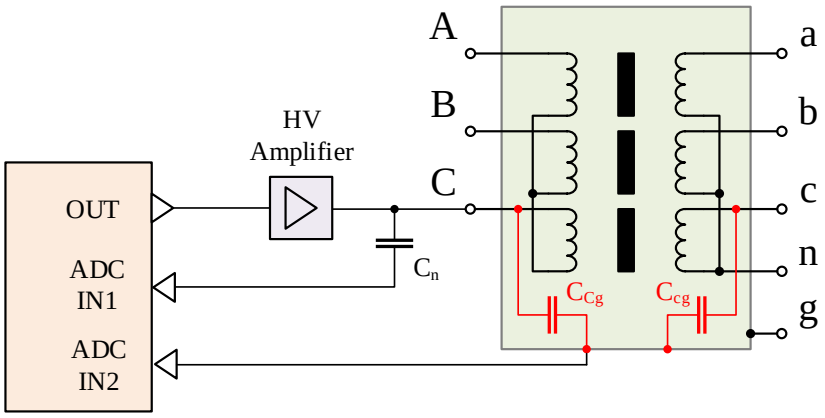

Figure 68. The schematic of the field experiment connection.

To show the designed measuring platform is capable to measure required transformer parameters in the real measurement, several measurements have been performed. The complete list of the measurements performed on the test objects is stated in Table 9. The table documents the measured parameter and a reference to a figure showing a particular graph of the measured values.

Figure 69. The photograph of the measuring instrument connected to the tested Object A.

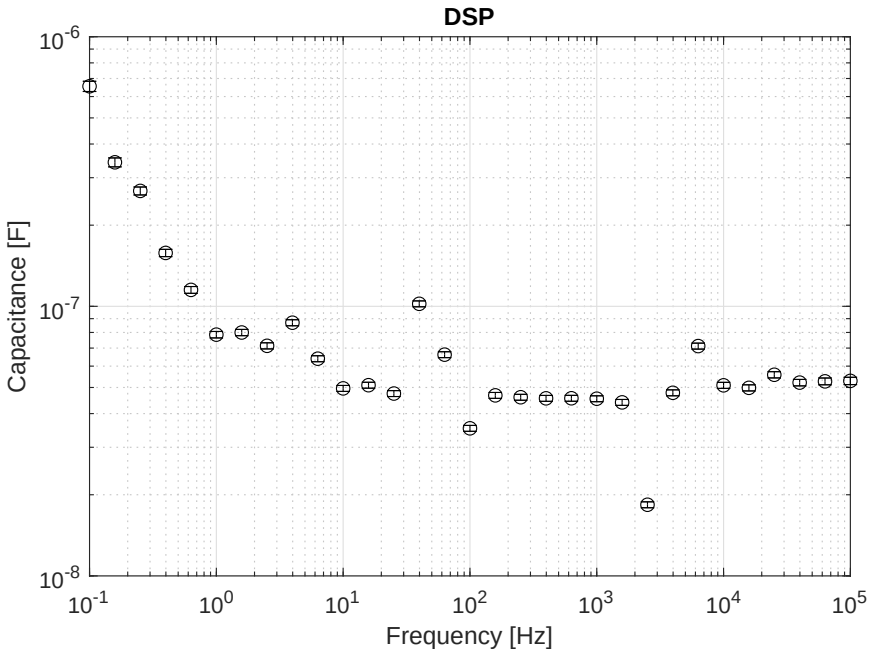

Figure 70. Capacitance course of test Object A between terminal C and g.

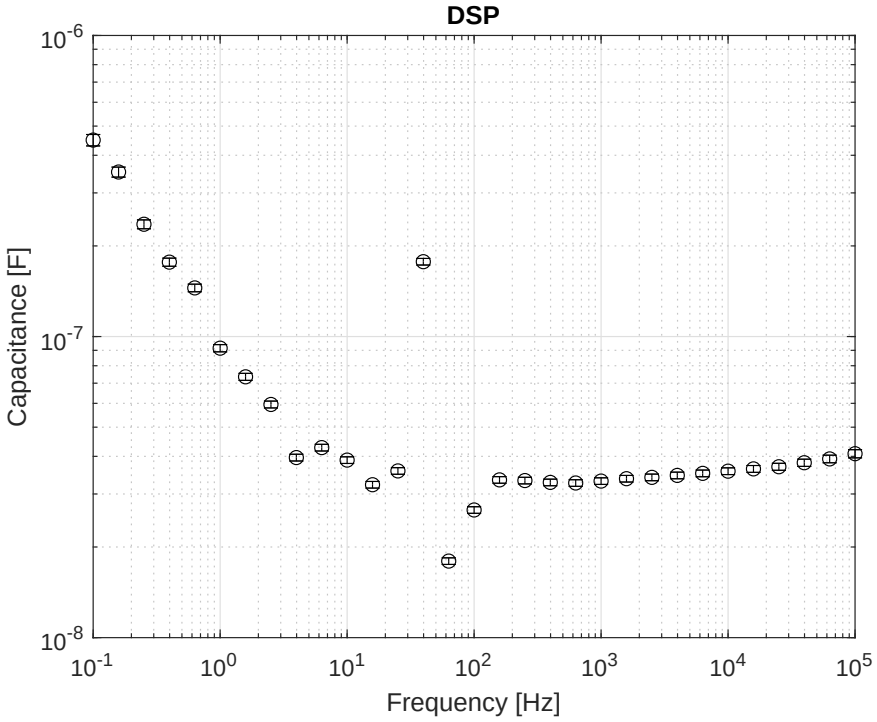

Figure 71. Capacitance course of test Object A between high and low voltage sides.

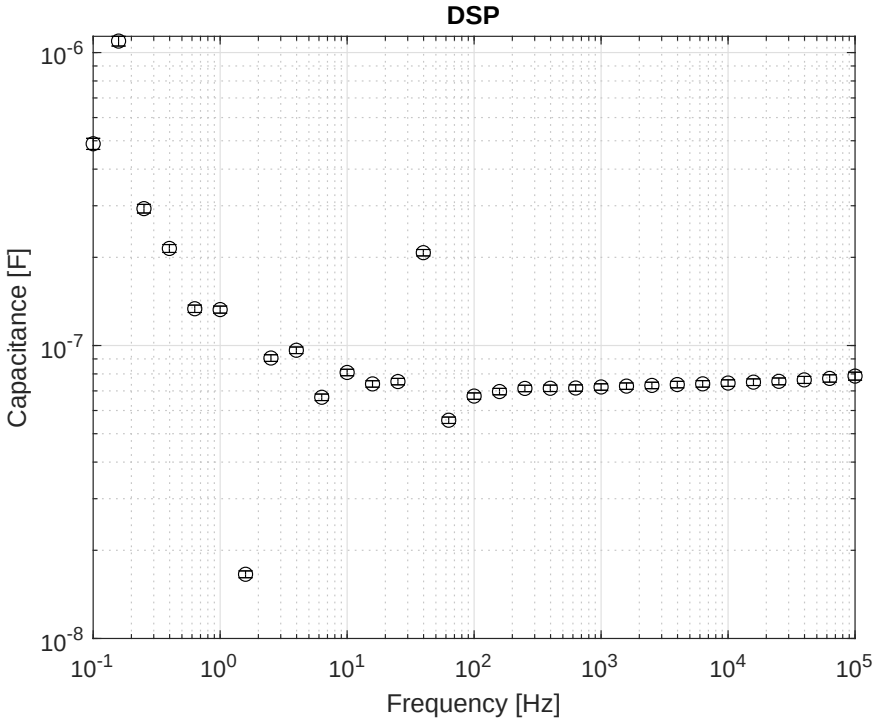

Figure 72. Capacitance course of test Object A between terminal c and g.

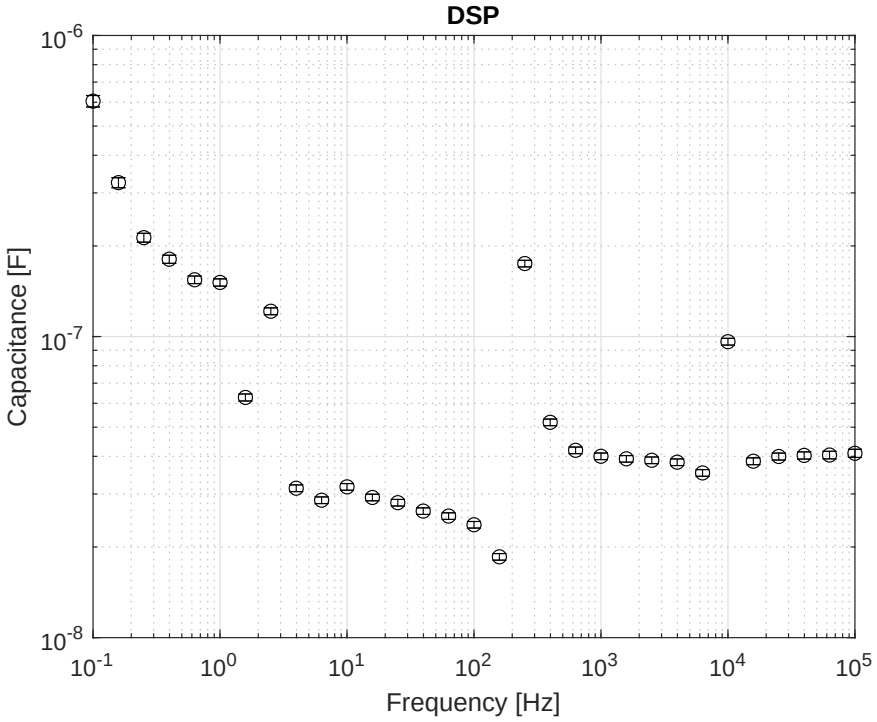

Figure 73. Capacitance course of test Object B between terminal B and g.

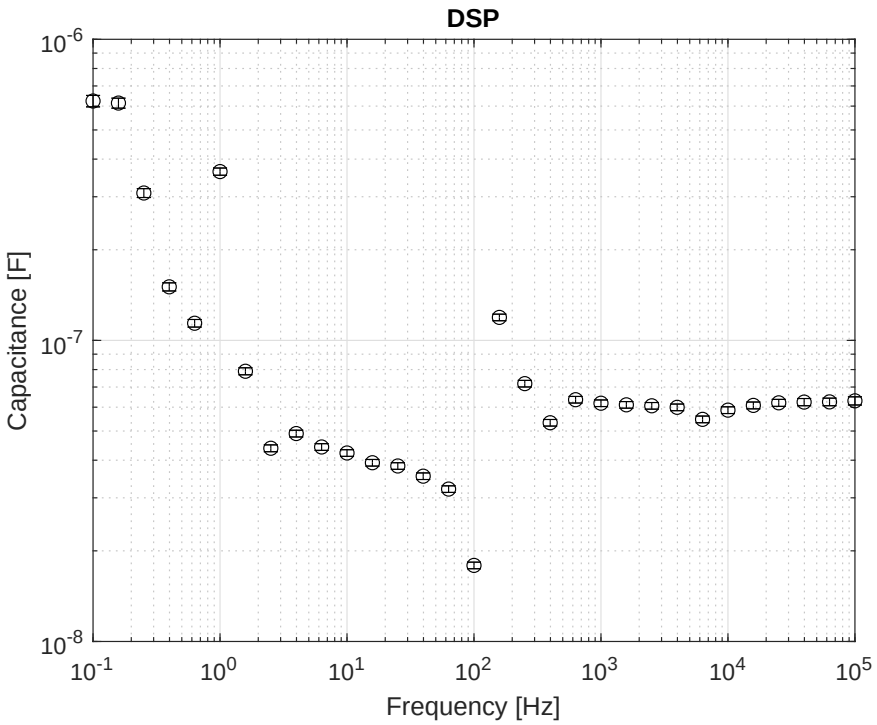

Figure 74. Capacitance course of test Object B between high and low voltage sides.

Table 9. List of the measurement performed.

Parameter	Results
Object A	
C_{Cg}	Fig. 70
C_{HV-LV}	Fig. 71
C_{cg}	Fig. 72
Object B	
C_{Bg}	Fig. 73
C_{HV-LV}	Fig. 74
C_{ag}	Fig. 75

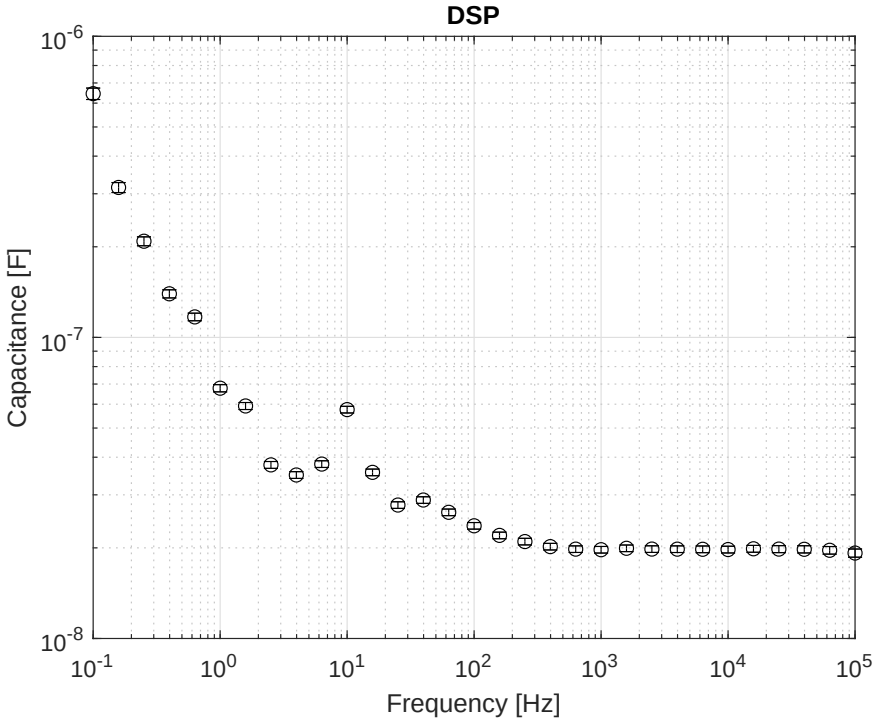

Figure 75. Capacitance course of test Object B between terminal a and g.

7.3. Data Evaluation

Various types of insulation defects such as water content, insulation geometry change, change in conductivity can be recognized from the shape of the dissipation factor plot over the excitation frequency. An example of these effects on the curve shape has been stated in Fig. 21. If a change in particular part of the curve was detected compared with the previous measurement it can be said there is a high risk of the defect occurrence. The key thing is comparing the current results with the previous one and watching the shape development over a relatively long period. Therefore it is necessary to repeat the measurement period and maintain a database of the measurement results for all watched objects.

To make the comparison more effective and automatic two methods of evaluation can be proposed. The first method counts with an area underneath the measured curve, see Fig. 76. The blue cross symbols represent the coupling frequency and dissipation factor as the output of the FDS instrument. Linear interpolation between adjacent measuring points is considered.

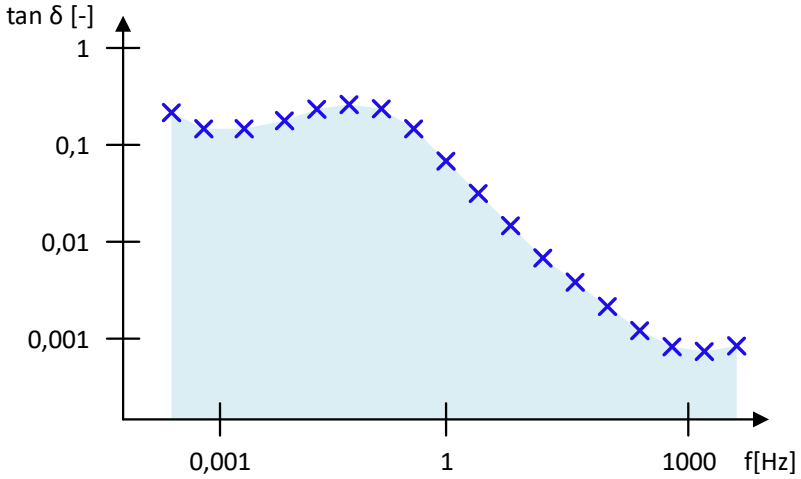

Figure 76. Area evaluation of the FDS curve

Let f_1 up to f_N to be particular excitation frequencies of the FDS measurement and $\tan\delta_1$ uo to $\tan\delta_N$ are dissipation factor values at f_i, the studied area of the curve can be expressed as

$$A_{tg\delta} = \sum_{i=1}^{N-1} \left[(f_{i+1} - f_i) \left(\tan\delta_i + \frac{\tan\delta_{i+1} - \tan\delta_i}{2} \right) \right]. \tag{138}$$

The result of the equation is an in units of $Hertz$. The evaluated area can be stored in the database along with the measured curve. If a significant change is detected compared with the value evaluated according to the previous measurement, it will indicate that special attention to the current curve is needed. The decision on how to adjust a threshold when the change of the area should draw the attention of the object operator would be a subject of a special investigation. It would need a period of testing and evaluating of the same set of real objects over a few years to get a relevant data set to derive a rule on how to adjust the threshold. Unfortunately, our scientific team has no access to such a set of the object for the time being.

The second evaluation method employs the determination of the correlation coefficient between current and previous measurements. The equation of the correlation coefficient can be expressed as

$$\rho_{X,Y} = \frac{cov\,(X,Y)}{\sigma_X \sigma_Y} = \frac{E\,(XY) - E\,(X)\,E\,(Y)}{\sqrt{E\,(X^2) - E\,(X)^2} \cdot \sqrt{E\,(Y^2)\,E\,(Y)^2}}, \tag{139}$$

where X, Y are compared data sets, where each value of the data set consists of a pair of excitation frequency ad measured dissipation factor, $cov\,(X,Y)$ is covariance function, σ_X and σ_Y are corresponding standard deviations and $E\,(Y)$ is expected value operator. The output value of the equation is a number in interval from -1 up to 1, where the lowest value indicates a perfect negative correlation and the highest value perfect positive correlation. A zero value indicates no correlation at all.

The method lies in the comparison of the current and previous measurement data sets using correlation coefficients. If the resulting coefficient value is close to one, it can be said, the compared data set are correlated and there is a high probability no change in the machine occurred from the last measurement. If the coefficient is below a certain threshold it could indicate a change in the characteristic of the tested object and a detailed inspection of the data set is necessary to estimate a type of failure. Again, the exact determination of the threshold could be a subject of further investigation and research.

A problem may occur if the two compared data were not performed at the same excitation frequencies. Then, the correlation method will show irrelevant values. Fig. 77 shows an example of such situation. Data set X and data Y have been performed at different excitation frequencies. Therefore, the data set need to be enriched with another sample to line up data before the correlation coefficient can be evaluated.

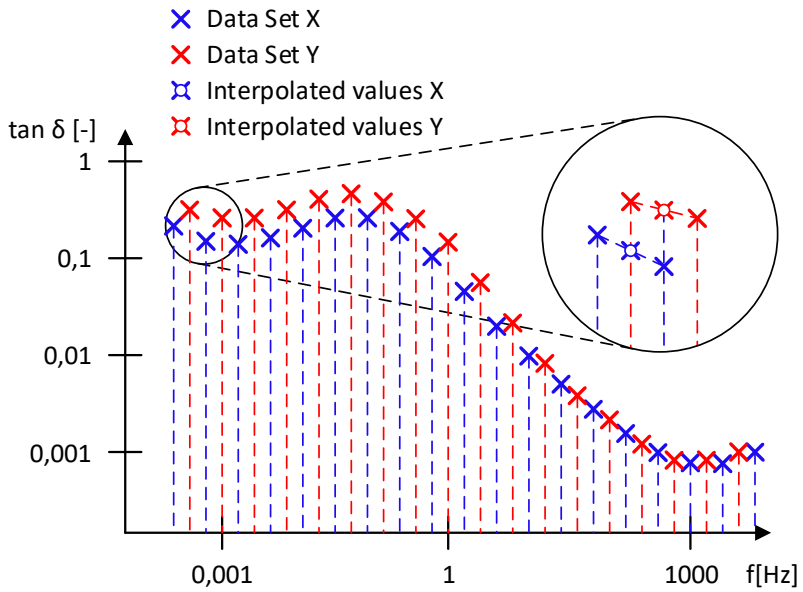

Figure 77. Interpolation of missing samples for correlation method

7.4. Summary

The proposed platform has been verified in two steps. At first, few laboratory experiments has been executed. The laboratory experiments have been focused to prove instrument measurement stability, input signal phase shift sensitivity, and phase shift accuracy. Then a passive circuit specimen with frequency-dependent impedance has been constructed. The topology and particular values of the passive components have been chosen to create an impedance characteristic close to a real HV transformer. The real impedance of the specimen has been determined using an MFIA impedance analyzer as a reference instrument. Then data measured by the proposed platform has been compared with data that came from the reference instrument. The experiment revealed the capacitance error did not exceeded 0.4 % and dissipation factor error did not exceed 0.3 %. The experiment also served as an opportunity for a full test of instruments simulating real conditions. These experiments also fulfill the thesis Aim No. 5a.

The scientific team had only limited access to real HV objects. However, it could be managed to negotiate a visit to OMZ Hranice, a. s. company. The company provided a one-day lend of the transformers with the different years of manufacture, but with similar parameters. One transformer was failed and the second was after a repair executed by the company. The proposed instrument platform has been used to make a DSP measurement on both transformers, which is related to the thesis Aim No. 5b. Unfortunately, the scientific team did not have access to the market available instruments described in section 2.2. Therefore a comparison measurement has not been executed.

At the end of chapter two method of data evaluation has been proposed (which corresponds to Aim No. 6). The first method utilizes area computation underneath FDS values and the second one correlation between current and previous FDS measurement. The methods help to compare the differences between two FDS data sets. If the output value of the method reaches a threshold it will indicate a possibility of tested object failure occurrence.

8. Conclusions

Since every unexpected system failure may result in huge financial losses, the operators of all kinds of the technical system want to know, predict and avoid any upcoming failures of the system. Therefore, the role of non-invasive diagnostics in all technical fields is very significant. Especially, in the field of energetics, there are many expensive technical devices with an expected lifetime in order of tens of years. Even if the lifetime is expected by their manufacturer, periodic inspections are necessary. The inspection should reveal a risk of upcoming failure and the system operator can take an action to prevent additional losses. To be able to inspect the system proper diagnostics methods have to be developed. The methods usually describe how to interpret the measured physical value on the tested device. For instance, if one of the measured values is out of the normal range, it may indicate some changes in the tested device. On the other hand, to provide a precise measurement sophisticated measuring instrumentation is needed.

This work deals with a non-invasive diagnostic of high voltage machines. The special emphasis is focused on a machine's insulation state assessment. Since the machine insulation is usually formed by a dielectric material (liquid or solid) a brief dielectric theory has been stated in Chapter 1.1. The basic definitions such as polarization, dielectric relaxation, and absorption are mentioned. The next two chapters deals with the commonly used methods and techniques, that are capable to indicate an impending machine failure. Special emphasis is given to dielectric spectroscopy and its purpose in the field of HV machine diagnostics. The base physical phenomenons are described and commonly used terminology is mentioned. Two different approaches to DSP are described. Also, DSP measuring instruments available on the market are compared.

8.1. Goals Evaluation

The main goal of this thesis was to develop a measuring platform intended for the DSP method for HV machines with better measuring precision and stability than the market instrumentation offers. The complete list of goals and other details are stated in Chapter 3. To summarize the results, refer to the listings below. Each of the goals mentioned in Chapter 3 is commented separately.

1. To make an overview of the DSP method and market research of existed instrumentations.

A derivation of the DSP method is stated in the Chapter 2.1. The derivation is based on a dielectric theory that is briefly stated in Chapter 1.1. An overview of the market available instruments is stated in Chapter 2.2.

2. To design the hardware platform of the instrumentation.

This is the main goal of this thesis. A big effort has been encountered to develop a hardware platform intended for DSP with parameters improving the existing market available instruments. The goal consists of four sub-goals.

2a) To delegate the work amount among the research team.

Due to the high complexity of the platform development, it was decided to split the workload into two members of the research team. Splitting the work it was intended to design a platform suitable for DSP and the FRA method which is a topic of the doctoral thesis of the second team member. The details about the workload division are stated in Chapter 3.

2b) To identify the key parameters and possibilities of improvement.

As the key parameter to improve, the precision of dissipation factor measurement has been identified. The identification has been based on the author's experience with the design and development of Capacitance and dissipation factor meters for HV machines. The design and results have been published in the author's master thesis [45] and conference article [46].

2c) To design the electric schematic of the daughter board.

Based on the workload division, the author's task has been to develop the daughter board which provides an analog-to-digital and digital-to-analog conversion part of the proposed platform. The schematic design utilizes modern electrical components to achieve the best possible results. The complete description of the schematic is stated in Chapter 4.1.

2d) To design a printed circuit board of the daughter board.

Besides a proper electric component choice, it was necessary to follow special PCB techniques to achieve to ensure the board will be as noise-free as it is possible. The PCB design is mentioned in Chapter 4.1.6.

2e) To create FPGA VHDL design collecting the data from ADCs.

A VHDL design including reading the ADC data and implementing LIA has been created. The LIA is a key part of the platform decomposing the input signal into the real and imaginary parts.

3. To design the control application.

Today trends in modern instrumentation show that instrumentation manufacturers provide a control PC application to control the device and to read out the measured values. In contrast to the old-style instrumentation where the front panel was full of various types of pushbuttons, knobs, switches, and LEDs, this is a much more effective way how to control the device. Therefore, it was decided, the second goal of the thesis is to develop the control application. The goal consists of four sub-goals.

3a) To ensure a cross-platform functionality.

To cover as many potential users as possible, it was decided to keep the control application as a cross-platform. It means, the application can be easily built under various mostly used platforms (Windows, Linux, macOS, Android). Therefore a Qt framework has been chosen to create the control application. Further details about this topic can be found in Chapter 5.2.1.

3b) To implement the computations necessary for DSP and FRA methods.

To keep the hardware platform as universal as possible, the instrument platform is sending only vector voltmeter data to the computer. The data corresponds to the measured voltage vector. Then the necessary quantities computation for each method can be performed on the computer. For DSP it is the capacitance and dissipation factor and in the case of FRA, it is the magnitude of the electrical impedance. Therefore the software inside the FPGA can stay simple the platform is universal for both methods. For detail description refer to Chapter 5.2.2.

3c) To design a graphic user interface to display the results of the measurements.

As it was mentioned in the text above, except for the quantities computation the control application should provide a proper measurement readout. For the measured data display, a plot diagram has been chosen. The user can set how much measurement point will be executed and the frequency range of the measurement. The application then issues commands to perform the points progressively. As the result of the measured point arrive from the instrument, the application plots the results and issue another measured point command. Detailed information about this topic is stated in Chapter 5.2.3.

3d) To design a communication protocol for the platform.

It was stated in the previous text that hardware platforms send data to the control application. Therefore there should be a communication link between the platform and the computer. The platform is equipped with both USB and Ethernet physical communication interfaces. A certain effort has been developed to choose a proper communication protocol for both USB and Ethernet links. Finally, it was decided to create a proprietary protocol enabling all necessary functions. The design protocol can be used under USB and Ethernet links as well. The description is stated in Chapter 5.1.

4. To examine the measurement uncertainties.

Examination of measurement uncertainties revealed possible sources of measurement inaccuracies. It helped to improved the signal processing algorithm to mitigate the influence of the sources.

4a) To derive equations leading to uncertainties evaluation.

The basic equations describing the sources of inaccuracy have been derived. A sum-up of these results is stated in Chapter 6.

4b) To perform computations to quantify measurement uncertainties.

Due to the high complexity of uncertainty equations, a MATLAB script has been written for particular quantification of the measurement uncertainties. The results stated in Chapter 6.2 revealed the proposed instrument platform can show better accuracy performance than market instruments.

5. To verify the platform functionality.

To be sure that the proposed platform is designed with intended parameters and still suitable for field measurement on real devices under test a proper verification is needed. In this case, a verification consisting of two stages has been chosen. Each stage forms one of the following sub-goals.

5a) To perform a laboratory tests.

To verify the functionality of the front-end a basic lock-in amplifier implementation was designed. It was observed, that the front-end provides time stable results and the instrument can use in the measurement of the dissipation factor with a resolution of $1.75 \cdot 10^{-5}$ at a frequency of 50 Hz. It was also proved the accuracy of $3 \cdot 10^{-5}\,rad$ in measured angle although without any sophisticated calibration. The results have been also presented in conference paper [47] and journal article [48]. A test with a simulated DUT impedance has been performed. The measured values have been compared with results based on a professional impedance analyzer. The test revealed the relative error of capacitance measurement was not higher than 0.4% and the relative error of dissipation factor was not higher than 0.3%. These results have been published in a conference paper [49]. The detailed information about tests themselves and test conditions are stated in Chapter 7.1.

5b) To perform a field tests with real tested objects.

Chapter 7.2 describes field tests that have been executed on real devices under test. The sample devices have been supplied by a company dealing with the repair of electrical transformers. The tests on two devices have been performed.

6) To propose an evaluation method of measured dataset.

Two evaluation methods of the dataset measured by the FDS instrument have been outlined in Chapter 7.3. The methods are oriented to help comparison between two FDS datasets because the key of the FDS is to monitor changes in the FDS curve over time. One method utilizes area underneath curve computation and the second one correlation between current and previous measurement. The result of the method is a number, that can represent a measure of dataset changes. However, the proposed method needs to be verified on a reasonable amount of the tested object. Unfortunately, the scientific team was not able to gather such a dataset during the period when this thesis has been formed. This problem can be a topic for further research in the future.

8.2. Future Work

From the author's point of view, all the goals of the thesis have been fulfilled. The results of each goal and sub-goals are summarized in the text above and the detail about each of them can be found inside the thesis text. Nevertheless, there are still opportunities to make further improvements.

To make the DSP analyzer more portable it is necessary to solve the implementation of the inner high voltage amplifier. Also, the current sensing resistor is placed inside the box of the instrument. The current instrumentation topology with an external resistor and HV amplifier allows the system to be more scalable, but on the other hand, it sets higher knowledge requirements for the user.

The control application can be extended as well. The current version provides basic control of the instruments and plotting the DSP and FDS results. Measurement management can be added providing sending the results to the operator cloud or database and other features based on requirements of the real instrumentation users.

One of the next application improvements can be an implementation of an expert system. The current application version provides the results in the form of numbers only. On the other hand, the expert system could provide detailed information converted into a form where it is specified how dysfunction has occurred in the object a where it can be found. It shows such diagnostics can be made only if the particular DUT is periodically tested for a longer time (units of years). Therefore, the design of such a system is very tedious.

The two methods for data set evaluation has been proposed at the end of the thesis. The methods have been derived theoretically, but it would need verification on some amount of different tested objects. The tested objects can be various types of power grids transformers, but key thing is, to monitor their FDS curve development over some time. Such long-term access to the particular objects can be the main problem of the verification of the method. The scientific team was not able to establish cooperation with any company to get the relevant datasets. Anyway, this problem has been identified as one of the main future goals.

The topic of the non-invasive diagnostic is still widely discussed and it can be expected it will still be. The proper measurement methods supported by sophisticated instrumentation may point to an upcoming tested system failure. And therefore save a lot of funds if the failure occurs unexpectedly.

Author's Publications

Publications and Academical Contribution Related to the Thesis

Publications in journals with impact factor

TEREŇ, O. [40 %], TOMLAIN, J. [40 %], and SEDLÁČEK, R. [20 %] DIRECT COMPARISON OF ANALOG AND DIGITAL FGPA-BASED APPROACHES OF SYNCHRONOUS DETECTION. Metrology and Measurement Systems. 2018, 25(1), pp. 57-69. ISSN 0860-8229. Available from: http://journals.pan.pl/dlibra/journal/118154?language=en

TOMLAIN, J. [40 %], TEREŇ, O. [40 %], SEDLÁČEK, R. [10 %], and VEDRAL J. [10 %] A Hardware Platform for Frequency Domain Spectroscopy and Frequency Response Analysis. Acta Polytechnica Hungarrica. 2017, 14(8), pp. 47-63. ISSN 1785-8860. Available from: http://www.uni-obuda.hu/journal/Tomlain_Teren_Sedlacek_Vedral_79.pdf

Publications in ISI

TOMLAIN, J. and O. TEREŇ. HARDWARE PLATFORM FOR FRA AND FDS INSTRUMENTATION. In: SVATOŠ, J., ed. Proceedings of Student Conference on Sensors, Systems and Measurement 2021. Student Conference on Sensors, System and Measurement, Prague, 2021-06-14/2021-06-15. Praha: CESKE VYSOKE UCENI TECHNICKE V PRAZE, 2021. p. 39-40. ISBN 978-80-01-06822-9. - **The paper received 3rd place in section "Measurement of Electrical and Non-electrical Quantities at Competition of SCSSM 2021."**

TOMLAIN, J., et al. Experimental Verification of the Fully-Digital High Voltage FPGA-Based Diagnostic Equipment. In: Proceedings of the International Conference on New Trends in Signal Processing 2020. 2020 New Trends in Signal Processing (NTSP), Demänovská dolina, 2020-10-14/2020-10-16. Liptovský Mikuláš: Akadémia ozbrojených síl, 2020. p. 116-120. ISSN 1339-1445. ISBN 9781728161556. DOI 10.1109/NTSP49686.2020.9229545 - **The publication received Diploma Ph.D. Student Prize from the Program Committee of NTSP 2020.**

TEREŇ, O., et al. The design of an analog to digital front-end for frequency domain spectroscopy analyzer. In: BEC 2016 15th Biennial Baltic Electronics Conference (BEC). 15th Biennial Baltic Electronics Conference (BEC). Tallinn, 03.10.2016 - 05.10.2016. USA: IEEE Computer Society. 2016, pp. 155-158. ISSN 1736-3705. ISBN 978-1-5090-1393-7. Available from: http://ttu.ee/bec/16

TOMLAIN, J. and TEREŇ, O. FPGA-based System for Non-invasive Frequency Response Analysis Testing [online]. In: HUSNÍK, L., ed. Proceedings of the 20th International Scientific Student Conferenece POSTER 2016. 20th International Student Conference on Electrical Engineering. Praha, 24.05.2016. Praha: Czech Technical University in Prague. 2016, ISBN 978-80-01-05950-0. Available from: http://radio.feld.cvut.cz/conf/poster/ - **The publication received Diploma for the Ph.D. work from the Program Committee of POSTER 2016.**

TEREŇ, O. and TOMLAIN, J. An analog to digital front-end for frequency domain spectroscopy analyze [online]. In: HUSNÍK, L., ed. Proceedings of the 20th International Scientific Student Conferenece POSTER 2016. 20th International Student Conference on Electrical Engineering. Praha, 24.05.2016. Praha: Czech Technical University in Prague. 2016, ISBN 978-80-01-05950-0. Available from: http://radio.feld.cvut.cz/conf/poster/ - **The publication received Diploma for the Ph.D. work from the Program Committee of POSTER 2016.**

TEREŇ, O., SEDLÁČEK, R., and VEDRAL, J. CAPACITANCE AND DISSIPATION FACTOR METER FOR HIGH-VOLTAGE ELECTRICAL MACHINES. In: HOLUB, J., ed. XXI IMEKO WORLD CONGRESS - Full Papers. XXI IMEKO WORLD CONGRESS. Prague, 30.08.2015 - 04.09.2015. Prague: Czech Technical University in Prague, Faculty of Electrical Engineering. 2015, ISBN 978-80-01-05793-3.

Functional Samples

TOMLAIN, J., TEREŇ, O., and SEDLÁČEK, R. Měrič frekvenční odezvy pro vysokonapěťové stroje. [Functional Sample]. 2017

TEREŇ, O., TOMLAIN, J., and SEDLÁČEK, R. Měrič dielektrické spektroskopie pro vysokonapěťové stroje. [Functional Sample]. 2017

TOMLAIN, J., TEREŇ, O., and SEDLÁČEK, R. Širokopásmový dvoukanálový synchronní detektor. [Functional Sample]. 2015

TEREŇ, O., SEDLÁČEK, R., and VEDRAL, J. Řídicí modul DSP analyzátoru. [Functional Sample]. 2015, Available from: http://measure.feld.cvut.cz/projekty/SGS15/213/OHK3/3T/13

Other Publications and Academical Contribution

Publications in ISI

TOMLAIN, J., O. TEREŇ, and J. TOMLAIN. Communication Technologies and Data Exchange Possibilities for Smart Energy Solutions. In: Proceedings of the International Conference on New Trends in Signal Processing. 2018 New Trends in Signal Processing (NTSP), Demänovská dolina, 2018-10-10/2018-10-12. Liptovský Mikuláš: Akadémia ozbrojených síl, 2018. p. 210-215. ISSN 1339-1445. ISBN 978-80-8040-547-2.

TOMLAIN, J., TEREŇ, O., and TOMLAIN, J. Smart grid communication technologies for renewable power sources [online]. In: BAN, M., DUIĆ, N., and SCHNEIDER, D.R., eds. 12th Conference on Sustainable Development of Energy, Water and Environment Systems. 12th Conference on Sustainable Development of Energy, Water and Environment Systems. Dubrovnik, 04.10.2017 - 08.10.2017. Zagreb: SRCE University of Zagreb. 2017, pp. 480. ISSN 1847-7178.

TOMLAIN, J., TEREŇ, O., and TOMLAIN, J. Interoperability between Islands and Smart Concentrator Unit [online]. International Research Journal of Electronics and Computer Engineering. 2017, 3(2), pp. 28-30. ISSN 2412-4370. Available from: http://researchplusjournals.com/index.php/IRJECE/article/view/298

TOMLAIN, J., TEREŇ, O., and TOMLAIN, J. Solution For On-line Monitoring of Island Renewable Energy Sources. In: JANÍČEK, F., ed. Proceedings of the 13th International Scientific Conference Energy-Ecology-Economy 2016. Power Engineering 2016 (Energetika 2016). Tatranské Matlaire, 31.05.2016 - 02.06.2016. Bratislava: Slovak University of Technology. 2016, ISBN 978-80-89402-85-4.

TOMLAIN, J., TEREŇ, O., and TOMLAIN, J. Wireless Solutions for Outdoor Training Polygons. In: BERESIK, R., SOSTRONEK, M., and BABJAK, M., eds. Proceedings of the International Conference on New Trends in Signal Processing. 2016 New Trends in Signal Processing (NTSP). Demanovska dolina, 12.10.2016 - 14.10.2016. Liptovský Mikuláš: Akadémia ozbrojených síl. 2016, pp. 87-90. ISSN 1339-1445. ISBN 978-80-8040-528-1. Available from: http://ntsp2016.aos.sk/

ROHÁČ, J., et al. Inertial Reference Unit in a Directional Gyro Mode of Operation. In: IEEE SENSORS 2012 - Proceedings. IEEE SENSORS 2012. Taipei, 28.10.2012 - 31.10.2012. Piscataway: IEEE Service Center. 2012, pp. 1356-1359. IEEE Catalog Number CFP12SEN-USB. ISSN 1930-0395. ISBN 978-1-4577-1765-9. Available from: http://www.ieee-sensors2012.org/

Functional Samples

SEDLÁČEK, R., BOHÁČEK, J., and TEREŇ, O. Konstrukční návrh kvadrifilárního etalonu odporu jmenovité hodnoty 38 700 Ohm. Praha: OI Praha. 2016, HS8301631C000.

BOHÁČEK, J., et al. Proudové ekvalizéry pro koaxiální měřicí systémy. Praha: Úřad pro technickou normalizaci, metrologii a státní zkušebnictví. 2016, VIII/16/16. Available from: http://www.unmz.cz

SEDLÁČEK, R. and TEREŇ, O. Konstrukční návrh kvadrifilárního etalonu odporu jmenovité hodnoty 12906 Ohm. Praha: OI Praha. 2016, HS8301667C000.

SEDLÁČEK, R., et al. Konstrukční návrh sério-paralelní odporové zařízení (SPRD) pro kalibraci referenčních indukčních děličů napětí. Praha: OI Praha. 2016, HS8301641C000.

TOMLAIN, J., et al. SSD Logger. [Functional Sample] 2018.

VEDRAL, J., et al. Funkční vzorek diagnostického systému. [Functional Sample] 2018.

VEDRAL, J., et al. Programové vybavení diagnostického systému. [Software] 2018.

Bibliography

[1] J. Simons, "Diagnostic testing of high-voltage machine insulation. a review of ten years' experience in the field," May 1980.

[2] J. van Bolhuis, E. Gulski, and J. Smit, "Monitoring and diagnostic of transformer solid insulation," *Power Delivery, IEEE Transactions on*, vol. 17, no. 2, pp. 528–536, Apr 2002.

[3] T. Saha, M. Darveniza, D. Hill, and T. Le, "Electrical and chemical diagnostics of transformers insulation. b. accelerated aged insulation samples," *Power Delivery, IEEE Transactions on*, vol. 12, no. 4, pp. 1555–1561, Oct 1997.

[4] M. S. Naidu, *High voltage engineering*, 2nd ed. New York: McGraw-Hill, no. ISBN 0074622862.

[5] M. Farahani, "A method for the evaluation of insulation systems for high voltage rotating machines," June 2003.

[6] R. Schwarz and M. Muhr, "Diagnostic methods for transformers," in *Condition Monitoring and Diagnosis, 2008. CMD 2008. International Conference on*, April 2008, pp. 974–977.

[7] B. Ward, "A survey of new techniques in insulation monitoring of power transformers," *Electrical Insulation Magazine, IEEE*, vol. 17, no. 3, pp. 16–23, May 2001.

[8] M. Farahani, H. Borsi, and E. Gockenbach, "Dielectric spectroscopy in time and frequency domain on insulation system of high voltage rotating machines," vol. 1, pp. 60–63 Vol.1, July 2004.

[9] R. H. Cole, "Time-domain spectroscopy of dielectric materials," *IEEE Transactions on Instrumentation and Measurement*, vol. IM-25, no. 4, pp. 371–375, Dec 1976.

[10] V. Mentlik, *Dielektricke Prvky a Systemy*, 1st ed. BEN - technicka literatura, no. ISBN 8073001896.

[11] J. Guo, T. Bamber, and M. Chamberlain, "Optimization and experimental verification of coplanar interdigital electroadhesives," vol. 49, p. 415304, 09 2016.

[12] Agilent Technologies, Inc., "Basics of measuring the dielectric properties of materials."

[13] J. Gregorec, "The basics of insulation testing," *NETA WORLD, Fall 2006*, no. ISBN 5989-2589EN.

[14] W. S. Zaengl, "Dielectric spectroscopy in time and frequency domain for hv power equipment. i. theoretical considerations," *Electrical Insulation Magazine, IEEE*, vol. 19, no. 5, pp. 5–19, Sept 2003.

[15] E. Kuffel, W. S. Zaengl, and J. Kuffel, *High Voltage Engineering Fundamentals*, 2nd ed. Butterworth-Heinemann, no. ISBN 0750636343.

[16] N. A. M. Jamail, M. A. M. Piah, and N. A. Muhamad, "Comparative study on conductivity using polarization and depolarization current (pdc) test for hv insulation," in *Electrical Engineering and Informatics (ICEEI), 2011 International Conference on*, July 2011, pp. 1–6.

[17] H. A. P. Silva, W. Bassi, and A. C. T. Diogo, "Noninvasive ageing assessment by means of polarization and depolarization currents analysis and its correlation with moisture content for power transformer life management," in *Transmission and Distribution Conference and Exposition: Latin America, 2004 IEEE/PES*, Nov 2004, pp. 611–616.

[18] J. Abhishek and P. Aaradhi, "Dielectric diagnosis of ehv current transformer using frequency domain spectroscopy (fds) & polarization and depolarization current (pdc)," *International Journal of Scientific & Engineering Research*, Nov 2012.

[19] M. Koch, M. Krueger, and M. Puetter, *Advanced Insulation Diagnostic by Dielectric Spectroscopy.*

[20] "Ieee recommended practice for testing insulation resistance of rotating machinery," *IEEE Std 43-2000*, pp. i–, 2000.

[21] OMICRON , *Dirana. Dielectric response analysis and moisture in oil-paper dielectrics.* [Online]. Available: https://www.omicronenergy.com/fileadmin/user_upload/pdf/literature/DIRANA-Brochure-ENU.pdf

[22] OMICRON, *Spectano 100. Dielectric Material Analyzer.* [Online]. Available: https://www.dacpol.eu/en/dielectric-materials-analyzer-spectano-100-64139/product/dielectric-materials-analyzer-spectano-100?file=files/pl/katalog/2015/spectano_100/PDF/Technical%20data_V1-1606_LR.pdf

[23] Megger Sweden AB, *IDAX 300/350 Insulation Diagnostic Analyzers.* [Online]. Available: http://www.megger.cz/wp-content/uploads/2013/06/Prospekt-IDAX-300-350.pdf

[24] M. M. Yaacob, M. A. Alsaedi, and J. R. Rashed, "Review on partial discharge detection techniques related to high voltage power equipment using different sensors," vol. Volume 4, pp. 325–337.

[25] S. Kornhuber, S. Markalous, M. Muhr, T. Strehl, and C. Sumereder, "Comparison of methods for the dissipation factor measurement at practical examples," in *Procedings of the 16th International Symposium on High Voltage Engineering.*

[26] N. Prakash, "Expert system for sweep frequnency response analysis of power transformer," in *Natinoal Conference of Emerging Trends in Electrical, Instrumentation & Communication Engineering*, vol. Volume 3.

[27] Texas Instruments Incorporated . ADS126x 32-Bit, Precision, 38-kSPS, Analog-to-Digital Converter (ADC) with Programmable Gain Amplifier (PGA) and Voltage Reference. [Online]. Available: http://www.ti.com/lit/ds/symlink/ads1263.pdf

[28] Texas Instruments Incorporated. ADS42LBx9 14- and 16-Bit, 250-MSPS, Analog-to-Digital Converters. [Online]. Available: http://www.ti.com/lit/ds/symlink/ads42lb69.pdf

[29] Analog Devices, Inc. Fundamentals of direct digital synthesis (dds). [Online]. Available: http://www.analog.com/media/en/training-seminars/tutorials/MT-085.pdf

[30] Texas Instruments Incorporated. 14-Bit, 165MSPS digital-to-analog converter. [Online]. Available: http://www.ti.com/lit/ds/symlink/dac904.pdf

[31] Analog Devices, Inc. Fundamentals of phase locked loops (plls). [Online]. Available: http://www.analog.com/media/en/training-seminars/tutorials/MT-086.pdf

[32] Silicon Laboratories, Inc. I2c-programmable any-frequency, any-output quad clock generator. [Online]. Available: https://www.silabs.com/documents/public/data-sheets/Si5338.pdf

[33] Texas Instruments Incorporated. Low voltage differential signaling (lvds). design notes. [Online]. Available: http://www.ti.com/lit/an/slla014a/slla014a.pdf

[34] H. Johnson and M. Graham, *High Speed Digital Design: A Handbook of Black Magic*. Prentice Hall, 1993. [Online]. Available: https://www.amazon.com/High-Speed-Digital-Design-Handbook/dp/0133957241?SubscriptionId=AKIAIOBINVZYXZQZ2U3A&tag=chimbori05-20&linkCode=xm2&camp=2025&creative=165953&creativeASIN=0133957241

[35] LXI Consortium. Lxi device specification 2016. [Online]. Available: http://www.lxistandard.org/members/Adopted%20Specifications/Latest%20Version%20of%20Standards_/LXI%20Standard%201.5%20Specifications/LXI%20Device%20Specification%20v1_5_01.pdf

[36] Modbus Organization, Inc. Modbus application protocol specification v1.1b3. [Online]. Available: http://www.modbus.org/docs/Modbus_Application_Protocol_V1_1b3.pdf

[37] G. Clarke, D. Reynders, and E. Wright, *Practical Modern SCADA Protocols: DNP3, 60870.5 and Related Systems*, edition 12 ed. IDC Technologies, 2004, no. ISBN 07506 7995.

[38] J. Thelin, *Foundations of Qt Development (Expert's Voice in Open Source)*. Apress, 2007, no. ISBN 1590598318.

[39] J. Prata, *Mistrovství v C++*, 2nd ed. Computer Press, Praha, 2001, no. ISBN 978-80-251-0098-1.

[40] A. Koenig and B. E. Moo, *Rozumíme C++*, 1st ed. Computer Press, Praha, 2003, no. ISBN 80-7226-656-X.

[41] M. Chroboczek, *Grafická uživatelská rozhraní v Qt a C++*, 1st ed. Computer Press, Brno, 2013, no. ISBN 978-80-251-424-3.

[42] Joint Committee for Guides in Metrology. Evaluation of measurement data — guide to the expression of uncertainty in measurement. [Online]. Available: https://www.bipm.org/utils/common/documents/jcgm/JCGM_100_2008_E.pdf

[43] J. Boháček, *Metrology.* ČVUT v Praze, Praha, 2013, no. ISBN 978-80-01-05351-5.

[44] Toellner Electronic Instrumente GmbH . 150 w four-quadrant amplifier. [Online]. Available: http://www.caltest.fi/pdf/7610.pdf

[45] Tereň, O., "Merač kapacity a stratového činiteľa VN strojov," *Master thesis, CTU Prague, FEE, Department of Measurement, 2014.*

[46] Tereň O., Sedláček R. and Vedral J., "Capacitance and dissipation factor meter forhigh-voltage electrical machines," *XXI IMEKO World Congress "Measurement in Research and Industry".*

[47] Tereň, O., Tomlain, J., Sedláček R. and Vedral, J., "The design of an analog to digital front-end for frequency domain spectroscopy analyzer," *BEC 2016 15th Biennial Baltic Electronics Conference (BEC).*

[48] Tereň, O., Tomlain, J. and Sedláček R., "Direct comparison of analogue and digital fgpa-based approaches to synchronous detection," *Metrology and Measurement Systems. 2018.*

[49] Tomlain, J., Tereň, O., Sedláček, R. and Vedral, J., "Experimental verification of the fully-digital high voltage fpga-based diagnostic equipment," *Proceedings of the International Conference on New Trends in Signal Processing 2020.*

Appendix A.

Communication protocol

A.1. Protocol Basics

The main demand to define the protocol was it is suitable for use either via virtual COM port (VCP) or TCP/IP socket. According to the proposed usage, to communicate the control application with one instrument, it is enough to define the protocol as a point-to-point topology. The protocol defines a server-client topology, see Fig. 47. The PC control application is supposed to be the client and the measuring instrument is the server.

The topology allows to initiation of a request by the client. The request may be understood as a demand either to write some data into the server memory space or read some data from the server memory space. Once, the server receives the request, it initiates a response. The response contains an acknowledgment in the case of writing data or demanding data in the case of reading data. The protocol also allows asynchronous data transmission from the server to the client. When an event occurs, the server is allowed to initiate sending an event message. These procedures are commonly called transactions. All types of transactions are further described in Chapter A.5.

A.2. Memory Space

The memory space is a set of internal server variables, which can be changed or read out via the protocol. The protocol allows several data types each of which occupied its part of the server memory. Each part can be up to 256 items long. The complete set of the provided data types is shown in Table 10. An example of the server memory space organization is shown in the picture 78. The picture is showing a maximized version of the memory space.

The protocol does not demand to implement of all of the data type sections or their maximum number of values. The protocol user can decide which data types and their amount are necessary and the other section can be omitted. Only the protocol

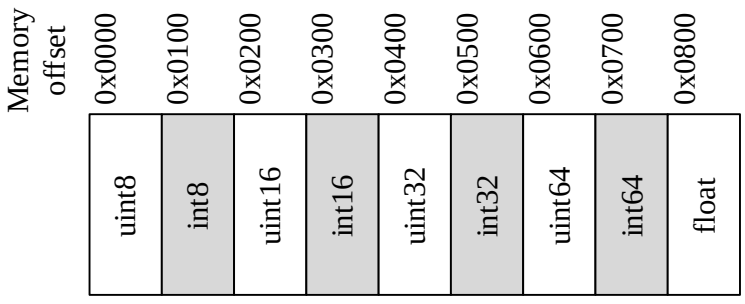

Figure 78. The memory space organization example

Table 10. Set of provided data types

Data type	Length	Binary code
uint8	8 bytes	0000
int8	8 bytes	1000
uint16	16 bytes	0001
int16	16 bytes	1001
uint32	32 bytes	0010
int32	32 bytes	1010
uint64	64 bytes	0011
int64	64 bytes	1011
float	32 bytes	1110

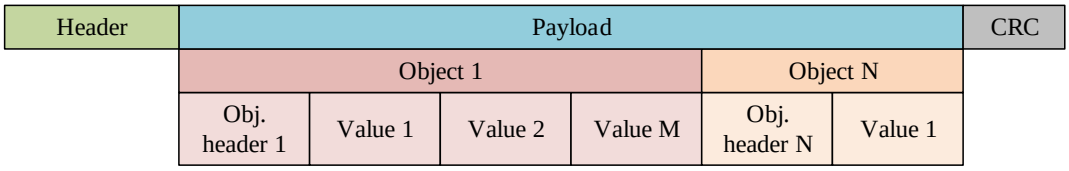

Figure 79. Protocol packet format

implementation has to be able to recognize which part of memory has to be entered according to the transmitting value address. In the case of requesting a non-existing value, the server has to respond with an error code. The list of all supported error codes is stated in Chapter A.5.

A.3. Packet Format

All requests, responses, and events are encapsulated in packets. The packet format is shown in Figure 79. It is not necessary to adhere the packet has not to be divided into more parts. On the other hand, when the packet is divided, it has to be ensured, all packet parts will arrive in the correct order.

Figure 79 shows the packet in three hierarchical layers. The top layer is divided into three parts. The first part is a header. The header serves to synchronization of the packet receiver (helps to find the actual packet beginning), determine the length of the payload part, and type of the transaction. The middle part is a payload. This part is intended for data transmission itself. It can be a maximum of 255 bytes long. The payload consists of an object. The payload can consist of a maximum of seven objects. The object can be understood as a data array of one of the provided data types. Depending on the transaction type, the object can define the addresses and amount of demanding values or the values data itself. In the other words, the protocol allows to read or write different data types in one packet. The last part is a cyclic redundancy check. It serves to check the integrity of the packet and minimized the probability of the falsely correct packet receiving.

The protocol header consists of four bytes. Figure 80 shows a detailed description of the header. Bytes number zero and one are used as a preamble and their value is fixed

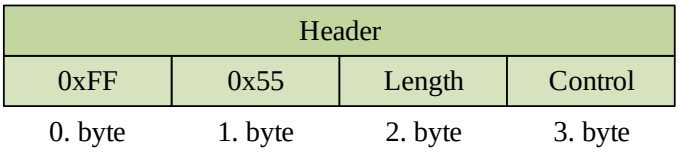

Figure 80. Protocol header detailed description.

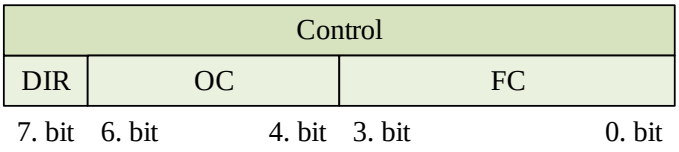

Figure 81. Protocol control byte detailed description.

Table 11. Set of provided function codes

Function code	**Meaning**
0x01	Read objects from server
0x02	Write objects to server
0x03	Asynchronous event from server
0x04	Ping
0x09	Read object error
0x0A	Write object error

set to $0xFF$ and $0x55$. The preamble helps the receiver of the packet to find the actual packet beginning and together with the CRC, the receiver can recognize the correct position in the packet. Byte number two defines the length of the payload part. Its maximum value can be 255.

The last byte is a control byte. The control byte consists of 8 bits and their detailed description is shown in Figure 81. The bit number seven represents a direction (DIR) of the transmission. If the DIR bit is set to zero, it means the transmission from server to client, otherwise transmission from client to the server. The next bits represent object count (OC) which are included on the following payload. According to the length of this field, its maximum value is seven. It means, the protocol can transmit a maximum of seven objects in one packet. The last field is a function code (FC). The function code determines the type of the transaction. The list of all supported function codes is stated in Table 11.

The payload consists of one or up to seven objects. The object determines the demand of the read or writes data by specifying the data type, starting address, and amount of values. As Figure 79 shows, the object consists of an object header followed by a sequence of a specified number of values. The detailed description of the object header is shown in Figure 82. The first four bits (15. to 12. bit) represent the sequence count (SC) number. This number determines the number of values transmitted after the object header. For example, when a written request of four uint16 numbers is transmitted, the SC number is set to four and the whole byte length of the value part is

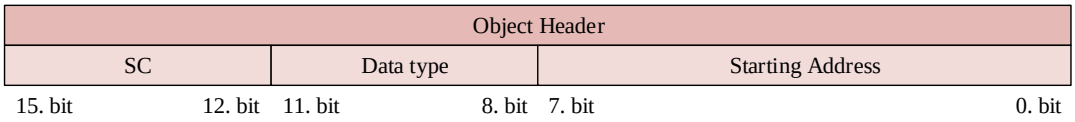

Figure 82. Protocol object header detailed description.

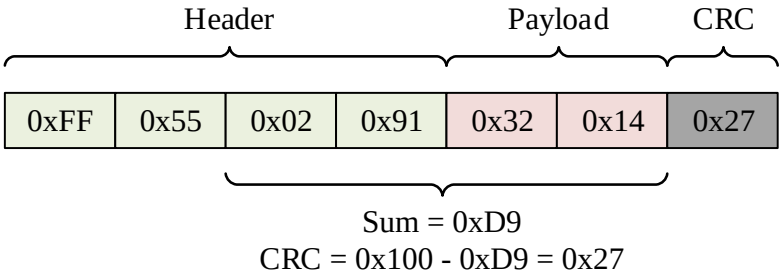

Figure 83. Protocol object header detailed description.

eight bytes. The next four bits of the header (11. to 8. bit) define the data type or the section of the server memory space (see Chapter A.2). The whole list of the supported data types with their hex codes is stated in Table 10. The last field of the header is starting address (7. to 0. bit). The starting specifies the point in memory space from which is data transmitted or read. For example, if starting address is set to 0x10 and the sequence count is to five, the server access the values from address 0x10 to 0x14. The detailed description of these situations is stated in Chapter A.5.

The last field of the packet is cyclic redundancy check (CRC). There is a lot of different ways how to define and compute CRC. For purposes of the designed HW platform, a basic one-byte sum of the packet bytes had been chosen. The sum covers the second byte of the packet (Length field) up to the last byte of the payload. The resulting CRC is then computed as subtraction of 0x100 number and the sum of the packet bytes. An example of the CRC calculation is shown in Figure 83.

A.4. Error Codes

Error codes are messages transmitted when a communication error occurs. For example, an error can be caused when the client is trying to read or write values that are out of the server memory space. When the situation occurs, the server responds with an error code, which is indicated in the function code field of the packet header. There is an error code transmitted in the payload section. All supported error codes are stated in Table 12. They were defined according to the Modus standard [36]. The way of the use of the error codes is stated in Chapter A.5.

A.5. Transactions

The transaction is a process during which the data exchange is executed. The transaction can be initiated by the client or server. There are several types of transactions defined and each of them has a function code assigned. The complete list of the function codes is stated in Table 11. All of the supported transactions are described in the

Table 12. Set of provided error codes.

Error code	Meaning
0x01	Illegal function
0x02	Illegal data address
0x03	Illegal data value

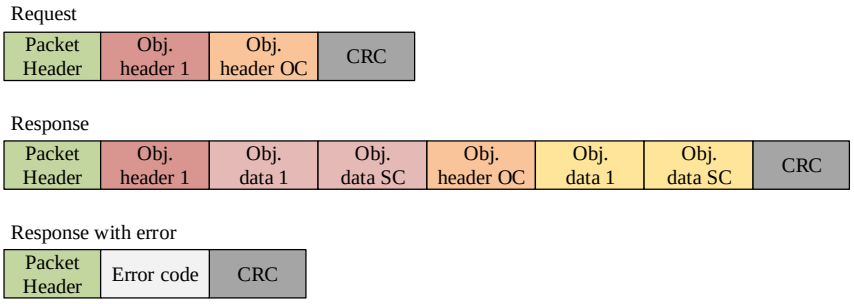

Figure 84. Read objects transaction general format.

further text.

Read Objects Transaction

The read object transaction serves to read data from the server. The general read transaction format is stated in Fig. 84. The client initiates the request, which is consisted of the packet header, object header describing the demanding data types and address, and the CRC. After the server receives the request, it prepares the output data and forms the response. The response consists of a packet header followed by the objects descriptors. Each object descriptor consists of the object header followed by the object data. At the end of the packet, the CRC code is transmitted. In the case an error occurs, for example, the client tries to access an invalid data address, the payload section of the packet consists only of the error code. The detected error is also signalized in the packet header in the function code field. An example of the read transaction reading one value from uint8 data space from address 10 and one value from float data space from address 4 is shown in Fig. 85.

Write Objects Transaction

The write objects transaction serves to write data into the server data space. The general write transaction format is stated in Fig. 86. The client initiates the request consisting of a packet header followed by the objects descriptors. Each object descriptor consists of the object header followed by the object data which is supposed to be written into the server memory space. At the end of the packet, the CRC code is transmitted. After the server receives the request, tries to write the received data and then prepare the response. If the write operation is successful, the response consists of the packet header, objects headers of the written objects, and the CRC. Otherwise, the payload consists only of the error code and the error is also signalized in the packet header function code field. An example of writing two values into the int8 data space to address 100 is shown in Fig. 87.

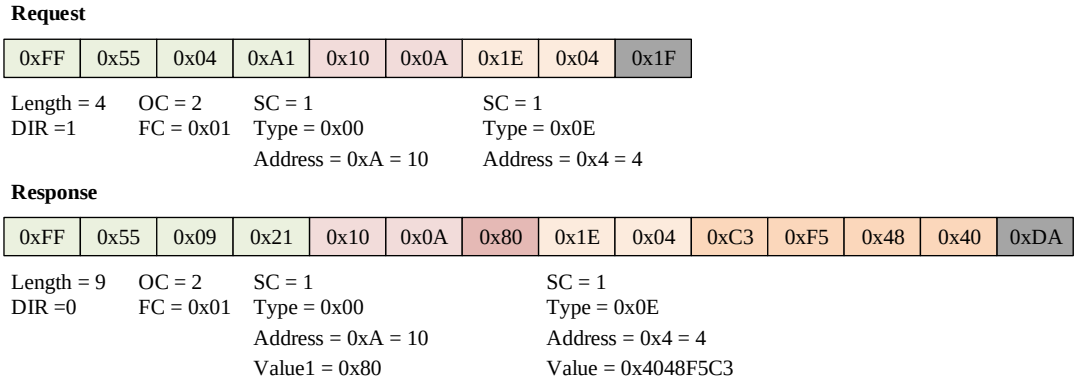

Figure 85. Read objects transaction example.

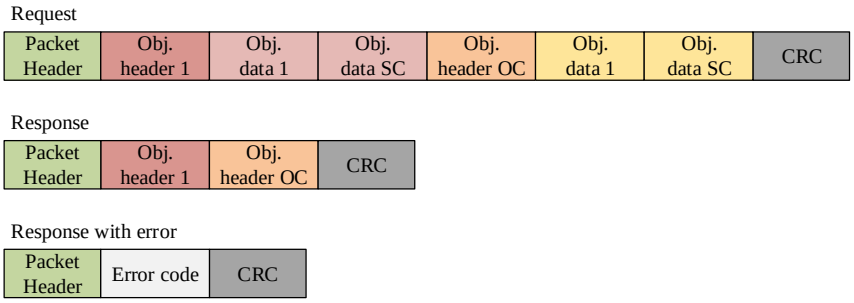

Figure 86. Write objects transaction general format.

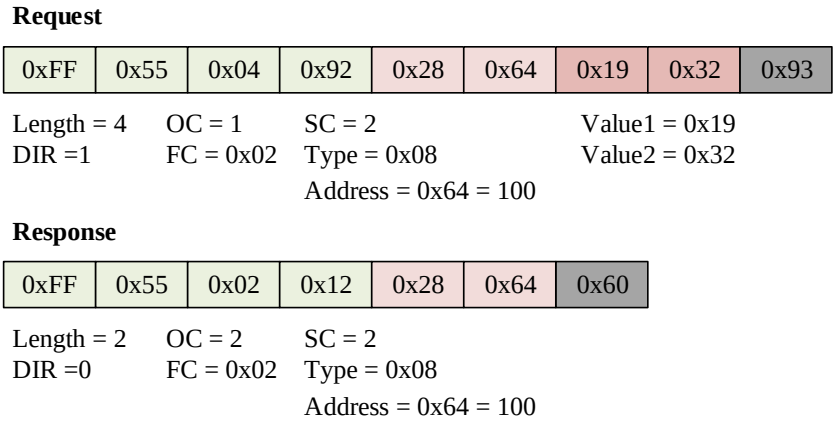

Figure 87. Write objects transaction example.

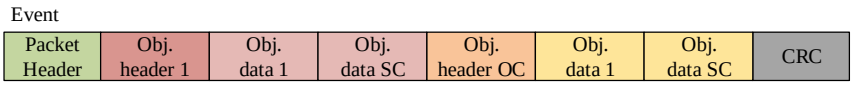

Figure 88. Event transaction general format.

Event

0xFF	0x55	0x04	0x13	0x11	0x00	0xAA	0x00	0x2E

Length = 4 OC = 1 SC = 1
DIR =0 FC = 0x03 Type = 0x01
Address = 0x00 = 0
Value1 = 0x00AA

Figure 89. Event transaction example.

Request

0xFF	0x55	0x00	0x84	0x7C

Length = 0 OC = 0
DIR =1 FC = 0x04

Response

0xFF	0x55	0x00	0x04	0xFC

Length = 0 OC = 0
DIR =0 FC = 0x04

Figure 90. Ping transaction format.

Event Transaction

The event transaction serves to the server to announce to the client a change has been captured. The change can be understood as a value of the data space being changed or an interrupt being caught. In contrast with reading and writing transactions, the event transaction is initiated only by the server. The general format of the event transaction is shown in Fig. 88. The event consists of a packet header followed by the objects descriptors. Each object descriptor consists of the object header followed by the object data. At the end of the packet, the CRC code is transmitted. There is no defined error code transmission. An example of event transmission of one uint16 value from address zero is shown in Fig. 89.

Ping Transaction

The ping transaction serves the client to check the presence of the server on the bus. Therefore, no data transmission is needed. The format of the ping transaction is shown in Fig. 90. The client initiates the request and the server replies by the response once the request is received.